Designing a sustainable bridge deck by using Basalt Fibre Reinforced Polymer

A comparative study

D.H.E. Coppus

TU Delft

Royal HaskoningDHV
Enhancing Society Together

This page was intentionally left blank

Designing a sustainable bridge deck by using Basalt Fibre Reinforced Polymer

A comparative study

By

D.H.E. Coppus

to obtain the degree of Master of Science
at Delft University of Technology,
to be defended publicly on Friday, January 31, 2025, at 3PM (UTC+1:00)
in Lecture Hall F at the Faculty of Civil Engineering and Geosciences,
Stevinweg 1, 2628 CN Delft

Student number:	4952952	
Project duration:	August 2024 – January 2025	
Thesis committee:	Prof.dr.ir. M.A.N. Hendriks (chair)	TU Delft, Concrete Structures
	Dr.ir. E.O.L. Lantsoght	TU Delft, Concrete Structures
	Ir. A.C.B. Schuurman	TU Delft, Applied Mechanics
	Ir. R.P.H. Vergoossen	TU Delft/Royal HaskoningDHV

This page was intentionally left blank

Preface

While writing this preface, I am filled with a sense of accomplishment and pride, as well as a surreal feeling. I feel accomplished and proud because, after months of hard work, I have successfully completed this thesis with a result that I am very satisfied with. However, I also experience a surreal feeling, as the completion of this thesis marks the end of my 6,5 years as a student at Delft University of Technology. During this time, I have not only acquired knowledge and skills in the field of Civil Engineering but have also had the opportunity to develop myself personally.

The topic of this thesis precisely reflects my interests within civil engineering, namely concrete structures, innovative materials, and finite element modeling. This research was conducted within the Concrete Structures section of the Faculty of Civil Engineering and Geosciences at Delft University of Technology. The thesis was performed in close collaboration with Royal HaskoningDHV, a leading global consulting engineering company. This collaboration provided me with the opportunity to not only explore the academic perspective of research but also to understand its practical implications and how this knowledge is applied in the industry.

Without the help and expertise of my thesis committee, this thesis would not have achieved its current result. First and foremost, I would like to thank ir. R.P.H. Vergoossen for introducing the topic, providing daily guidance at Royal HaskoningDHV, sharing his knowledge and expertise on all matters related to concrete, and allowing me to utilize his network in the concrete industry.
My deepest gratitude also goes to dr. ir. E.O.L. Lantsoght. Her communication, valuable feedback, and assistance over the past months have been invaluable. It has shown that supervising remotely with a six-hour time difference is absolutely no obstacle.
I would also like to thank ir. A.C.B. Schuurman for his critical questions during meetings and his insightful perspective on my work from a building engineering perspective.
Furthermore, I would like to thank the chair of the committee, prof. dr. ir. M.A.N. Hendriks, for his expertise throughout the process and his critical view on my work, which elevated it to a higher academic level.

In addition to my thesis committee, my heartfelt thanks go to my family, friends, and girlfriend for their unwavering support and belief in me. Without them, this would never have been possible.

I proudly present you my thesis, which focuses on the sustainability improvement and structural performance of a concrete bridge deck in an inverted T-girder bridge, through the application of Basalt Fibre Reinforced Polymer. I hope you enjoy reading it.

D.H.E. (Daan) Coppus
Delft, January 2025

Abstract

Concrete structures are responsible for a substantial share of the total global CO_2 emissions. This has led to the establishment of the Betonakkoord in the Netherlands, which aims to significantly reduce the emissions from concrete structures.

Reinforcement bars made from Basalt Fibre Reinforced Polymer (BFRP) offer a potential solution for making concrete structures more sustainable. Firstly, the Environmental Cost Indicator (ECI) of BFRP rebar is 43% lower than that of steel rebar. Additionally, BFRP does not corrode, which eliminates the requirement for a thick concrete cover to meet environmental class standards. Consequently, the use of BFRP reinforcement instead of steel could potentially reduce the amount of concrete needed, further enhancing the sustainability of concrete structures.

This study investigates the feasibility of enhancing the sustainability of a bridge deck in an inverted T-girder bridge by using BFRP rebars. BFRP differs from steel in several material properties. Although its strength, at approximately 1200 N/mm², is significantly higher than that of B500B steel, the much lower E-modulus of BFRP presents challenges. Additionally, BFRP behaves in a fully linearly elastic manner until failure in the absence of a yield plateau. The lower stiffness results in higher deformations and crack widths. The hypothesis is that this could potentially be problematic for shear capacity, as the concrete compression zone is reduced, aggregate interlock decreases, and dowel action is less effective due to the low transverse strength of the rebar.

In this study, various design variants for a bridge deck in an inverted T-girder bridge were modeled to assess the impact of different design parameters. A reference design variant with steel reinforcement was used as a baseline and compared with several variants incorporating BFRP rebars. The BFRP design variants differed in terms of reinforcement quantity, concrete cover, and effective depth.

A quasi-linear model of an inverted T-girder bridge was developed using the numerical software SCIA Engineer. The bridge deck design alternatives were modeled as an orthotropic plate with centroidal ribs. The numerical model clearly demonstrated that, due to the less stiff nature of the BFRP-reinforced bridge decks, there is less distribution of traffic loads compared to relatively stiff steel-reinforced bridge deck. Ultimately, the model showed that shear force is indeed the critical failure mechanism for BFRP-reinforced bridge decks. Reducing the effective depth of the BFRP reinforced bridge deck variants, decreases the shear force distribution in transverse direction by 5% and further decreases the shear capacity by 23% to 30%, depending on the adjusted parameters for each design variant.
The application of BFRP rebar in a bridge deck and the reduction of concrete cover to 25 mm, instead of the usual 50 mm used with steel reinforcement, is shown to be feasible in this study. An optimization was conducted to develop a bridge deck design, that meets the structural performance criteria of shear force while minimizing concrete usage. This resulted in an optimized design with a bridge deck height of 215 mm, compared to the conventional 250 mm.

A sustainability study based on the LCA cradle-to-gate life cycle phases (A1-A3) has demonstrated that BFRP reinforcement can significantly enhance the sustainability of a bridge deck. For the optimized design variant that meets all the structural requirements, the ECI reductions range from 27% to as much as 32%, depending on the cement type used in the concrete mixture. This study has shown that the application of BFRP rebars in a concrete bridge deck is certainly feasible and results in significant sustainability improvements.

Contents

This page was intentionally left blank

1. Introduction

1.1 Background and relevance

Concrete is the most used building material worldwide and its demand is still increasing. Despite the many positive properties of concrete, there is also a downside: a lot of carbon dioxide (CO2) is released during production. This, in combination with the large quantities of concrete used, gives CO2 emissions coming from the concrete industry a significant share of total global CO2 emissions. The concrete industry accounts for approximately 8% of current anthropogenic CO2 emissions worldwide (Tracy, 2023). The Dutch government, together with MVO Nederland, took the initiative to draw up the Betonakkoord to reduce CO2 emissions from concrete production. The main objectives of the Betonakkoord are a 30% CO2 reduction in 2030 compared to 1990, with an ambition of 49% reduction in the chain (Betonakkoord, 2018).

A possible solution for reducing CO2 emissions is to simply decrease the amount of concrete in structures. For instance, one could choose to reduce the concrete cover layer to use less material. In traditional steel reinforcement bars, the maximum allowable crack width of the concrete usually determines the thickness of the cover layer (Medeiros, Rocha, R.A.-Medeiros-Junior, & Helene, 2017). Steel reinforcement can corrode due to penetrating water, chlorides, salts, and other chemicals, leading to structural damage.

On the other hand, one could also use a new promising innovation in the field of reinforcement namely: reinforcement that does not corrode. These so-called non-corrosive reinforcement bars will therefore not corrode when water, chlorides, salts and other chemicals penetrate the concrete. Crack width of the concrete may then become less crucial, meaning that a lower concrete cover layer may be maintained. Applying the lower concrete cover layer could possibly result in a significant reduction of concrete usage and its CO2 emissions, especially for concrete structures with a large surface area to volume ratio. Additionally, if the non-corrosive reinforcement bars themselves also have a lower CO2 emission per unit volume used compared to steel reinforcement, this will further enhance the sustainability of the structure.

1.2 Research problem

The use of Fiber Reinforced Polymers (FRP), as non-corrosive reinforcement, can result in a reduction of the concrete cover in concrete bridge decks which are cast in-situ on prefabricated inverted T-beams. This can be done because the reinforcement cannot corrode, and a larger crack width is permitted. For these cast-in-situ concrete bridge decks on inverted T-beams, a significant reduction in concrete usage could be achieved. Suppose that the concrete cover of a bridge deck with a height of 250 mm can be halved from 50 mm to 25 mm on both the top and bottom sides of the cross-section, this results in a reduced total height of 200 mm. This equates to a 20% reduction in concrete usage for the bridge deck. However, relatively little research has been done into the extent to which concrete covers can decrease when using FRP and the influence of this on the shear capacity. Firstly, FRP has a lower modulus of elasticity, which results in larger cracks in the concrete under the same load, compared to cases with steel reinforcement. Secondly, the reduction in concrete cover leads to a decrease in cross-sectional height. This combination of larger cracks and reduced cross-section can result in a significantly lower shear capacity than when steel reinforcement with higher concrete cover is used.

The most used FRP rebars are glass, carbon and aramid (fib bulletin 40, 2007). More recently, basalt fibres have also become increasingly applied. Given that basalt fibre reinforced polymers (BFRP) are a relatively new technology, with ongoing research into their properties and applications, and pose fewer problems regarding recycling, this study focuses on the application of BFRP rebars as non-corrosive reinforcement in cast-in-situ concrete bridge decks on inverted T-beams.

1.3 Research objectives

This research aims to create an understanding of the decrease in shear capacity of cast-in-situ concrete bridge decks on prefabricated inverted T-beams, because of the use of BFRP, instead of traditional steel reinforcement, with a smaller concrete cover.
This includes the following objectives:

- Determine the decrease in shear capacity because of the use of BFRP and a lower concrete cover, based on calculation rules, literature and numerical modelling.
- Develop a comprehensive design methodology for bridge decks reinforced with BFRP, focusing on optimizing structural performance and sustainability
- Determine the effect of the ECI of a cast-in-situ concrete bridge deck on prefabricated inverted T-beams when BFRP and a lower concrete cover are applied.

1.4 Research scope

This research will be conducted based on a case study of a concrete bridge yet to be built in a Dutch highway. This bridge consisting of inverted T-beams covered by a bridge deck, will be used to investigate the effect of using BFRP in combination with a lower concrete cover than if steel reinforcement was used. The focus in this research will only be on the bridge deck. The underlying inverted T-beams are not part of the scope of this research. Next to this FRP materials other than basalt are beyond the scope of this study.
Building a numerical model cannot provide an exact representation of reality. Nevertheless, this research aims to build a representative model within its constraints, which closely mimics reality. This approach will enable an accurate simulation of the effect of BFRP in combination with a reduced concrete cover in concrete bridge decks.

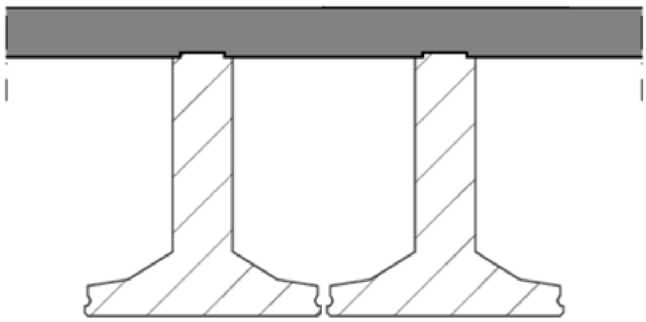

Figure 1.4: Cast-in-situ bridge deck on top of prefabricated inverted T beams (Rooij, 2011)

1.5 Research questions

Main research question:

To what extent does the use of BFRP in combination with a smaller concrete cover, in a cast-in-situ concrete bridge deck on prefabricated inverted T-beams, influence the shear capacity?

Sub research questions:

- To what extent has BFRP already been used in built structures and what design principles were followed?
- What are the current design codes and guidelines for using FRP rebars in concrete structures?
- How can the load distribution in a concrete bridge deck reinforced with BFRP be tested with a numerical model?
- What is the difference in governing failure mechanisms between BFRP reinforced concrete bridge decks and steel reinforced concrete bridge decks?
- What is the CO2 reduction of a concrete bridge deck when BFRP combined with a smaller concrete cover is used compared to traditional steel reinforcement with a thicker concrete cover?

1.6 Thesis outline

To guide the reader of this report, this section will provide an overview of the various chapters of the report with a brief description of the content of each chapter. The next chapter, Chapter 2, presents the literature review, which provides information on BFRP, explains the principle of shear capacity, highlights design codes and guidelines, and reviews experimental studies. Following this, Chapter 3 conducts a preliminary analysis of bridge deck design using various design codes. Chapter 4 then provides a detailed description of the case study of a concrete bridge deck in an inverted T-girder bridge. This case study description will outline the geometry of the bridge and the associated traffic loads, which will then be converted into a numerical model in Chapter 5. Chapter 5 details the principles followed in building the numerical model and the outcomes of the analyses of the different bridge deck design variants will be given. Chapter 6 will then discuss the failure mechanisms of the different design variants, from which an optimized design variant is found. In Chapter 7, each design variant is evaluated for its sustainability using the environmental cost indicator. The corresponding LCA boundaries and calculation methods are also described. Chapter 8 presents the discussion of the modeling approach used and the generated results. Subsequently, Chapter 9 provides the conclusion of the report by answering the research question. The report concludes with Chapter 10, which offers recommendations for practice and future research.

2. Literature review

2.1 Fibre Reinforced Polymer Materials

2.1.1 FRP principles

Fiber reinforced polymers (FRP) are materials that can be used as alternative non-corrosive reinforcement in concrete structures. FRP consists of continuous fibres impregnated with polymeric resins. The main function of this resin is to bundle the fibres and hold them together, in this way it distributes the load on the rebar over all the fibres that make up the rebar. In addition, the resin protects the fibres during transport and handling on the construction site.

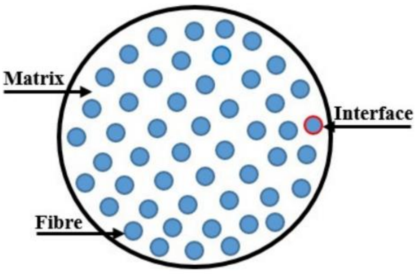

Figure 2.1.1.1: Schematic composition of FRP rebar (Rajak, Wagh, & Linul, 2022)

The most common manufacturing process is the pultrusion process in which the fibres are pulled and impregnated before curing takes place in a heated die (fib bulletin 40, 2007).
FRP fibres could consist of different materials such as: carbon, aramid, glass and basalt. The main advantage of FRP materials is that they do not corrode, which increases the durability of the concrete structure in which they are applied. Another advantage of FRP is its electromagnetic neutrality, which makes it suitable for environments where magnetic fields can be very critical, such as in research centres, robotic operating rooms or self-driving port transport. In addition, FRP have a higher strength and are lightweight, unlike steel. The modulus of elasticity, on the other hand, is many times lower than steel.

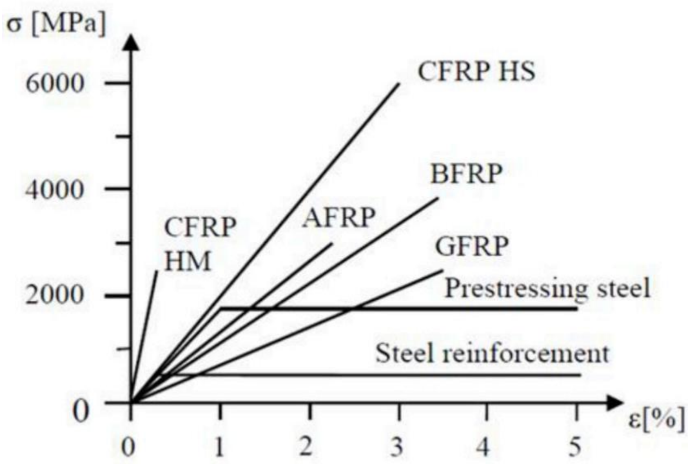

Figure 2.1.1.2: FRP stress/strain curve; AFRP(aramid), BFRP(basalt), CFRP(carbon,) GFRP(glass), (Xu, Rawat, Shi, & Zhu, 2019)

Aramid FRP
Aramid fibres, also referred to as aromatic polyamide fibres, represent a category of organic fibres characterized by their exceptionally low specific gravity and high tensile strength-to-weight ratio among the current reinforcing fibres. Aramids are commercially recognized under names such as Kevlar, Technora, and Twaron. Despite their superior mechanical properties, the higher cost of aramid fibres compared to glass and basalt fibres limits their widespread use in structural applications (Prince-Lund Engineering, 2019).
Moreover, aramid fibres absorb more water compared to other fibre materials, necessitating meticulous storage and project planning until they are impregnated with a polymer matrix. Increased moisture levels can induce internal cracking at pre-existing micro-voids, leading to longitudinal splitting. Although aramid fibres demonstrate resistance to numerous chemicals, they are susceptible to degradation by certain acids and alkalis (fib bulletin 40, 2007).

Basalt FRP
Basalt fibres exhibit a tensile strength superior to that of E-glass fibres, while being comparable to S-glass fibres. Economically, basalt fibres are comparable to glass fibres, while being significantly more cost-effective than carbon fibres. Additionally, basalt fibres demonstrate enhanced resistance to the alkaline and acidic environments typically found in concrete, surpassing the performance of both E-glass and S-glass fibres in this regard. The exploration of basalt fibres as a structural reinforcement material for concrete structures remains in the developmental phase (fib bulletin 40, 2007).

Carbon FRP
Carbon fibres exhibit exceptional tensile strength and stiffness, surpassing even that of steel. Their tensile modulus and strength remain stable with increasing temperature, and they exhibit high resistance to harsh environmental conditions. Carbon fibres also fail in a brittle manner and behave elastically up to the point of failure. However, a significant drawback of carbon fibres is their high cost, which is 10 to 30 times greater than that of E-glass fibres. The high cost is caused by expensive raw materials and the long processes of carbonization and graphitization required for their production (fib bulletin 40, 2007).
In addition to their cost, the environmental impact of CFRP is considerably higher compared to steel and other FRP. Research by Stoiber, Hammerl, & Kromoser (2020) has shown that even when normalizing the environmental impact per N/mm^2 of tensile strength, CFRP still exhibits a significantly higher environmental cost than steel. Their research was based on an LCA “cradle-to-gate” analysis according to EN 158054.

Glass FRP
Glass fibres are the most widely used reinforcing fibres for FRP applications. These fibres are available in various types, including E-glass, S-glass, and alkali-resistant glass. E-glass is primarily made from silica, alumina and calcium oxide. Because of these components it is known for its good electrical insulation properties, moderate strength, and resistance to moisture. S-glass, on the other hand, contains higher amounts of silica, magnesium oxide, and aluminium oxide, offering higher tensile strength, higher stiffness, and better resistance to heat and impact compared to E-glass. Furthermore, alkali-resistant glass contains a significant amount of zirconia (over 17%) to enhance alkali resistance (GRCA International, 2019). This glass composition is specifically designed to resist degradation in alkaline environments, making it highly durable in concrete and cement applications.
E-glass is the most economical among these types and is extensively utilized in the FRP industry. S-glass, on the other hand, offers higher tensile strength and E-modulus compared to E-glass, but its higher cost limits its popularity (fib bulletin 40, 2007). Regarding mechanical properties, the primary distinction between BFRP and GFRP rebars lies in their temperature

resistance. GFRP rebar and mesh retain their properties up to 200°C, whereas BFRP can endure temperatures up to 400°C. However, both types of fibres are coated with the same resin matrix during production, and the thermal tolerance of this matrix is more critical than that of the fibres themselves. Therefore, there is no significant difference in thermal tolerance between GFRP and BFRP (Zhon Sheng, 2023).

Table 2.1.1: Fibre type comparisons

Fibre type	Advantages	Disadvantages	References
Aramid FRP	Low density Cheaper than carbon	More expensive than basalt and glass High water absorption Susceptible to degradation by certain acids and alkalis	(Prince-Lund Engineering, 2019) (fib bulletin 40, 2007)
Basalt FRP	Tensile strength superior to E-glass Same cost as glass Cheaper than carbon Very high chemical resistance	Tensile strength lower than carbon E-modulus lower than carbon	(fib bulletin 40, 2007)
Carbon FRP	Tensile strength and E-modulus even higher than steel Stable at high temperatures High resistance to harsh environmental conditions	Very high cost High environmental impact	(fib bulletin 40, 2007) (Stoiber, Hammerl, & Kromoser, 2020)
Glass FRP	Low cost (E-glass even lower than S-glass and alkali-resistant glass) Electrical insulation(E-glass)	Low tensile strength E-glass and alkali-resistant glass	(fib bulletin 40, 2007) (Zhon Sheng, 2023)

Fibre type	Density ρ [kg/m^3]	Tensile strength f_u [MPa]	Young's modulus E [GPa]	Strain at failure ε_u [%]
Carbon (high modulus)	1950	2500-4000	350-650	0.5
Carbon (high strength)	1750	3500	240	1.1
Aramid (Kevlar49)	1440	3620	124	2.2
S-glass	2500	4580	86	3.3
E-glass	2500	3450	72	2.4
Basalt	2800	4840	89	3.1

Figure 2.1.1.3: Properties of fibre types (fib bulletin 40, 2007)

As mentioned in Section 1.2 only BFRP will be considered for the remainder of this study. This choice is based on the properties as described above. In short: little is known about BFRP and there is therefore a need for additional research. CFRP is too expensive and not environmentally friendly. AFRP and GFRP have a lower resistance to alkalis and acids than BFRP and AFRP also has a greater water absorption.

2.1.2 BFRP history

The first person to conceive the idea of producing basalt fibres was the Frenchman Paul Dhe, who patented it in 1923 under patent US1462446A (United States Patent Office, 1923). In the 1960s, the Soviet Union investigated the potential applications of basalt fibres, primarily for military purposes, focusing on armour protection capabilities. Compared to other bulletproof fibre types such as glass, aramid, and ultra-high molecular weight polyethylene, basalt exhibits an exceptionally excellent cost performance. It is also highly resistant to strong alkaline conditions, possesses higher tensile strength, and is more fire-resistant than the alternatives (Fu, et al., 2020).
In 1985, basalt fibres were first commercialized in Ukraine. After the fall of the Soviet Union in 1991, it was decided to make Soviet research on basalt fibres publicly available for civil applications. This led to further technological development and a reduction in costs, making it more attractive for commercial purposes.

2.1.3 Basalt rebar production

Basalt is a volcanic rock that is found abundantly on the Earth's surface. About 30% of the earth's crust consists of basalt. Basalt fibres are obtained by melting crushed washed volcanic lava rock at approximately 1400 degrees Celsius. The liquid rock is then extruded through multiple tip bushings to make fibre 13 to 19 microns in diameter. These fibres are rolled up on large rolls. The fibres are then bundled by pultrusion technique, using an epoxy resin to form a rebar.
During the production process of BFRP, just like the production of steel reinforcement, a significant amount of heat is generated. In fact, more heat is required per unit of weight for BFRP than for steel. However, the volumetric density of BFRP is four times lower than that of steel. Consequently, the environmental impact (ECI) per bar diameter is approximately 40 to 50% lower for BFRP compared to steel (Leenders, 2024). The rebars can be produced with various types of profiling. The most common profiles are smooth, ribbed, and sand-coated. The type of profiling will ultimately influence the bond characteristics between the concrete and the rebar.

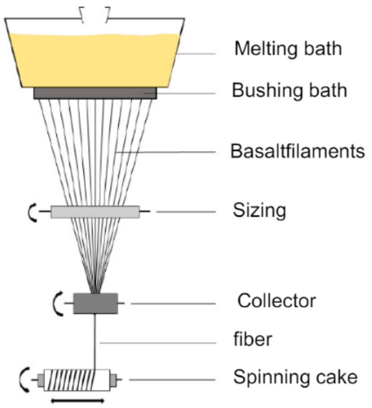

Figure 2.1.3.1: Production microfibre rolls (Deutsche Basalt Faser, 2021)

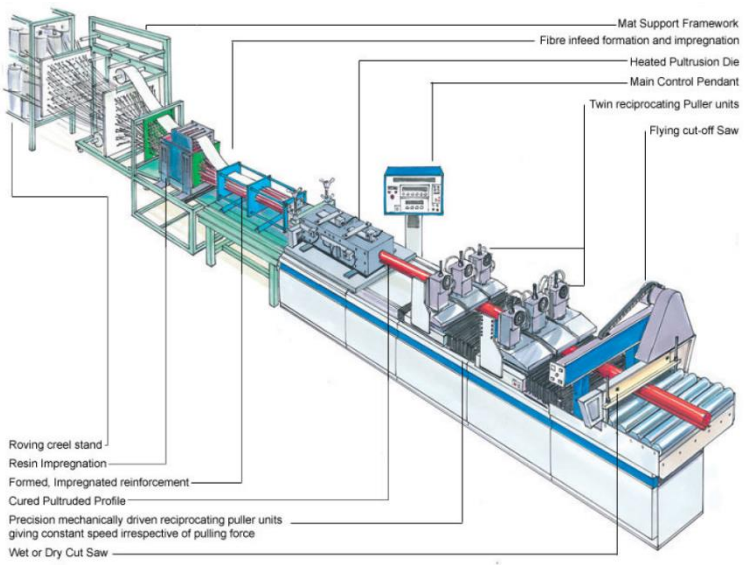

Figure 2.1.3.2: Pultrusion technique (Orlitech, 2024)

2.1.4 BFRP manufacturers

A study conducted by Schmidt et al. (2019) mapped the global production of BFRP. They collected information from 23 different BFRP manufacturers across 10 different countries. These manufacturers are all based in North America, Europe, or Asia. Notably, most manufacturers began producing BFRP relatively recently; over 50% started after 2007, while only 20% started before 2000 (Schmidt, Kampmann, Telikapalli, Emparanza, & Caso, 2019). Which again shows the increasing global interest in this innovative material.

Manufacturer		Country	State	City
ID	Name			
RAW	Nor Rust Rebar Inc	USA	Florida	Pompano Beach
SBS	Smarter Building System	USA	Rhode Island	Newport
NVC	Neuvokas Corp.	USA	Michigan	Ahmeek
KOD	KODIAK Fiberglass Rebar	USA	Texas	Houston
AFT	Advanced Filament Technologies	USA	Texas	Houston
USB	US Basalt	USA	Texas	Richmond
PPC	Proven Performance Chemicals	USA	Georgia	Bogart
PAL	Pultrall Inc.	Canada	Quebec	Thetford Mines
AKI	Armkar Inc.	Canada	Ontario	North York
ICT	Incotelogy GmbH	Germany	NRW	Pullheim
DBF	ASA. TEC GmbH	Germany	Sachsen-Anhalt	Sangerhausen
ASA	Basalt Technologies UK Limited	Austria	Lower Austria	Langenlois
BTL	ReforeTech AS	England	London	London
RAS	Technobasalt-Invest	Norway	Buskerud	Røyken (Office Melbourne, FL)
TBI	Galen	Ukraine	Kiev	Kiev
GPA	Rusano (TBM)	Russia	Chuvashia	Cheboksary
RSN	Armastek	Russia	Moscow	Moscow
ARM	GMV	Russia	Perm Krai	Perm
GMV	Phoenix New Material Co., Ltd.	China	Jiangsu	Nanjiing
PNM	GBF Basalt Fiber Co., Ltd	China	Gansu	Lanzhou
GBF	GBF Basalt Fiber Co., Ltd.	China	Zhejiang	Hangzhou
HGM	Huabin General Machinery Co.,Ltd.	China	Hebei	Hebei
FIE	Filips India Engineering	India	Mumbai	Mumbai

Figure 2.1.4.1: BFRP manufactures (Schmidt, Kampmann, Telikapalli, Emparanza, & Caso, 2019)

At the time of the study, up to 2019, North America had seven manufacturers, Europe had six, and Asia had eight. Furthermore, Russia and Ukraine have numerous "garage BFRP producers" who produce pultruded basalt products during the warmer months. These "manufacturers" were not included in the study by Schmidt et al. (2019) because their product quality does not meet the standards required for public construction projects.

The most common surface enhancements were found to be helical wrap, helical rib, and sand coat. The most significantly used resin type was epoxy.

Manufacturer	Cross-Sectional Shape	Fiber Type	Resin Type	Surface Enhancement	Produced Diameters
RAW	Round (solid)	Basalt	Epoxy	Helical wrap & Sand coat	#1, 2, 3, 4, 5, 6, 7, 8, 9, 10, 11
SBS	Round (solid)	Basalt	Epoxy / Vinyl Ester	Helical wrap	#1, 2, 3, 4, 5, 8
NVC	Round (solid)	Basalt	Epoxy	-	#3
KOD	Round (solid)	Basalt/Glass	Epoxy / Vinyl Ester	Helical wrap/rib & Sand coat	#2, 3, 4, 5, 6, 7,8
AFT	Round (solid)	Basalt	Epoxy	Helical wrap	#1, 2, 3, 4, 5, 6, 7, 8, 9, 10, 11
USB	-	Basalt	-	-	-
PPC	-	Basalt	-	-	-
PAL	Round (solid)	Basalt/Glass	Epoxy	Sand coat	#2, 3, 4, 5, 6, 7, 8, 9, 10, 11
AKI	-	Basalt	-	-	-
ICT	-	Basalt	-	-	-
DBF	Round (hollow)	Basalt	Thermoset	Sand coat	#1, 2, 3, 4, 5
ASA	Round (solid)	Basalt	Vinyl Ester	Helical rib	#2, 3, 4, 5, 6, 8
BTL	-	Basalt	-	-	-
RAS	-	Basalt	-	-	-
TBI	Round (solid)	Basalt	Epoxy	Helical rib	#1, 2, 3, 4
GPA	Round (solid)	Basalt/Glass	Epoxy	Sand coat	#1, 2, 3, 4, 5, 6, 7, 8, 9, 10, 11
RSN	-	Basalt	-	-	-
ARM	Round (solid)	Basalt/Glass	Epoxy	Helical wrap & Sand coat	#1, 2, 3, 4, 5, 6, 7, 8, 9, 10, 11
GMV	-	Basalt		-	-
PNM	-	Basalt	-	-	-
GBF	-	Basalt	-	-	-
HGM	-	Basalt	-	-	-
FIE	-	Basalt	-	-	-

Figure 2.1.4.2: BFRP rebars produced by manufacturers (Schmidt, Kampmann, Telikapalli, Emparanza, & Caso, 2019)

2.1.5 BFRP rebar properties

BFRP consists of two materials: basalt fibres and resin matrix. The high-strength basalt fibres are embedded and bonded together by the low-modulus polymeric matrix. The primary functions of the resin matrix are to bind the basalt fibres, distribute stresses to all other fibres in the rebar and protect their surfaces from damage during handling, fabrication, and service life. This chapter will first examine the properties of the individual basalt fibres and resin matrix, and then discuss the properties of the composite BFRP.

Basalt fibre

Basalt fibres are exceptionally strong and lightweight. These fibres are stronger than raw basalt rock due to the pultrusion process, which orients the molecules in a preferential direction along the fibre. This orientation results in fewer defects, thereby increasing the strength of the fibres compared to the raw basalt material (fib bulletin 40, 2007). Basalt fibres behave in a linearly elastic manner, like other FRP materials. The table below presents the properties of basalt fibres.

Fibre Type	ρ [kg/m³]	f_u [MPa]	E [GPa]	ε_u [%]	α [10^{-6}/°C]	ν [-]
E-glass	2500	3450	72.4	2.4	5	0.22
S-glass	2500	4580	85.5	3.3	2.9	0.22
Alkali resistant glass	2270	1800-3500	70-76	2.0-3.0	-	-
ECR	2620	3500	80.5	4.6	6	0.22
Carbon (high modulus)	1950	2500-4000	350-650	0.5	-1.2…-0.1	0.20
Carbon (high strength)	1750	3500	240	1.1	-0.6…-0.2	0.20
Aramid (Kevlar 29)	1440	2760	62	4.4	-2.0 longitudinal 59 radial	0.35
Aramid (Kevlar 49)	1440	3620	124	2.2	-2.0 longitudinal 59 radial	0.35
Aramid (Kevlar 149)	1440	3450	175	1.4	-2.0 longitudinal 59 radial	0.35
Aramid (Technora H)	1390	3000	70	4.4	-6.0 longitudinal 59 radial	0.35
Aramid (SVM)	1430	3800-4200	130	3.5	-	-
Basalt (Albarrie)	2800	4840	89	3.1	8	-

Figure 2.1.5.1: Typical properties of fibres for FRP composites (fib bulletin 40, 2007)

Resin matrix

The primary functional and structural requirements of a resin matrix are to hold the reinforcing fibres together, transfer and evenly distribute the load to the fibres, and protect the fibres from environmental damage and mechanical abrasion. The most used matrix types are: polyester, epoxy and vinyl ester. Their advantages and disadvantages are given below.

Epoxy resins

Advantages
- High mechanical properties
- Easy processing
- Low shrinkage during cure → good bond
- High chemical resistance
- Less affected by water

Disadvantages
- Relatively high cost
- Long curing period

Polyester resins

Advantages
- Good UV resistance
- High durability
- Resistance to fibre erosion
- Cost-effective

Disadvantages
- High volumetric shrinkage

Vinyl ester resins

Advantages
- More flexible
- Chemical resistance

Disadvantages
- High volumetric shrinkage
- Fewer crosslinks

Property	*Matrix*		
	Polyester	Epoxy	Vinyl ester
Density (kg/m³)	1200 - 1400	1200 - 1400	1150 - 1350
Tensile strength (MPa)	34.5 - 104	55 - 130	73 – 81
Longitudinal modulus (GPa)	2.1 – 3.45	2.75 – 4.10	3.0 – 3.5
Poisson's coefficient	0.35 – 0.39	0.38 – 0.40	0.36 – 0.39
Thermal expansion coefficient (10^{-6}/°C)	55 - 100	45 - 65	50 - 75
Moisture content (%)	0.15 – 0.60	0.08 – 0.15	0.14 – 0.30

Figure 2.1.5.2 Typical properties of thermosetting matrices (fib bulletin 40, 2007)

During use phase, as embedded reinforcement, UV resistance of the matrix is not an issue since UV radiation cannot reach the rebars. However, low UV resistance of the FRP rebar can cause a problem during material storage. FRP rebars that are sensitive to UV radiation must therefore be stored in an enclosed or dark environment to prevent UV degradation. FRP with polyester resins exhibit good UV resistance, making them highly suitable for external reinforcement or external strengthening of existing structures. The drawback of this polyester matrix is its high volumetric shrinkage. Since the fibres themselves do not shrink, this causes internal stresses, potentially leading to micro-cracks in the rebar. This deterioration impairs the ability to transfer stresses from the resin matrix to the microfibers.
In practice, despite the higher costs, epoxy is often preferred as the resin matrix material. The superior processing, low shrinkage, high chemical resistance, and excellent mechanical properties are favoured over the higher cost. This phenomenon is also reflected in Figure 2.1.4.2, where most manufacturers choose epoxy as their resin type.

BFRP rebar
The properties of BFRP can vary significantly due to factors such as the production process, the ratio and orientation of the fibres, type of resin used, and the quality control measures implemented by the manufacturer. According to the ASTM D 2584 “Standard Test Method for Ignition Loss of Cured Reinforced Resins” the fibre content shall not be less than 55% by volume or 70% by mass (ASTM D 2584, 2011). The mass fibre fraction of 85%, is considered as baseline, as provided by the manufacturers (Pavlovic, Donchev, Petkova, & Staletovic, 2022).
The tensile strength of BFRP can be up to approximately three times higher than that of B500 reinforcing steel, while its modulus of elasticity is about three to five times lower. Furthermore, BFRP does not exhibit yielding behaviour and behaves in a fully linear elastic manner up to its fracture strain.
A disadvantage of BFRP is that its tensile strength decreases over time. Reinforcing bars that are subjected to constant stress for prolonged periods can experience sudden failure, a phenomenon known as creep rupture. The stress level at which creep rupture occurs can be reduced under adverse environmental conditions such as high temperatures, exposure to UV radiation, wet-dry cycles, or freeze-thaw cycles (ACI 440.1R-15, 2015).

Like all other FRPs, BFRP is also magnetically neutral, making it highly suitable for applications involving wireless communication or sensitive sensors, such as: the construction of robot operating rooms or self-driving trucks in harbour areas.
The most important advantage of BFRP, in contrast to steel, is that it does not corrode and compared to other fibres such as S-glass, carbon or aramids used in concrete, they are also considered to be inexpensive (Nasvik, 2016). Another advantage of basalt compared to other FRP materials is that it has a high fire resistance and it does not require separation after the use phase, as is often the case with other types of reinforcement. The basalt rebars can be recycled along with the concrete in a single treatment, as basalt is also a type of rock. Separation of rebar and concrete is therefore not necessary (Ruiz, 2022).

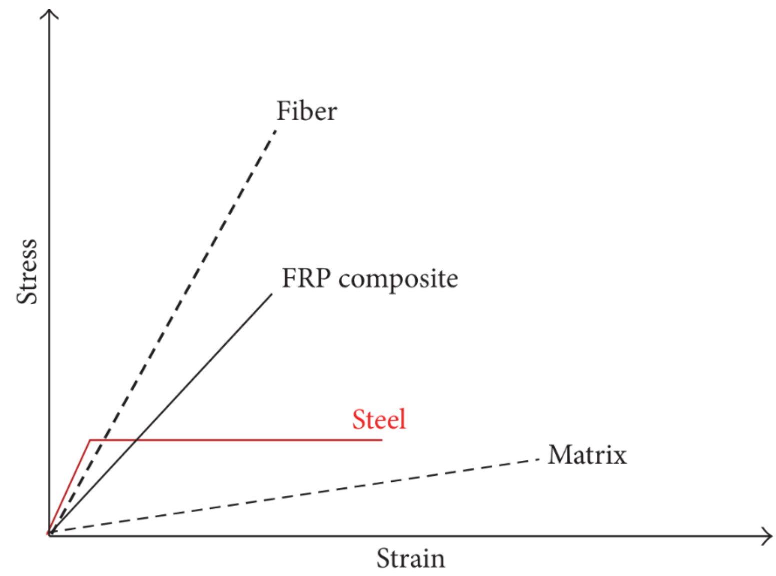

Figure 2.1.5.3: Typical stress-strain curves for fibre, matrix, steel and FRP composite (Kang, 2017)

Table 2.1.5: Basalt rebar properties (fib Model Code for Concrete Structures, 2020)

Property	**BFRP**	**Steel (B500)**
Tensile strength: f_f [MPa]	550 – 1800	500
E-modulus: E_f [GPa]	40 - 70	210
Ultimate strain: ε_{fy} [%]	1,2 – 3,4	5

2.1.6 BFRP sustainability

Pavlovic et al. evaluated the environmental impact of BFRP through a life cycle assessment (LCA) study. In this study, they examined the extent to which BFRP enhances the sustainability of structures compared to other reinforcement materials. The materials considered in this study include BFRP, traditional steel, GFRP, galvanized steel, and stainless steel.

LCA system boundaries

LCA is a standardized method for measuring and comparing the environmental impact arising from the production, use, and disposal of a product. The globally recognized standardized procedures for an LCA analysis are outlined in ISO 14040 for the 'principles and framework' and ISO 14044 for an outline of 'requirements and guidelines.'
The system boundary for the LCA study by Pavlovic et al. (2022) includes all material extraction, transportation, processing, and associated energy consumption up to gate. This system boundary corresponds to the production stage, or in LCA terms, modules A1-A3. The construction process stage (modules A4 &A5), use stage (modules B1-B5) and end-of-life stage (modules C&D) for BFRP still contain too much uncertainty. Including these modules in the LCA procedure would introduce an excessive level of uncertainty into the analysis.

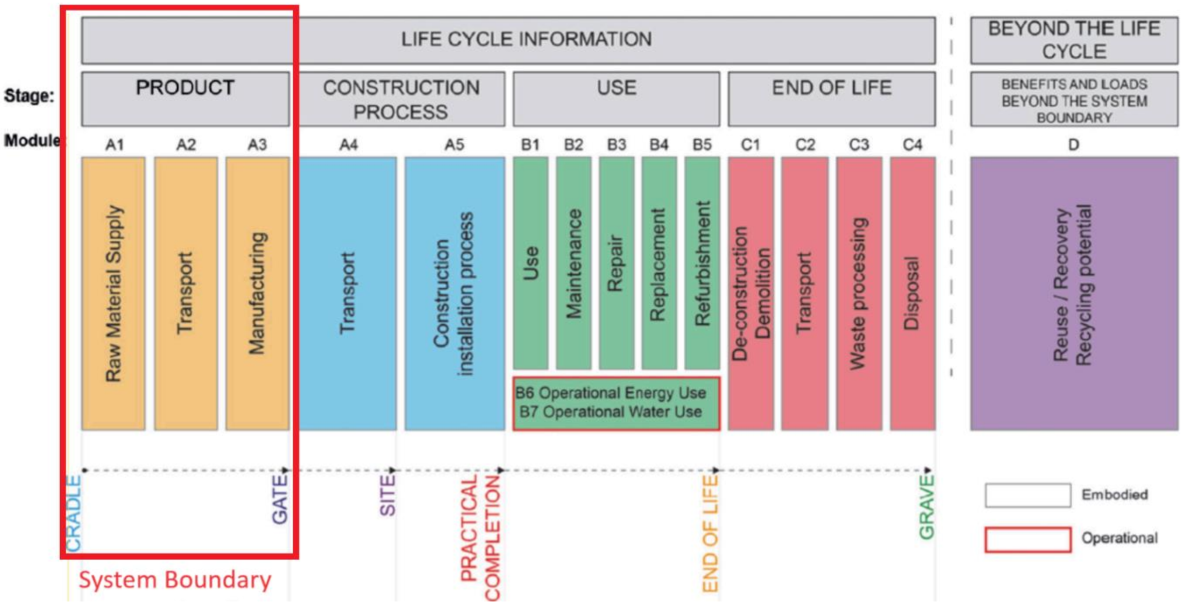

Figure 2.1.6.1: System boundary within scope of LCA (Orr & Gibbons, 2020)

Fibre/resin content

Given that epoxy is by far the most used resin material, this LCA study incorporates epoxy as the resin component (Schmidt, Kampmann, Telikapalli, Emparanza, & Caso, 2019). According to Bagherpour (2012), the most used fibre content in FRP is about 80% by mass, therefore this assumption was adopted for the LCA study. A higher fibre content poses the risk that not all fibres will be adequately surrounded by the resin matrix. The greatest environmental burden from BFRP arises from the resin component.

Steel

In the LCA study, distinctions were made between various types of steel and methods used to produce the rebar. The study considered standard reinforcing steel, stainless steel, and galvanized steel. Additionally, different proportions of recycled steel were considered.

There are two production methods for steel: basic oxygen furnace (BOF) and electric arc furnace (EAF). BOF uses virgin iron ore as input, with scrap used only as a cooling agent, whereas EAF can use up to 100% scrap. According to Swann (2021), the production ratio between BOF and EAF in Europe is 60/40, and this ratio was used in this analysis.

LCA Results

The results of the study by Pavlovic et al. (2022), based on the ISO 14040:2006 framework, indicate that the resin component significantly impacts the sustainability of BFRP. A parameter study on the fibre content showed the sensitivity of fibre content for 18 LCA midpoint categories. The highest sensitivity can be observed in the case of terrestrial ecotoxicity (TE) . A change in fibre fraction of 15% can influence the environmental midpoint category of TE of BFRP by 42.5%.

Comparison of BFRP with steel in the Cradle-to-Gate Life Cycle Impact Assessment shows that BFRP has a significantly lower environmental impact than even 100% recycled reinforcing steel. Regarding non-recycled steel, the difference is even more pronounced.

The global warming potential of BFRP is 74% lower than that of traditional steel reinforcement, per unit volume. For 100% recycled steel, this difference is 22%; for galvanized steel, it is 49%; for stainless steel, it is 88%; and for GFRP, it is 44%.

Table 2.1.6: Global warming potentials, BFRP vs alternatives (Pavlovic, Donchev, Petkova, & Staletovic, 2022)

Material	Relative Global Warming potential/unit volume
BFRP vs stainless steel	-88%
BFRP vs traditional steel	-74%
BFRP vs galvanized steel	-49%
BFRP vs GFRP	-44%
BFRP vs 100% recycled steel	-22%

2.1.7 Existing applications of BFRP

In this paragraph, a brief overview of some reference projects where basalt fibre reinforcement has already been applied will be provided. These projects demonstrate that it is an innovation that is still in its infancy, as BFRP has not yet been utilized for challenging applications with high consequence classes. Presently, the applications of BFRP primarily encompass sound barriers, flooring, or other structures with minimal risks. Nevertheless, these projects already exhibit a significant reduction in CO2 emissions. This underscores the necessity for further research so that BFRP may potentially become a widely utilized material in the future

Bus depot Breda

The 2500 m^2 prefabricated fire wall panels of this bus depot will consist entirely of panels made with BFRP. By utilizing BFRP instead of traditional steel in this project, a reduction in environmental impact of 31% and a CO2 reduction of 8% have been achieved in the production phase, specifically in LCA phases A1 through A3 (Leenders, 2024). The design standards used consist of a combination of BRL0513 and ACI 440.1R-15. The design formulas for the capacities are derived from BRL0513. ACI 440.1R-15 was used to determine the long-term tensile strength of BFRP because BRL0513 provides a very conservative value. Additionally, a material factor of 1,5 was used in accordance with BRL0513.

Maasvlakte Rotterdam

On the Maasvlakte in the Port of Rotterdam, a new floor will be installed for the transportation of goods by electric autonomous trucks. The contractor, Dura Vermeer, has also opted to utilize BFRP in this context due to basalt's electromagnetic neutrality, thereby reducing the likelihood of wireless signal disruptions (Hoven, 2023).

Swimming pool Rhode Island

The construction of a swimming pool is also extremely suitable to the application of BFRP. In this example in Rhode Island, BFRP was chosen because basalt is lighter and thus more easily to handle, it lacks sharp edges that could injure workers, and it does not corrode, thereby quiring less maintenance. The latter is particularly advantageous given the difficulty of conducting maintenance on an in-ground pool, where accessibility is limited (Basalt.Guru, 2016).

Figure 2.1.7: BFRP in swimming pool (Basalt.Guru, 2016)

Thompson’s Bridge

This project involves the replacement of the bridge on the A509 in Fermanagh County over the Cladagh River in Northern Ireland. The bridge consists of four prestressed U-girders with an in-situ cast bridge deck that is 200 mm thick. In the middle section of the span, Ø12 BFRP bars are used. Near the supports and edges, traditional Ø12 steel reinforcement is applied. The reinforcement ratio for the basalt bars is 0.6%, and for the steel bars, it is 0.7%. The span of the U-girders is 32 m. The span of the bridge deck is 1.4 m between two U-girders and 1.6 m between the two webs of a single girder (Zhou, Zheng, & Taylor, 2018). The bridge deck is designed based on compression membrane action according to the Highway Agency guidance BD 81/02. The vertical deflection with BFRP is less than with steel reinforcement, despite the lower modulus of elasticity of BFRP and slightly less reinforcement. Taylor (2024) suspects that this is due to deviations in concrete quality rather than the reinforcement itself, as the design is based on compression membrane action, which assumes concrete in compression.

Approach slab pilot

In a pilot project by Rijkswaterstaat, approach slabs were constructed with BFRP reinforcement and equipped with sensors for measurements. The approach slabs were placed on a site and are subjected to daily loads from truck traffic. The aim of this research is to gain insight into the behavioral changes of the approach slabs over time (or the absence of changes) (ASCEM, 2023). Findings from the pilot include: significant variations in material properties, bends in BFRP are very weak and should be avoided, BFRP failure behavior is 100% brittle, and actively determining material properties is crucial.

Innovation Bridge

The Innovation Bridge is a bridge constructed at the University of Miami. The pedestrian bridge contains no steel, only concrete, GFRP, CFRP, and BFRP. These rebar materials were chosen to make the bridge maintenance-friendly, as the rebars do not corrode in the aggressive subtropical climate of Florida, ensuring a service life of up to 75 years. GFRP and BFRP are used as reinforcement, while CFRP provides the prestressing in the girders. Furthermore, it serves as field-proof for the development and validation of the next generation of design and construction guidelines for FRP-reinforced concrete. The ACI 440 standards were used in the design (Rossini, Spadea, & Nanni, 2019).

Table 2.1.7: BFRP existing applications

Project	Reason for application	Design approach	Lessons learnt/conclusions
Bus depot Breda	Sustainability and non-corroding	BRL0513 & ACI440.1R-15	- ECI reduction 31% on rebar - No comprehensive European standards - Shear force is governing - Curved rebar is a problem
Maasvlakte Rotterdam	Electromagnetic neutrality	Unknown	- Better wireless communication
Swimming Pool Rhode Island	Lightweight, better handling and non-corroding	Unknown	- Less heavy construction work - Safer working conditions
Thompson's Bridge	Durability, lightweight and highstrength	BD 81/02	- Using CMA leads to more sustainable bridge deck designs - Proof loading showed excellent safety
Approach slab	Sustainability and non-corroding	Unknown	- Bends difficult and weak - Determine material properties
Innovation bridge	Little maintenance, unify design approaches to FRP-RC and FRP-PC	ACI 440.1R-15 & ACI 440.4R-04	- GFRP and BFRP have same mechanical properties - CFRP for prestress - BFRP rebar in deck and girders - GFRP rebar in deck

2.1.8 BFRP-RC design considerations

When a strong bond between rebar and concrete is established, forces can be successfully transferred to the rebar. Bond properties between BFRP and concrete differ in several respects from those of steel and concrete. In the case of steel reinforcement, the bond is primarily due to the mechanical action of the bar lugs against the concrete. Once the tensile strength of the concrete is exceeded, primary cracks, often extending to the surface, appear. Subsequently, secondary cracks form, which are mainly inclined and trapped within the concrete matrix. Bond failure usually occurs due to crushing of the concrete in the vicinity of the lugs.
In the case of BFRP reinforcement, which has a lower modulus of elasticity and less pronounced surface undulations, the bond is more frictional in character. Bond failure in BFRP typically occurs due to partial failure in the concrete and some surface damage to the BFRP (fib bulletin 40, 2007).

This section will consider bond through bond development, tension stiffening, and splitting resistance.

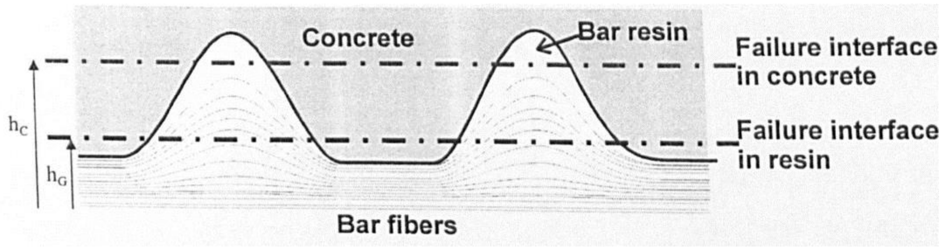

Figure 2.1.8.1: FRP failure bond: partial concrete failure and FRP surface failure (Achillides, 1998)

Bond development

The interaction between reinforcing bars and the surrounding concrete can be described using the theoretical model of bond stress-slip behaviour introduced by Tassios (1979), as illustrated in Figure 2.1.8.2.

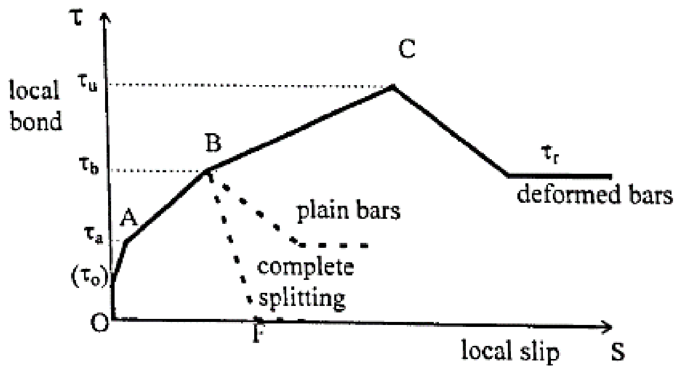

Figure 2.1.8.2: Theoretical model of local bond-slip relationship (Tassios, 1979)

In this model, several stages can be distinguished:

- *Up to τ_0:* There is no slip between the rebar and the concrete. The resistance mechanism is entirely dependent on the chemical adhesion between the rebar and the concrete.
- *τ_0 to τ_a*: As the pullout force increases, the chemical bond breaks, and a new type of bonding occurs. This bonding depends on the surface properties of the rebar and is

referred to as mechanical bonding. The irregularities on the rebar induce bearing stresses in the surrounding concrete. In this stage, the first slip is noticeable, and initial microcracks appear because of exceeding the concrete tensile strength. As seen in the graph, there is a slight decrease in the slope, indicating a reduction in bond stiffness.

- τ_a *to* τ_b: The further formation of microcracks modifies the response of the concrete under loading. The concrete stiffness decreases, and therefore, larger slip increments are required for further bond stress increments than before cracking. The radial forces induced by the surface of the rebar are balanced against the tensile stress rings in the surrounding concrete. When the tensile stresses in these stress rings exceed the tensile strength of the concrete, splitting cracks form along the rebar. If these splitting cracks penetrate through the concrete cover, the bond fails suddenly, as indicated at point F in Figure 2.1.8.2.
- τ_b *to* τ_u: However, if the splitting resistance of the surrounding concrete is sufficiently high (due to a thick concrete cover or adequate transverse reinforcement), the pullout force can be further increased. The maximum bond resistance can then be achieved, as indicated at point C in Figure 2.1.8.2. Failure can then occur through various mechanisms: low laminar shear strength between fibres or shear bar deformations, concrete shear failure due to localized peak stresses at bar deformations, or squeezing through concrete due to the low transverse stiffness of BFRP, or a combination of these (fib bulletin 40, 2007).
- τ_u *to* τ_r: After this stage, the bonding mechanism is frictional resistance between the rebar and the concrete in the cylindrical surface where shear failure occurred.

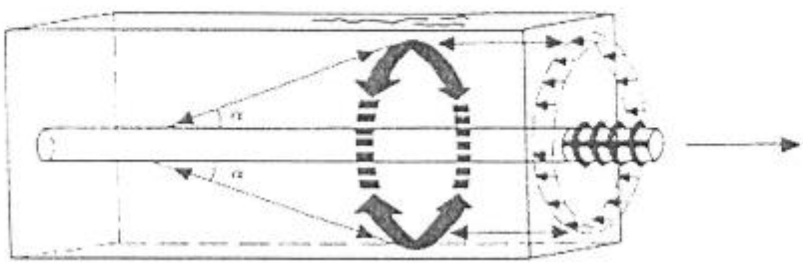

Figure 2.1.8.3: Balancing radial components bond forces against tensile stress rings in concrete in an anchorage zone (Tepfers, 1979)

Angle (α) depends on the properties of the concrete and rebar: E-modulus, concrete shear strength, shape, and surface deformations of the rebar**.**
The shear stiffness of FRP bars primarily depends on the shear stiffness of the bar's resin and the shear strength at the resin-fibre interface. When an FRP bar is subjected to tensile forces, differential movement can occur between the core and surface fibres. This results in an uneven distribution of normal stresses across the bar's cross section. An example of this stress distribution is illustrated in Figure 2.1.8.4.

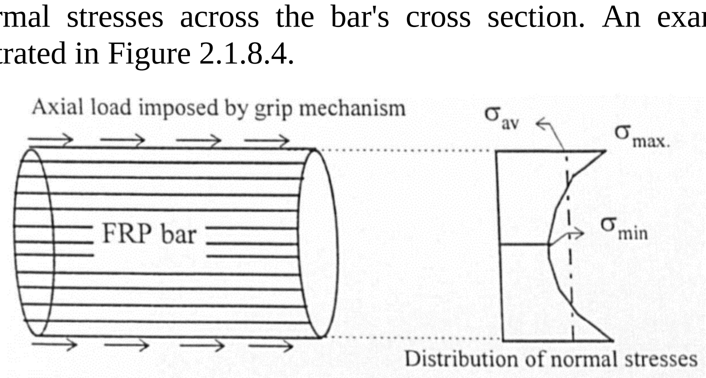

Figure 2.1.8.4: Distribution of normal stresses on FRP bar (Achillides, 1998)

Cover, bar spacing and formation of splitting

In addition to the properties of the concrete and the reinforcing bars themselves, the orientation of the reinforcing bars relative to each other and to the entire concrete cross-section is also crucial for the development of splitting cracks. When an insufficient concrete cover is maintained, side splitting can occur, which can cause spalling of the concrete. The spalling of the concrete due to side splitting results in a decrease in the beam's capacity. In the case of a single reinforcing bar, local bond failure can occur in the form of V-notch splitting and corner splitting. Failure does not necessarily lead to a decrease in the beam's capacity if the other bars, aside from the failing bar, maintain their performance. However, the beam cannot perform as expected in terms of flexural capacity (Nishimura, Onishi, & Kawazu, 2020).

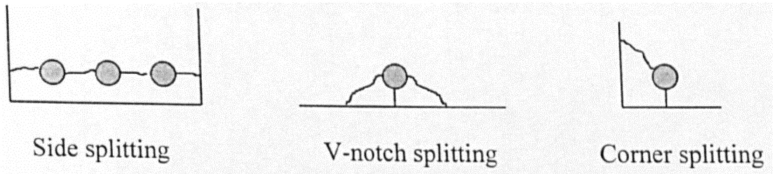

Figure 2.1.8.5: Formation of splitting cracks (Nagatomo, Matsubara, & Kaku, 1992)

BFRP surfaces

As previously described, the most commonly available surface types for BFRP in Europe are sand-coated, helically grooved, and helically wrapped. These three different surface types each have a significant effect on the bond behaviour between the BFRP and the concrete. Various studies have been conducted to investigate the differences between these surface types of rebars. However, it is challenging to draw a clear conclusion regarding which surface characteristics are the best. As Soloyom and Balázs (2020) describe, there are significant differences and conflicting conclusions among the results of earlier research. The variations in bond strength can be explained by the alteration of surface configuration, improvements in material properties, and large deviations in fabrication processes. Additionally, the test setup was found to affect the measurable bond strength (Solyom & Balázs, 2020).

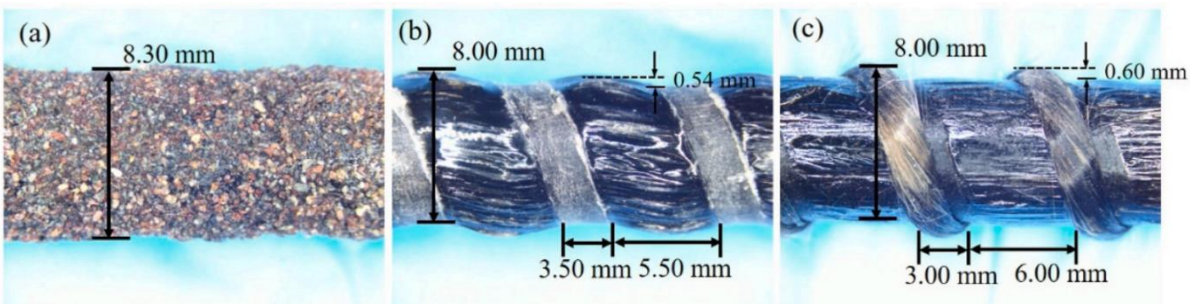

Figure 2.1.8.6: Surface details of BFRP rebars: (a) sand-coated, (b) helically-grooved, (c) helically-wrapped (Feng, et al., 2024)

The bond behaviour principles of each surface type will be discussed below.

Sand coated

The bonding behaviour of sand-coated BFRP is primarily derived from friction. The sand coating increases the effective surface area and creates two shear surfaces. Consequently, a shear surface forms between the concrete and the sand, and another shear surface forms between the sand and the rebar surface. When bonding failure occurs in such bars, it is mainly due to shear failure between the sand and the concrete or between the sand and the rebar surface (Xiong, et al., 2021).

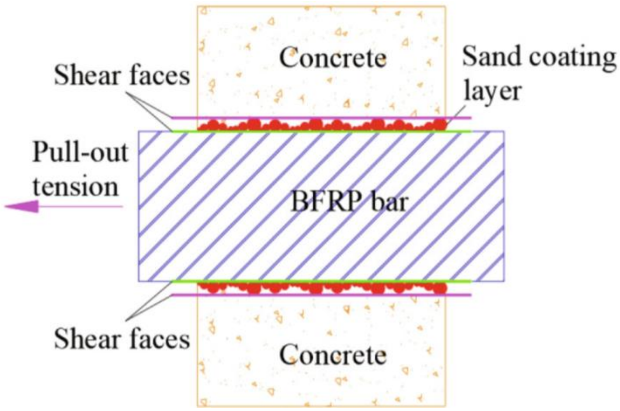

Figure 2.1.8.7: Failure face sand coated BFRP (Xiong, et al., 2021)

Helically grooved

The bonding behaviour between this rebar type and the surrounding concrete is primarily controlled by mechanical interlocking. The concrete ribs, which are in direct contact with the bar ribs, ultimately leads to violent mechanical interlocking that damages the ribs. Consequently, the failure surface occurred at the base of the concrete ribs or bar ribs, resulting in shear failure, as illustrated in Figure 2.1.8.8. In this scenario, the bond strength is governed by the shear strength of the concrete ribs or shear strength of the bar ribs (Xiong, et al., 2021).

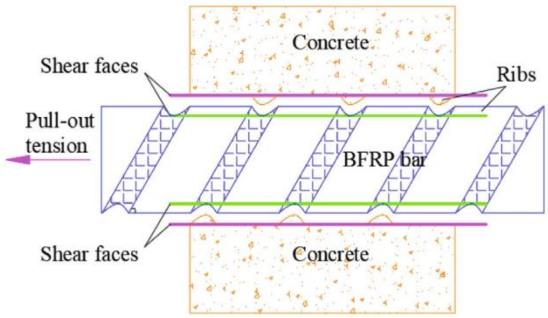

Figure 2.1.8.8: Failure face helically grooved BFRP (Xiong, et al., 2021)

Helically wrapped

In this case, the bond behaviour is also dominated by mechanical interlocking. When relative slip occurs between the concrete and BFRP, mechanical interlocking arises between the concrete ribs, wrapping fibres, and bar ribs. Tests by Xion et al. (2021) have shown that failure in this scenario occurs due to the complete deformation of the concrete ribs and bar ribs, indicating that slippage continued until pull-out failure. The failure surface is the interface between the concrete and the bars. Therefore, the bond strength in this case is determined by the deformation of the ribs.

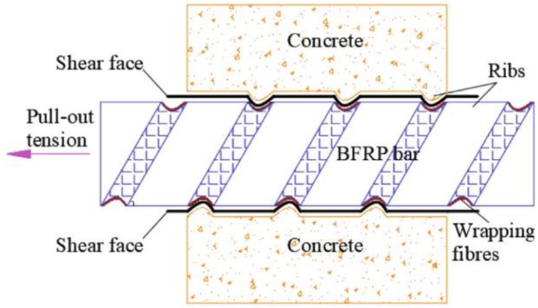

Figure 2.1.8.9: Failure face helically wrapped BFRP (Xiong, et al., 2021)

Durability properties

As previously described by Soloyom and Balázs (2020), the significant variability in material properties makes it difficult to determine which type of rebar surface has the best mechanical properties in terms of bond behaviour. However, there is a clearer distinction between BFRP surface types concerning durability properties.

Among the three different surface types, the sand-coated BFRP exhibits the best durability performance. This is attributed to the protective effect of the sand layer, which serves as an additional barrier against penetrating acids, salts, and other chemicals (Feng, et al., 2024).

Conversely, the worst-performing surface type is the helically grooved one. The grooves in the rebar serve as initial degradation position due to the reduced resin presence in these areas. During the grooving process, some of the resin layer is removed, which leaves some of the basalt fibres less protected and more susceptible to rapid degradation (Feng, et al., 2024).

The durability performance of the helically wrapped surface lies between that of the sand-coated and helically grooved types.

Table 2.1.8: Different BFRP surface properties and their failure mechanisms

Rebar surface type	Bonding behaviour	Failure surface	Governing bond failure mechanism	Durability properties*
Sand coated	friction	Concrete-sand or sand-rebar	Shear failure between concrete-sand or Shear failure between sand-rebar	95,2%
Helically grooved	Mechanical interlocking	Base of concrete ribs or bar ribs	Shear strength concrete ribs or Shear strength bar ribs	75,2%
Helically wrapped	Mechanical interlocking	Interface between concrete and bars	Deformation concrete ribs and bar ribs	91,6%

*bond strength retention after 180 days in aggressive environment (Feng, et al., 2024)

2.2 Shear capacity

The shear capacity of concrete structural elements depends on four contributing factors. The mechanisms that contribute to shear capacity are: contribution offered by the un-cracked compression zone, aggregate interlock, dowel action and, when provided, shear reinforcement. Given that the scope, see Section 1.4, of this project is limited to the cast-in-situ bridge deck on inverted T-beams, where normally no shear reinforcement is applied, shear reinforcement will not be discussed further in this chapter. The subsections that follow will describe how the shear capacity mechanism works and what the influence of BFRP rebar is on these mechanisms.

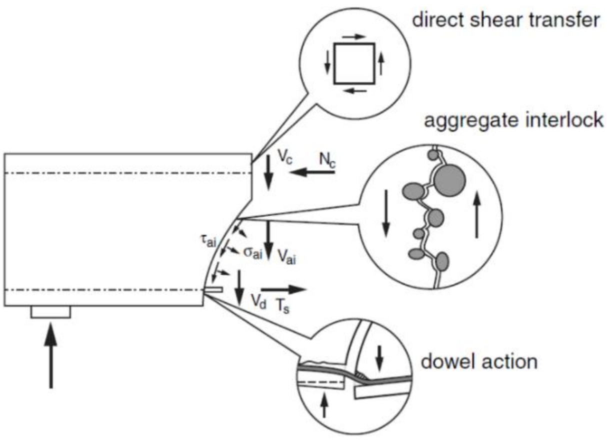

Figure 2.2: Contributing shear capacity mechanisms (Yang, Walraven, & Uijl, 2017)

2.2.1 Shear capacity due to concrete compressive zone

The compression zone in a concrete cross-section contributes to the shear capacity of a concrete element. As can be seen in Figure 2.2.1.1d, the shear stress is parabolically distributed over the cross-section's height in compression with a maximum value around the neutral axis (Arslan, 2011). This load can be resisted due to the intact structure of the concrete under compression. The height of the concrete compression zone is therefore partly determining the shear capacity but is also dependent on the longitudinal reinforcement, since the properties of the reinforcement determine the height of the neutral axis.

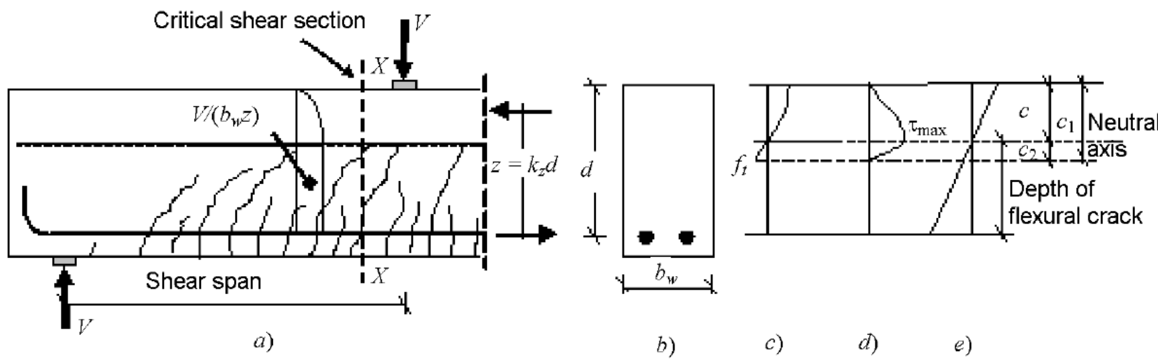

Figure 2.2.1.1: Shear stress and strain distribution in a RC beam with flexural cracks: a) typical crack pattern and shear stress distribution (adapted from Cladera (2003)); b) cross-section X-X; c) distribution of concrete stresses (Khuntia, Stojadinovic 2001); d) shear stress distribution (Khuntia, Stojadinovic 2001); e) longitudinal strain distribution (Arslan, 2011)

For a structural element subjected to bending, the amount of reinforcement depends on the stiffness and strength of the composite material. For FRP, the strength-to-stiffness ratio is significantly higher than that of steel, which has a substantial impact on the distribution of stresses across the cross-section. In a balanced situation, which is typically desirable in reinforced concrete design, the neutral axis depth for an equivalent FRP RC section is relatively small (Pilakoutas K. , 2022). This is illustrated in Figure 2.2.1.2:

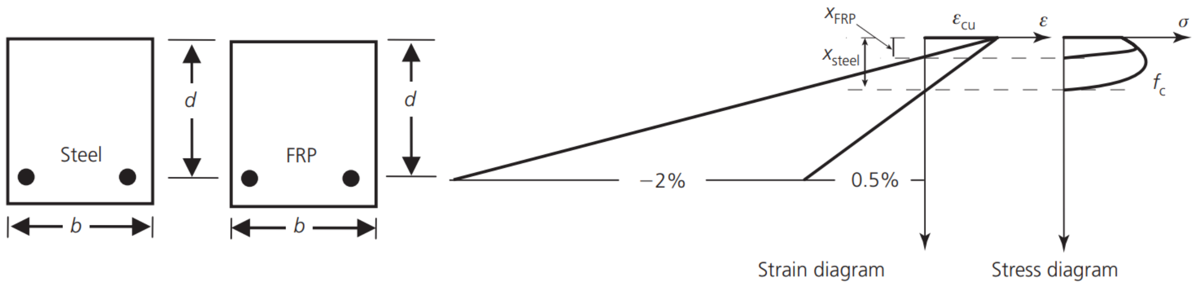

Figure 2.2.1.2: Strain distribution for FRP vs steel rebar (Pilakoutas, Guadagnini, Neocleous, & Matthys, 2009)

If the tensile force in the rebar that has be resisted is the same in both cases and the amount of reinforcement is also the same, the reinforcement in the FRP variant will need to strain approximately four times more. This is because the E-modulus of FRP is four times lower than that of steel. Consequently, a larger portion of the cross-section will be under tension, resulting in a smaller concrete compression zone. This reduction in the concrete compression zone means that the shear capacity derived from the concrete compression zone for this cross-section also decreases.

In case of steel reinforced concrete structures, the shear capacity of the concrete compression zone decreases strongly after yielding of the steel. This is a somewhat different mechanism than when BFRP is used. As soon as cracking occurs in BFRP reinforced structures, the area under compression is smaller than when steel is used. If the strain in the BFRP reinforcement increases, the decrease in the concrete compression zone does not decrease further as is the case with steel reinforcement (fib bulletin 40, 2007). Even though a lower shear resistance is assumed after cracking, it will decrease less quickly than in the case of steel. See Figure 2.2.1.3.

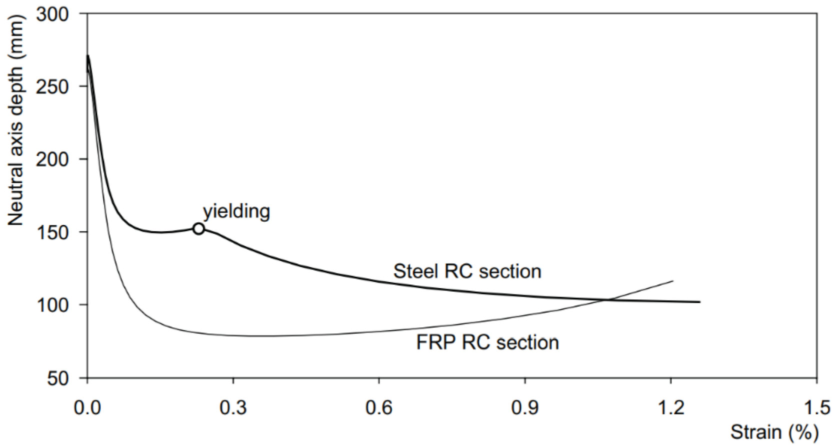

Figure 2.2.1.3: Behaviour of steel and FRP RC sections with same geometry and amount of longitudinal reinforcement (fib bulletin 40, 2007)

To understand the phenomenon of different behavior in the neutral axis depth, a closer examination of the strain and stress distributions in concrete sections reinforced with steel and FRP is required. First, the steel-reinforced variant will be analyzed.

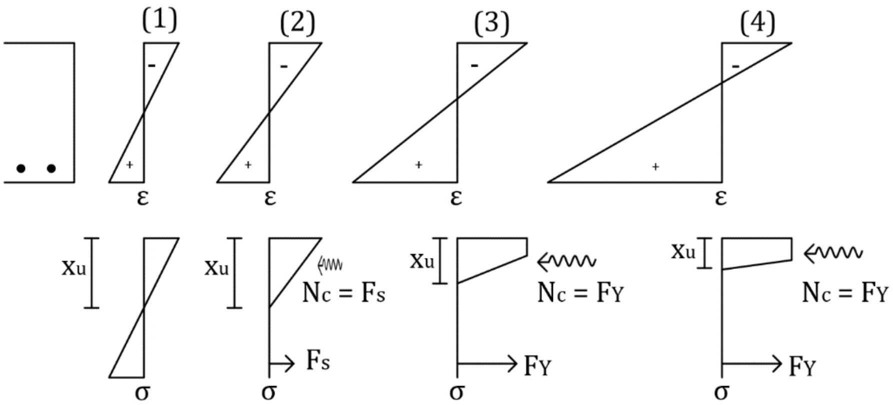

Figure 2.2.1.4: Stress strain distribution steel RC

Since steel does not behave linearly elastic anymore beyond the yield point, the force does not increase with strain from this point onwards. In other words, Hooke’s law no longer applies and a horizontal yielding plateau is reached. As observed in the transition from loading stage (3) to loading stage (4), the strain in the tensile zone of the section increases, but the force in the steel reinforcement remains constant due to yielding. However, equilibrium of horizontal forces must still be maintained in the section, meaning $F_Y = N_C$ must be satisfied. This can only occur if the compression zone x_u decreases with increasing strain.
For FRP RC a different situation holds.

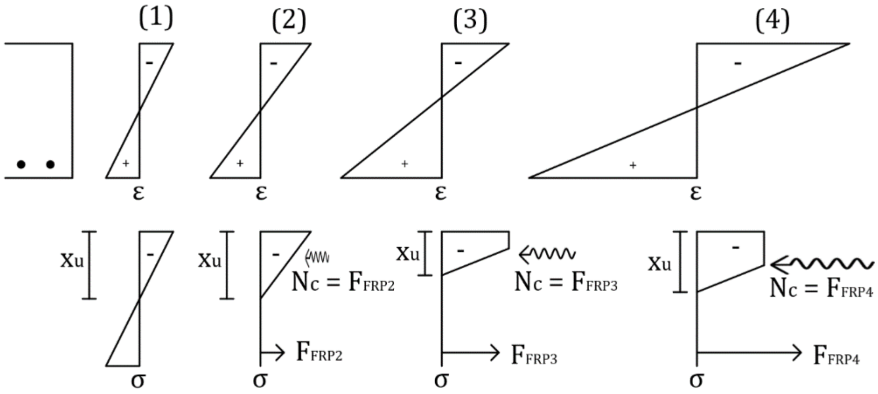

Figure 2.2.1.5: Stress strain distribution FRP RC

In contrast to steel, FRP behaves in a fully linear elastic manner, meaning Hooke's law always applies to the reinforcement. When the strains increase from loading stage (3) to (4), the force in the reinforcement also increases, as evidenced by the larger force vector in the later loading stages. To achieve horizontal equilibrium in this case, the concrete compression zone must increase to allow the force in the concrete, N_C, to increase as well. This differs from the steel-reinforced variant, where after yielding, the forces in the steel and thus in the compression zone remain constant despite increasing strains.

2.2.2 Shear capacity due to aggregate interlock

In the tensile zone of the concrete section, shear transfer across a crack occurs by mechanical interlock when there is a shear displacement parallel to the direction of the crack. Several studies have investigated the effect of aggregate interlock on the shear capacity. These studies have shown that for beams without web reinforcement, the contribution of aggregate interlock to the shear capacity ranges between 33% and 50% (Taylor, 1970). For increasing crack widths, this percentage decreases because the aggregate interlock diminishes (Walraven, 1981).

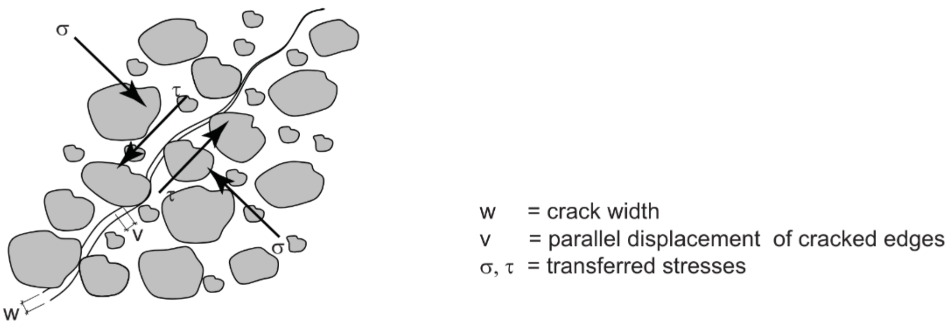

Figure 2.2.2.1: Transfer of forces across cracks due to aggregate interlock (fib bulletin 40, 2007)

When FRP rebar is used, larger deflections and crack widths will occur compared to when steel rebar is used. This is primarily due to the lower modulus of elasticity of FRP. Consequently, the use of FRP results in a decrease in shear capacity due to the reduction in aggregate interlock.

2.2.3 Shear capacity due to dowel action

The concept of dowel action refers to the combination of the tensile resistance of the surrounding concrete around the longitudinal reinforcement and the bending and transverse shear resistance of the rebars. For traditionally lightly steel-reinforced elements, the shear capacity derived from dowel action is of relatively minor importance compared to other shear transfer mechanisms (Kostovos & Pavlovic, 1999).

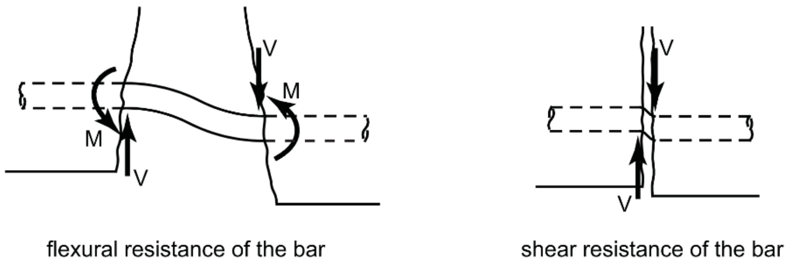

Figure 2.2.3.1: Mechanisms of dowel action for flexural bars crossing a crack (fib bulletin 40, 2007)

Research by Baumann and Rüsch (1970) indicates that the shear resistance provided by dowel action is governed by the tensile strength of the concrete cover and the diameter of the reinforcing bar. The concrete cover will fail by splitting when the dowel action force becomes too high. However, it is important to note that Baumann and Rüsch's theory is based on steel reinforcement bars. The strength of steel is significantly higher than that of concrete, making concrete failure the governing factor. In contrast, the strength of FRP rebar perpendicular to the bar direction is much weaker, which means that failure of the concrete cover may not be the governing factor, but rather the failure of the FRP rebar itself.

Research conducted by Lu, Yang, & Hendriks (2024) demonstrates that the ratio of beam length, L, to rebar diameter, ϕ, also influences dowel action. After analyzing various dowel action models, they state that, in most cases, dowel splitting in a normally reinforced beam occurs when L/ϕ is greater than 5. Additionally, Lu, Yang, & Hendriks (2024) suggest in their comparative study that most models give a relatively conservative value for dowel action capacity when considering the splitting tensile strength. In their own dowel action model, they provide a correction factor for this phenomenon.

To determine the dowel action of BFRP, the shear properties of a BFRP rebar must first be examined. These properties depend on both the fibres and the resin.

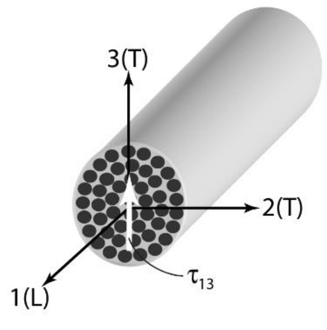

Figure 2.2.3.2: BFRP bar subjected to transverse shear (fib bulletin 40, 2007)

For the interlaminar shear modulus, G_{13}, a semi-empirical formula developed by Tsai and Hahn (1980) is used. The input parameters include the volume fractions of the fibre and resin matrix, V_f en v_m and their respective shear moduli, G_f en G_m.

$$G_{13} = G_m \frac{V_f+\eta_{13}+(1-V_f)}{\eta_{13}(1-V_f)+V_f G_m/G_f} \tag{2.2.3.1}$$

where,

$$\eta_{13} = \frac{3-4v_m+G_m/G_f}{4(1-V_m)} \tag{2.2.3.2}$$

Transverse shear usually results in matrix splitting without shearing off any fibres. Therefore, the interlaminar shear strength is dominated by the strength of the resin matrix, as the shear force acts on a plane perpendicular to the fibre direction. The shear resistance of FRP can be enhanced by winding or braiding the fibres transversely to the main reinforcing fibres.

The shear properties of a BFRP rebar are determined by the properties of the resin. When BFRP is used as longitudinal reinforcement, the shear resistance derived from dowel action can be considered negligible, primarily because the transverse stiffness of the rebars is extremely low (Kanakubo & Shindo, 1997) (Tottori & Wakui, 1993).

2.2.4 Design variables affecting shear capacity

Nex to the main shear mechanisms described above, one could influence the shear capacity by adjusting the following parameters:

Longitudinal reinforcement ratio
A higher longitudinal reinforcement ratio will give an increase in shear capacity. A higher reinforcement ratio will result in smaller crack widths, which will increase the previously mentioned contributions of shear mechanisms.

Shear reinforcement
Shear reinforcement will enhance the confinement of the concrete and reduce crack widths, which will also have a positive effect on the contributing shear mechanisms.

Axial loading/prestress
Axial loading and prestress will enhance the confinement of the concrete and make sure that tension will occur at a later loading step, which will also have a positive effect on the contributing shear mechanisms.

Dimensions structural element
An increased height and/or width of the cross section will distribute the loading over a bigger surface/volume wat will increase its shear capacity as well. Note that this increase in capacity is not proportional to the increase in dimensions.

Concrete strength
Increasing concrete strength has a positive effect on the aforementioned contributing shear mechanisms. The upper limit of this increase is a concrete strength of 60 MPa. This value is maintained because, at strengths above this level, cracks can propagate through the aggregates. Consequently, aggregate interlock may decrease due to the reduced crack surface roughness. Due to this phenomenon, most design formulas for shear are only applicable up to a concrete strength of ± 60 MPa.

Shear span/depth
Concrete structural elements with a low a/d ratio can withstand higher shear forces than elements with a high a/d ratio. This is because the load in a low a/d ratio is placed relatively closer to the support. As a result, arch action occurs, and the load is transferred more as a compressive force towards the support rather than a true shear force.

2.2.5 One-way shear failure modes

The previously mentioned variables all affect the way in which the structural element fails. The corresponding one-way shear failure modes are presented below."

Flexural shear failure
Flexural shear failure is a shear failure mechanism, initiated by flexural cracks from which an inclined shear crack develops into the compression zone.
Consider the region between the support and the point load in the figure below. This section does not fail in bending, as it is assumed that the reinforcement is the same along the entire length. Consequently, the flexural reinforcement in this area near the support is over-dimensioned ($M_{Ed} < M_{Rd}$). Instead of cracks perpendicular to the tensile reinforcement as in the case of pure bending, inclined cracks will develop in the shear zone near the support. If the load is further increased, these inclined cracks will progressively reduce the concrete compression zone, eventually leading to the failure of the beam. This phenomenon is referred to as flexural shear failure.

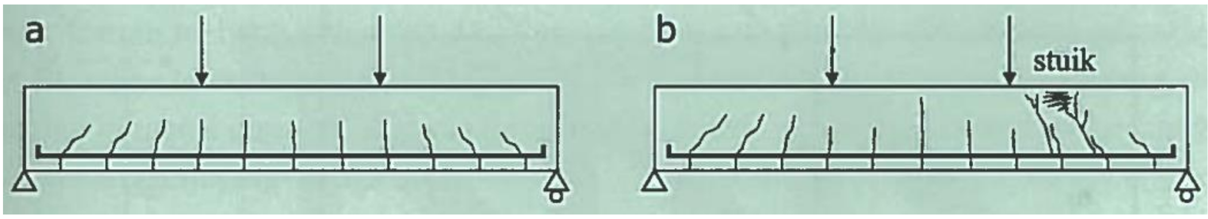

Figure 2.2.5.1: Flexural shear failure crack pattern a) serviceability limit state, b) ultimate limit state (Braam & Langendijk, 2008)

Shear tension failure

Shear tension failure is a shear failure mechanism in the uncracked region, initiated by the principal tensile stress exceeding the concrete strength.
In the part of the beam where no flexural tensile cracks occur, the uncracked concrete section, inclined cracks can develop under a certain load. These cracks, forming an angle of approximately 30° to 45° with the beam axis, suddenly (brittle) appear in the concrete, unlike flexural shear failure, where cracks propagate from the bottom of the beam. If there is insufficient reinforcement in the section, a continuous inclined crack will form in the beam, leading to sudden failure without warning. This phenomenon is referred to as shear tension failure.

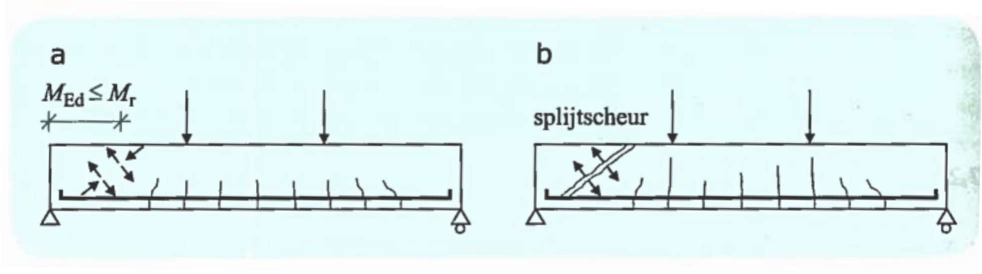

Figure 2.2.5.2: Shear tension failure crack pattern a) serviceability limit state, b) ultimate limit state (Braam & Langendijk, 2008)

2.3 FRP design codes and guidelines

2.3.1 Maximum allowable crack widths

Design standards and guidelines permit larger crack widths when using BFRP compared to steel rebar, primarily because BFRP does not corrode. The maximum allowable crack widths are based on aesthetics and other considerations, such as preventing water leakage. Different allowable crack widths may apply depending on that specific situation. These variations depend on factors such as exposure class, loading type, and the function of the structure. Table 2.3.1.1 presents the maximum allowable crack widths according to various design standards and guidelines. For reinforced concrete with steel, the range of the maximum allowable crack width is 0,2 mm to 0,4 mm.

Table 2.3.1.1: Maximum allowable crack widths (ACI 440.1R-15, 2015) (ACI 440.11-22, 2022) (BRL 0513, 2015) (CSA S806-12, 2012) (FprEN_1992-1-1:2022, 2022)

Code or Guideline	Maximum allowable crack width FRP reinforced concrete
ACI 440.1R-15	0,5 mm – 0,7 mm
ACI 440.11-22	0,5 mm – 0,7 mm
BRL 0513	0,5 mm
CSA S806:12	0,7 mm
Eurocode 2 Annex R	0,4 mm - 0,7 mm

2.3.2 One-way shear design codes and guidelines

This paragraph will address various design codes that can be utilized in determining the shear capacity of a concrete element. Eurocode 2 does not provide calculation rules for the shear capacity of FRP reinforced concrete. Some guidelines that do include FRP calculation rules are presented in the fib Model Code Bulletin 40 such as the ACI Commission 440. There are numerous other national guidelines available, but for this study, only these two will be examined. For comparison with steel reinforcement, the guidelines from Eurocode 2 will be utilized.

Shear design issues with BFRP, compared to steel:

1) Low modulus of elasticity
2) Low transverse shear resistance
3) High tensile strength and no yield point
4) After cracking, smaller depth to neutral axis, due to lower axial stiffness (product of reinforcement area and modulus of elasticity)
5) Lower compression region
6) Crack width

As a result of these issues the shear resistance provided by compressed concrete, aggregate interlock and dowel action is smaller.

ACI 440.1R-15 guide for shear capacity reinforced concrete with FRP
Committee 440 of the American Concrete Institute revised the preexisting code applicable to steel RC structures (ACI (2005), incorporating adjustments rooted in a strain-based approach. This adaptation became necessary due to the inherent limitation in directly altering the reinforcement area within the simple shear equation (cf. ACI 318-05 Eq. 11-3)

The shear design equation for FRP RC beams without stirrups in ACI 440.1R-15 is formulated based on the framework developed by *Tureyen and Frosch (2002, 2003)*, marking a notable departure from previous methodologies for computing the concrete shear contribution. In accordance with this model, the longitudinal FRP reinforcement's axial stiffness is accounted for through the compression depth of the concrete, denoted as "c". Subsequently, the concrete shear resistance, V_{cf} , of flexural members featuring FRP reinforcement, is determined using these equations:

$$V_c = 0{,}4\sqrt{f_c'}\,b_w(kd) \qquad (2.3.2.1)$$

For singly reinforced rectangular sections, and assuming elastic-cracked conditions

where

$$k = \sqrt{2\rho_f n_f + \left(\rho_f n_f\right)^2} - \rho_f n_f \qquad (2.3.2.2)$$

and

$$\rho_f = \frac{A_f}{b_w d} \qquad (2.3.2.3)$$

$$n_f = \frac{E_f}{E_c} \qquad (2.3.2.4)$$

Eq.(2.3.2.1) can also be re-written as

$$V_c = \left(\frac{12}{5}k\right)0{,}167\sqrt{f_c'}\,b_w c \qquad (2.3.2.5)$$

So in fact the ACI 318 equation for concrete shear resistance of steel reinforced concrete, is simply modified by the factor(12/5k) which accounts for the axial stiffness of the FRP Reinforcement.

The effect of the flexural reinforcement ratio on the concrete shear strength can be seen in Figure 2.3.2.1.

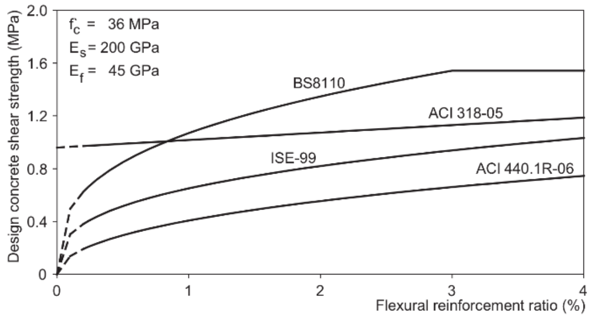

Figure 2.3.2.1: Effect of flexural reinforcement ratio on concrete shear strength according to different guidelines (fib bulletin 40, 2007)

Next to this also the effect of the concrete compressive strength, on the shear capacity of the concrete can be visualised in a graph:

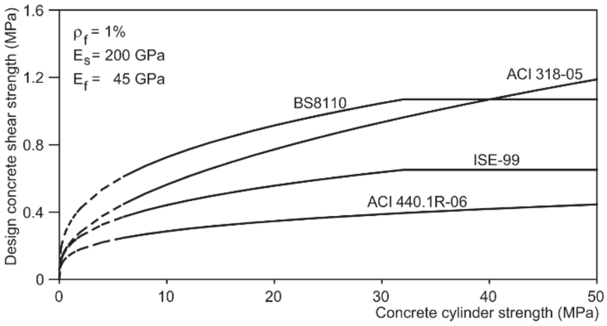

Figure 2.3.2.2: Effect of concrete strength on shear capacity, according to different guidelines (fib bulletin 40, 2007)

The contribution of longitudinal FRP reinforcement in terms of dowel action is not considered in the ACI 440.1R-15 shear design model.

ACI 440.11-22 Code for shear capacity reinforced concrete with GFRP

In contrast to ACI 440.1R-15, ACI 440.11-22 is not a guide but a building code requirement. This code specifies the minimum requirements for structural concrete reinforced with GFRP. Since GFRP, like BFRP, belongs to the family of FRP and has very similar properties to BFRP, it is reasonable to apply this code to BFRP as well. This code also imposes a lower limit for shear force design, as recommended by Nanni et al.(2014) The lower limit is proposed to avoid unreasonably low shear force capacities for lightly reinforced members such as slabs and foundations.

$$V_c = 0{,}4\sqrt{f_c'}\lambda_s b_w k d \qquad (2.3.2.6)$$

where

$$V_{c\,min} = 0{,}067\sqrt{f_c'} b_w d \qquad (2.3.2.7)$$

$$\lambda_s = \sqrt{\frac{2}{1+0{,}004d}} \leq 1{,}0 \qquad (2.3.2.8)$$

The contribution of longitudinal FRP reinforcement in terms of dowel action is not been taken into account in the ACI 440.11-22 shear design model.

BRL 0513

The Dutch calculation model for GFRP rebars is BRL0513. In terms of shear capacity, BRL0513 provides only a correction factor for the reinforcement ratio for structural elements without shear reinforcement. In this way, the existing formulas from Eurocode 2 6.2.a are adjusted to account for the lower modulus of elasticity of GFRP (BRL 0513, 2015).

$$\rho_l = \frac{E_{gl} * A_{gl}}{E_s * b * d} \leq 0{,}02 \quad (2.3.2.9)$$

Shear capacity according to Eurocode 2, for cross sections without shear reinforcement:

$$V_{Rd,c} = [C_{Rd,c}\mathrm{k}(100\rho_l f_{ck})^{1/3} + k_1\sigma_{cp}]b_w\mathrm{d} \ \geq \ (v_{min} + k_1\sigma_{cp})b_w\mathrm{d} \quad (2.3.2.10)$$

where

$$k = 1 + \sqrt{\frac{200}{d}} \leq 2{,}0 \quad (2.3.2.11)$$

$$\sigma_{cp} = \frac{N_{Ed}}{A_c} \leq 0{,}02 f_{cd} \quad (2.3.2.12)$$

$$v_{min} = 0{,}035 k^{3/2} f_{ck}^{1/2} \quad (2.3.2.13)$$

The values of $C_{Rd,c}$, and k_1 for use in a country can be found in the national annex. The recommended value for $C_{Rd,c}$ is $0{,}18/\gamma_c$ and for k_1 it is 0,15.

CSA S806:12 shear capacity

In addition to the American ACI standards and guides, the Canadian CSA standard is also available for designing with FRP in concrete structures. The CSA S806:12 standard, published by the Canadian Standards Association (CSA), provides methodologies for calculating the reduction in shear capacity of a concrete section. Like ACI 440, this is achieved by modifying existing formulas that apply to steel reinforced concrete. The CSA S806:12 standard distinguishes between elements with an effective depth of 300 mm or less and those with an effective depth greater than 300 mm. Additionally, different formulas apply depending on the presence or absence of transverse reinforcement.

For d ≤ 300 mm or amount of transverse reinforcement at least equal to minimum required

$$V_c = 0{,}05 k_m k_r (f_c')^{\frac{1}{3}}\, b_w d_v \quad (2.3.2.14)$$

where

$$0{,}11\sqrt{f_c'}\,b_w d_v \leq \ V_c \leq \ 0{,}22\sqrt{f_c'}\,b_w d_v \quad (2.3.2.15)$$

$$f_c' \leq 60\ \mathrm{N/m}m^2 \quad (2.3.2.15)$$

$$d_v = 0{,}9\mathrm{d} \tag{2.3.2.16}$$

$$k_m = \sqrt{\frac{V_F d}{M_F}} \leq 1{,}0 \tag{2.3.2.17}$$

$$k_r = 1 + \left(E_f \rho_f\right)^{\frac{1}{3}} \tag{2.3.2.18}$$

Shear modification due to arch effect:
For sections located within a distance of 2,5d from the face of a support. Where the support reaction causes compression in the beam parallel to the direction of the shear force at the section, an extra factor k_d has to be taken into account.

$$k_d = \frac{2{,}5}{\frac{M_F}{V_F d}} \tag{2.3.2.19}$$

$$1{,}0 \leq k_d \leq 2{,}5 \tag{2.3.2.20}$$

For d > 300 mm or amount of transverse reinforcement less than minimum required, an extra factor k_s has to be taken into account

$$k_s = \frac{750}{450+d} \leq 1{,}0 \tag{2.3.2.21}$$

ACI 440.1R-15	CSA S806-12	Nehdi et al. (2007)
$V_c = 0.4\sqrt{f_c'}\,b_w(kd)$	$V_c = 0.05 k_m k_r (f_c')^{\frac{1}{3}} b_w d_v$	$for\ \frac{a}{d} \geq 2.5$
$k = \sqrt{2\rho_f n_f + (\rho_f n_f)^2} - \rho_f n_f,$	$0.11\sqrt{f_c'}\,b_w d_v \leq V_c \leq 0.22\sqrt{f_c'}\,b_w d_v$	$V_c = 2.1\left[fc' .\ \rho_f\ \frac{E_f}{E_s}\ \frac{d}{a}\right]^{0.3} b.d$
$n_f = \frac{E_f}{E_c},\ E_c = 4700\sqrt{f_c'}$	$d_v = 0.9d,\ k_m = \sqrt{\frac{V_F d}{M_F}} \leq 1.0,$	$for\ \frac{a}{d} < 2.5$
$V_f = \frac{A_{fv}}{s} f_{fv} d$	$k_r = 1 + (E_f \rho_f)^{\frac{1}{3}},\ k_s = \frac{750}{450+d} \leq 1.0$	$V_c = 2.1\left[fc' .\ \rho_f\ \frac{E_f}{E_s}\ \frac{d}{a}\right]^{0.3} \frac{2.5\,d}{a}\ b.d$
$f_{fv} = 0.004 E_{fv} \leq f_{fb}$	$V_f = \frac{A_{fv}}{s} f_{fv} d_v \cot(\theta)$	$V_f = 0.5\sqrt{\rho_{fv} .\ f_{fv}}\ b.d$
$V_{SC,ACI} = \frac{2}{3}\sqrt{f_c'}\,b_w d$	$f_{fv} = \min(0.4 f_{fu,v},\ 0.005 E_{fv},\ 1200)$	$V_{total} = V_c + V_f$
$V_{total} = V_c + (V_f \leq V_{SC,ACI})$	$V_{SC,CSA} = 0.22 f_c' b_w d_v$	
$A_{fv,min} = \frac{0.35}{f_{fv}} b_w s$	$V_{total} = (V_c + V_f) \leq V_{SC,CSA}$	
	$A_{fv,min} = \frac{0.07\sqrt{f_c'}}{f_{fv}} b_w s$	

Figure 2.3.2.3: Shear capacity overview by (Ebid & Deifalla, 2021)

Forthcoming Eurocode 2
In the forthcoming Eurocode 2, an informative Annex R is included, which provides design principles for FRP in concrete structures. It is important to emphasize that this annex does not contain design formulas, but solely design principles. Additionally, this annex focuses exclusively on GFRP and CFRP, and does not address BFRP.

Table R.1 (NDP) — Partial factors for FRP reinforcement

Design Situation	γ_{FRP}
Persistent and transient design situation	1,50
Accidental design situation	1,10
Serviceability limit state	1,00

Figure 2.3.2.4: Partial factors Annex R Eurocode 2 (FprEN_1992-1-1:2022, 2022)

Over the years, the properties of FRP degrade. The Eurocode accounts for this through the following design principle, where $f_{ftk,100a}$ represents the design long-term strength.

$$f_{ftd} = \frac{f_{ftk,100a}}{\gamma_{FRP}} \tag{2.3.2.22}$$

With

$$f_{ftk,100a} = C_t * C_C * C_e * f_{ftk0} \tag{2.3.2.23}$$

- C_t = 1,0 for indoor and underground environments
- C_t = 0,8 for outdoor members if heating through solar radiation cannot be excluded
- C_C factor determined according to ISO 10406-1, often for GFRP 0,35 and for CFRP 0,8
- C_e factor determined according to ISO 10406-1, often 0,7

For concrete elements only reinforced with longitudinal FRP, that do not require shear reinforcement, the minimum shear resistance, according to 8.2.1(4) in (FprEN_1992-1-1:2022, 2022), may be calculated as:

$$\tau_{Rdc,min} = \frac{11}{\gamma_v} \sqrt{\frac{f_{ck}}{f_{ftk0}} * \frac{E_{fR}}{E_s} * \frac{d_{dg}}{d}} \tag{2.3.2.24}$$

2.3.3 Punching shear design codes and guidelines

In addition to the principle of one-way shear, an inventory is also made of the design standards and guidelines regarding two-way shear, also known as punching shear. Punching shear capacity considers the load of a point load on a slab. Failure occurs when the shear forces around the concentrated load exceed the shear resistance of the slab, causing the load to “punch” through. In the application of this research on cast-in-situ bridge decks on prefabricated inverted T-beams, the point load originates from the wheel loads of vehicles going over the bridge. Below punching shear design formulas from various standards and guidelines can be found.

ACI 440.1R-15 punching shear capacity of reinforced concrete with FRP

The punching shear formula according to ACI 440.1R-15 includes only minor adjustments to the one-way shear capacity formula from Section 2.3.2. Specifically, the factor 0,4 is doubled to 0,8, and the effective width, b_w, is replaced by the perimeter around the loading surface at a distance of d/2, now referred to as b_o.

$$V_c = 0{,}8\sqrt{f_c'}\,b_o(kd) \tag{2.3.3.1}$$

where

$$k = \sqrt{2\rho_f n_f + \left(\rho_f n_f\right)^2} - \rho_f n_f \tag{2.3.3.2}$$

and

$$\rho_f = \frac{A_f}{b_w d} \tag{2.3.3.3}$$

$$n_f = \frac{E_f}{E_c} \tag{2.3.3.4}$$

$$b_o = perimeter\ \ at\ distance\ \frac{d}{2}\ outside\ loading\ surface \tag{2.3.3.5}$$

ACI 440.11-22 punching shear capacity reinforced concrete with GFRP

Like the one-way shear variant of ACI 440.11-22, the formula for punching shear also has a lower limit. Additionally, just like in the formula from ACI 440.1R-15, the factors at the beginning of the formulas are doubled. For this formula as well, b_o refers to the perimeter at a distance of d/2 outside the loading surface.

$$V_c = 0{,}8\sqrt{f_c'}\,\lambda_s b_o kd \tag{2.3.3.6}$$

where

$$V_{c\,min} = 0{,}132\sqrt{f_c'}\,b_o d \tag{2.3.3.7}$$

$$\lambda_s = \sqrt{\frac{2}{1+0{,}004d}} \leq 1{,}0 \tag{2.3.3.8}$$

BRL 0513 punching shear capacity reinforced concrete with GFRP

The BRL 0513 guideline includes a minor adjustment to the punching shear formula in terms of reinforcement ratio. Specifically, the square root of the product of the reinforcement in the x and y directions is taken. Additionally, unlike the American ACI codes, a distance of 2d outside the loading surface is used to determine the perimeter, rather than d/2.

$$\rho_{l,x,y} = \frac{E_{gl}}{E_s}\sqrt{\rho_{l,x} * \rho_{l,y}} \leq 0{,}02 \tag{2.3.3.9}$$

$$V_{Rd,c} = C_{Rd,c}\mathrm{k}\left(100\rho_{l,x,y}f_{ck}\right)^{1/3} * b_o * \mathrm{d}\ \geq\ V_{min} \tag{2.3.3.10}$$

where

$$k = 1 + \sqrt{\frac{200}{d}} \leq 2{,}0 \tag{2.3.3.11}$$

$$V_{min} = 0{,}035k^{3/2}f_{ck}^{1/2} * b_o * d \tag{2.3.3.12}$$

$$b_o = perimeter\ \ at\ distance\ 2d\ outside\ loading\ surface \tag{2.3.3.13}$$

The value of $C_{Rd,c}$ for use in a country can be found in the national annex. The recommended value for $C_{Rd,c}$ is 0,18/γ_C.

CSA S806:12 punching shear capacity
The formula for punching shear according to this Canadian standard offers three possibilities. The design value of the punching shear capacity can be obtained by taking the minimum value of the three formulas listed below.

$$V_C = \left(1 + \frac{2}{\beta_c}\right) 0{,}028\lambda\varphi_c(E_F \rho f_c')^{\frac{1}{3}} * b_o * \mathrm{d} \tag{2.3.3.14}$$

$$V_C = [\left(\frac{\alpha_s d}{b_o}\right) + 0{,}19]0{,}147\lambda\varphi_c(E_F \rho f_c')^{\frac{1}{3}} * b_o * \mathrm{d} \tag{2.3.3.15}$$

$$V_C = 0{,}056\lambda\varphi_c(E_F \rho f_c')^{\frac{1}{3}} * b_o * \mathrm{d} \tag{2.3.3.16}$$

where

$$\beta_c = \frac{long\ loading\ side}{short\ loading\ side} \tag{2.3.3.17}$$

$$\lambda = 1\ for\ normal\ weight\ concrete\ or\ 0{,}85\ for\ semi - lightweight\ concrete \tag{2.3.3.18}$$

$$\alpha_s = 4\ for\ interior, 3\ for\ edge\ and\ 2\ for\ corner \tag{2.3.3.19}$$

$$b_o = perimeter\ at\ \frac{d}{2} \tag{2.3.3.20}$$

2.3.4 Concrete cover design codes and guidelines

Concrete cover according to ACI 440.1R-15 guide
Since ACI 440.1R-15 serves as a guideline rather than a standard, it does not specify explicit minimum cover values. Instead, it primarily explains design principles and qualitatively describes the impact of concrete cover on the mechanical and durability properties of FRP-reinforced concrete structures. For instance, it is recommended that a ratio of concrete cover thickness to bar diameter $c/d_b > 1{,}6$ is sufficient to avoid cracking of concrete under high temperature up to 80°C.

Concrete cover according to ACI 440.11-22 Code

According to ACI 440.11-22, Section 20.5.1, the cover requirement is solely dependent on constructability, bond, and fire-related performance issues. Durability does not play a role in this standard. The standard specifies that a cover of, $c \geq 2Ø$ is necessary to control cracking due to thermal cycling loading in smaller diameter bars. Unlike steel bars, if GFRP bars are not adequately anchored, high temperatures during a fire can cause a loss of bond. Table 20.5.1.3.1 from ACI 440.11-22, shown below, presents the minimum cover requirements for different structural element types in relation to fire. These minimum cover requirements are significantly higher than those in other standards and guidelines, because ACI 440.11-22 is specifically focused on GFRP. However, the fire resistance of basalt fibres is significantly better than that of glass fibres. The operating temperature limit of basalt fibre is 650°C, compared to 460°C for glass fibre (Bhat, Chevali, Liu, Feih, & Mouritz, 2015).

Table 2.3.4.1: Specified concrete cover for cast-in-place and precast concrete members (ACI 440.11-22, 2022)

Concrete exposure	Member	GFRP reinforcement	Specified cover
Cast against and permanently in contact with ground	All	All	75 mm
Exposed to weather	All	No. 6 through No. 10 bars	50 mm
		No. 5 bar and smaller	12 mm – 25 mm
Not exposed to weather or cast against the ground	Slab, joists, and walls	All	19 mm
	Beams, columns, pedestals, and tension ties	All	12 mm – 25 mm

Concrete cover to according to BRL 0513

This amendment sheet aligns with the provisions outlined in Annex R of the upcoming Eurocode. The durability requirement concerning corrosion applicable to steel reinforcement is not relevant for FRP. The minimum cover for FRP in normal-weight concrete, considering the construction class, is specified by $c_{min,dur}$ (Table 4.4N). For this, the environmental exposure class X0 should be adhered to.

Concrete cover according CSA806:12

According to Section *8.2.3 Minimum cover*, the minimum clear concrete cover in reinforced concrete members shall be $2d_b$ or 30 mm, whichever is greater.

Concrete cover according to forthcoming Eurocode 2

In the forthcoming Eurocode 2, it is anticipated that the requirement for minimum concrete cover $c_{min,dur}$ may be omitted when using FRP rebar in concrete structures. Consequently, this modification would render exposure classes inconsequential in determining the necessary concrete cover

$$c_{nom} = c_{min} + \Delta c_{dev} \tag{2.3.4.1}$$

where

$$c_{min} = \max\{c_{min,b};\ c_{min,dur} + \Delta c_{dur,\gamma} - \Delta c_{dur,st} - \Delta c_{dur,add}; 10mm\} \tag{2.3.4.2}$$

The predominant component of the above equation is likely to be $c_{min,b}$, the bond component. For the forthcoming Eurocode 2, this value will depend on the rebar diameter. There exists a lower limit of $c_{min,b} \geq 10$ mm, $c_{min,b} \geq 2Ø$, or $c_{min,b} \geq 1{,}5Ø$ in cases where tests permit. Additionally, when the aggregate size exceeds 32mm, an additional 5mm of concrete cover for adhesion must be applied (NEN-EN 1992-1-1 4.4.1.2 (3)).

Δc_{dev} is applied as an addition to c_{min} to allow the design for deviation. The value of Δc_{dev} for each country may be found in their National Annex. The recommended value is 10 mm. In the Dutch annex, 5 mm is maintained (NEN-EN 1992-1-1 4.4.1.3 (1) & NB). In certain situations, the acceptable deviation and consequently the tolerance may be reduced. If it can be guaranteed that a highly accurate measuring instrument is used for monitoring concrete cover and that elements that do not comply are removed (for example, prefabricated elements), then the design deviation, Δc_{dev}, may be reduced to 0 mm.

2.4 Overview of existing experimental results on BFRP

In addition to the design codes and guidelines, an overview of existing test results on the capacities of reinforced concrete with BFRP rebar is provided. Table 2.4 gives a concise summary of several studies, along with their conclusions and recommendations.

Table 2.4: Overview results from existing shear experiments

Research by	Research description	Conclusions
(Guadagnini, Pilakoutas, & Waldron, 2006)	-Beams with no shear reinforcement -Only longitudinal reinforcement -Steel vs FRP rebar -Different shear span/depth ratios	-Steel RC exhibit higher shear resistance than FRP RC, for beams with equivalent geometrical area of reinforcement. -ACI shear formulas appear to be very conservative. -Similar shear failure modes for steel and FRP RC. Justifying the extension of the design principles adopted for steel RC to FRP RC.
(Abed, Refai, & Abdalla, 2019)	-Experimental, analytical and numerical results of BFRP RC beams -Only longitudinal reinforcement -Steel vs BFRP rebar -Different reinforcement ratios -Different heights	- Beams that showed concrete crushing at the top demonstrated more deformations than those beams that failed due to diagonal shear cracks only. -Shear capacities BFRP RC linearly proportional to the cubic root of effective dept, $\sqrt[3]{d}$, the longitudinal reinforcement ratio, $\sqrt[3]{\rho}$, and the reciprocal of the shear span-todepth ratio, $1/\sqrt[3]{(a/d)}$.
(Abdul-Salam, Farghaly, & Benmokrane, 2016)	-16 FRP reinforced concrete slabs were tested -Different bar diameters -Normal and high strength concrete	-Observed failure mechanisms: shear-compression failure, diagonal tension failure and bond/anchorage failure. -Normal concrete cracks at lower loading than high strength concrete. -High bar diameter increases bond - splitting cracks. -Slab shear strength is proportional to axial stiffness of FRP reinforcement.
(Tharmarajah, Taylor, Cleland, & Robinson, 2014)	-In plane restrained slabs -Full scale dimensions - Steel vs GFRP vs BFRP	-GFRP and BFRP showed same cracking pattern -Failure load much higher than calculated by Eurocode 2 and ACI -CMA significantly increased capacity -The restrained slab had a capacity more than 3 times higher than the simply supported slab

2.5 Summary and research gap

The literature review has demonstrated how BFRP rebar material differs from steel. Firstly, the production process of BFRP was examined, where filaments are pulled from heated basalt rock and then combined with a resin matrix and pultrusion technique to form rebar. As a result, BFRP is approximately three times stronger than steel in the uniaxial direction, although its E-modulus is about four times lower. Another significant difference is that FRP is completely linear elastic until fracture strain, unlike steel, which exhibits yielding.
Additionally, BFRP was compared with other FRP materials, revealing that it has the most similarities with glass FRP. Carbon FRP is much more expensive and has a greater environmental impact, while aramid FRP is more susceptible to certain acids and alkalis and has a lower tensile strength than BFRP.
One of the major advantages of BFRP is that, like other FRPs, it cannot corrode. This enhances the durability of structures and eliminates the need for high concrete cover requirements. Furthermore, various LCA studies have shown that BFRP rebar is more sustainable than traditional steel reinforcement bars.
Regarding design codes and guidelines, it was found that these are still very limited in Europe. Eurocode only includes some amendments and a brief appendix on FRP-reinforced concrete in the forthcoming version. In contrast, the American ACI440 and Canadian CSA S806 standards are much more advanced in terms of calculation methods for FRP-reinforced concrete. The reference projects considered, also show that North American design approaches are often used due to their more comprehensive nature.

Overall, the literature review concludes that BFRP is a promising and more sustainable material than steel reinforcement. BFRP is significantly stronger than steel and can enhance the durability of structures since it does not corrode. This also has the added benefit of potentially allowing for a smaller concrete cover. The main challenge with BFRP applications lies in its lower E-modulus, which may result in larger deformations and cracks. BFRP in reinforced concrete can reduce the contributions of the shear capacity mechanisms: aggregate interlock, dowel action, and concrete compression. Numerous experimental studies have confirmed that the shear capacity is indeed much lower when BFRP reinforcement is used.
Finally, there has been little to no research on the effect of BFRP reinforcement in a bridge deck combined with a smaller concrete cover, highlighting the urgency of this research.

3. Preliminary analysis of bridge deck capacity using various design codes

A preliminary analysis of the bridge deck capacity with various design codes, was conducted to gain an initial understanding of the critical failure mechanism of the concrete bridge deck. This study utilized the simple design formulas from various design codes and guidelines as outlined in Section 2.3. The concrete bridge deck with traditional steel reinforcement was tested according to Eurocode 2 and the traffic load model according to Eurocode 1. For the variant with BFRP reinforcement, the American ACI 440 and the Dutch BRL0513 were considered. For the American ACI 440, the capacity was tested against the load according to AASHTO. For BRL0513, Eurocode 1 also applies as the relevant traffic load. The preliminary analysis was conducted based on a case study as described below.

3.1 Structural geometry and material composition of the bridge deck

The motivation of this preliminary analysis is based on the case study of Figure 3.1. The main reinforcement of the concrete bridge deck is chosen at φ16 – 150 mm. In the preliminary analysis, the load-bearing capacities are plotted against different effective depths, d. The effect of a double amount of reinforcement in the case of reinforcement with BFRP is also examined. In this way, approximately the same ECI score is obtained in the field of reinforcement, since the ECI/volume unit for BFRP is approximately half that of steel (Leenders, 2024).
The selected concrete strength class is C30/37. For steel, B500 reinforcement steel was chosen and for BFRP an ultimate tensile strength of 1200 N/mm^2 with E-modulus of 55 GPa was assumed.

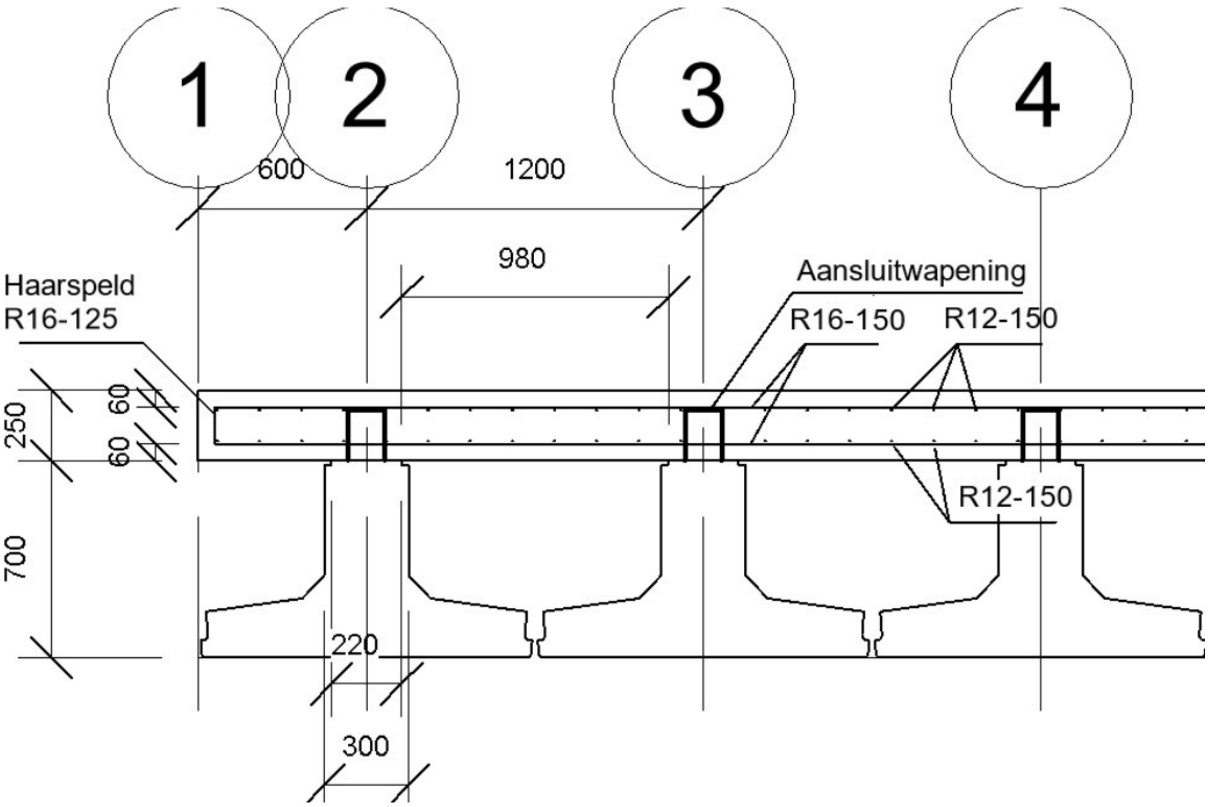

Figure 3.1: Geometry of cast-in-situ concrete bridge deck

3.2 Structural mechanics scheme and applied loads

The bridge deck spans multiple inverted T-beams. This affects the boundary conditions of the mechanical model for a segment of the bridge deck when it is schematized as a span over two supports. The chosen cross-section of the bridge in the longitudinal direction also influences the selected mechanical model. For instance, a cross-section closer to the cross beams will have a more moment-resistant connection between the T-beam and the bridge deck. Conversely, moving towards the middle of the span in the longitudinal direction results in a connection that behaves more like (rotational)spring. Additionally, the thickness of the slab will impact the degree of flexibility of the boundary conditions in the mechanical model.

This preliminary analysis aims to provide an initial impression of the magnitude of the loads and to identify the critical failure mechanism. The mechanical model adopted is a quarter-way between a fully fixed and a simply supported structure. The width of the bridge deck is set to be 1200 mm as this is the distance to the line support over which the point loads are distributed.

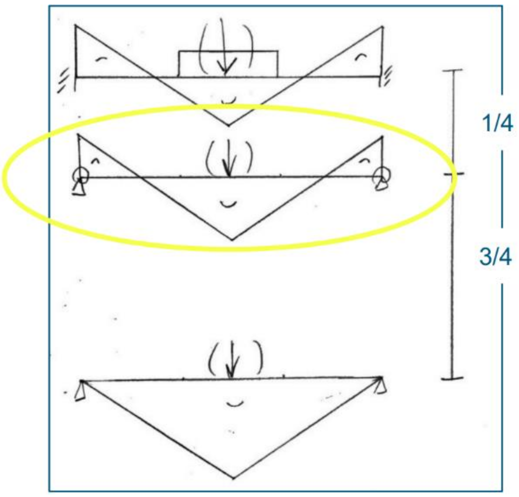

Figure 3.2: Chosen boundary conditions for preliminary analysis

Table 3.2: Traffic Loads, design truck HL-93 (AASHTO, 2012) LM1 (NEN-EN 1991-2+C1, 2015)

Traffic Load	UDL	Wheel Load
NEN-EN 1991+2+C1	10,35 kN/m^2	150 kN
AASHTO	3,1 kN/m^2 (0,64 klf over 3m width, on a 3,6 m wide lane)	71 kN (16 kip)

3.3 One-way shear capacity analysis: comparison of design codes

First, the one-way shear capacity was analysed analytically. For each design code the capacity was calculated as a function of the effective depth. In terms of unity checks, it was found that the BRL0513 provides a much more conservative approach compared to the ACI 440 standard. Additionally, when comparing ACI 440 to traditional reinforcement methods, the steel variant exhibits a higher shear capacity than the BFRP variant at lower reinforcement ratios. As the reinforcement ratio increases, this difference diminishes. For all approaches, an increase in effective depth results in an increase in shear capacity.

However, it should be noted that European and American standards are based on different design philosophies. As shown in the left plot of Figure 3.3, the shear capacity according to the ACI is significantly lower than that of the BRL0513 approach. Furthermore, the ACI 440, according to AASHTO, applies a wheel load of 71 kN, in contrast to the 150 kN specified by the European Eurocode. See Table 3.2. The relative differences in unity checks are thus further amplified, as the lower shear capacity is also divided by a lower load in the case of the ACI 440.

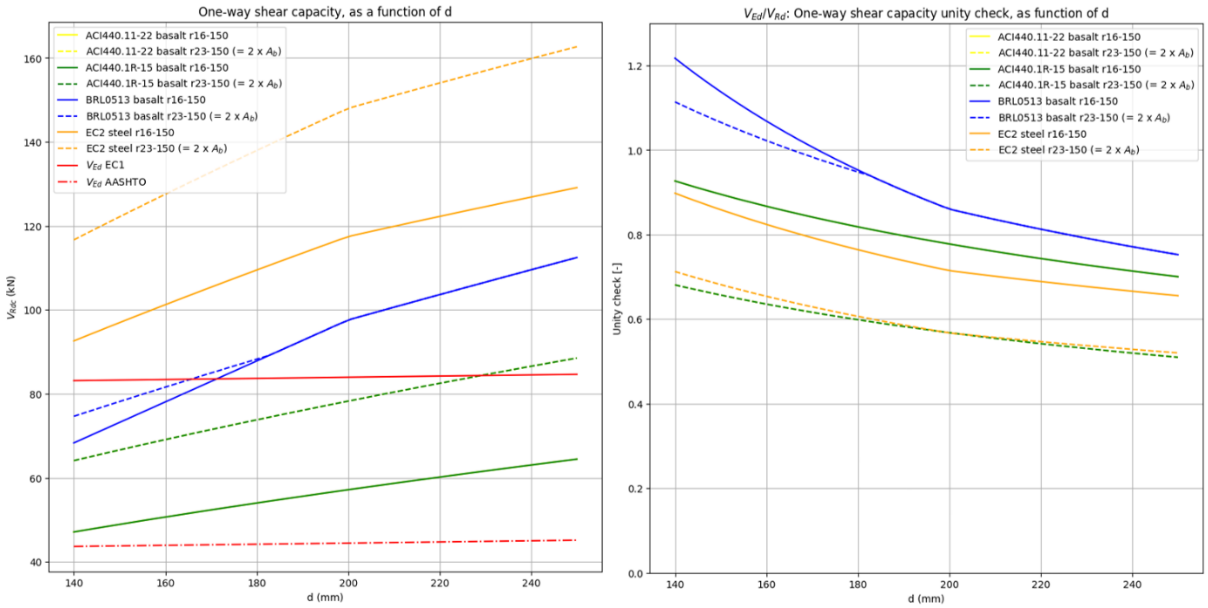

Figure 3.3: One-way shear capacity

3.4 Punching shear capacity analysis: comparison of design codes

For punching shear, it is again evident that BRL0513 provides significantly more conservative values in terms of unite checks, compared to ACI 440. Like one-way shear, the punching shear capacity increases with an increase in effective depth. It is also observed that the unity checks are much lower than the one-way shear values mentioned in the previous paragraph. Therefore, punching shear appears to be less governing than one-way shear.

It is further noteworthy that in the left plot of Figure 3.4, for low values of d, the BRL0513 and ACI440 punching shear capacities are close to each other, while the unity checks in the right plot are relatively further apart. This phenomenon can again be explained by the differences in maximum wheel loads according to Eurocode 1 and AASHTO. The AASHTO uses more than 50% lower maximum wheel loads than the Eurocode, resulting in a more conservative unity check for the BRL0513 values compared to the Eurocode 1 values.

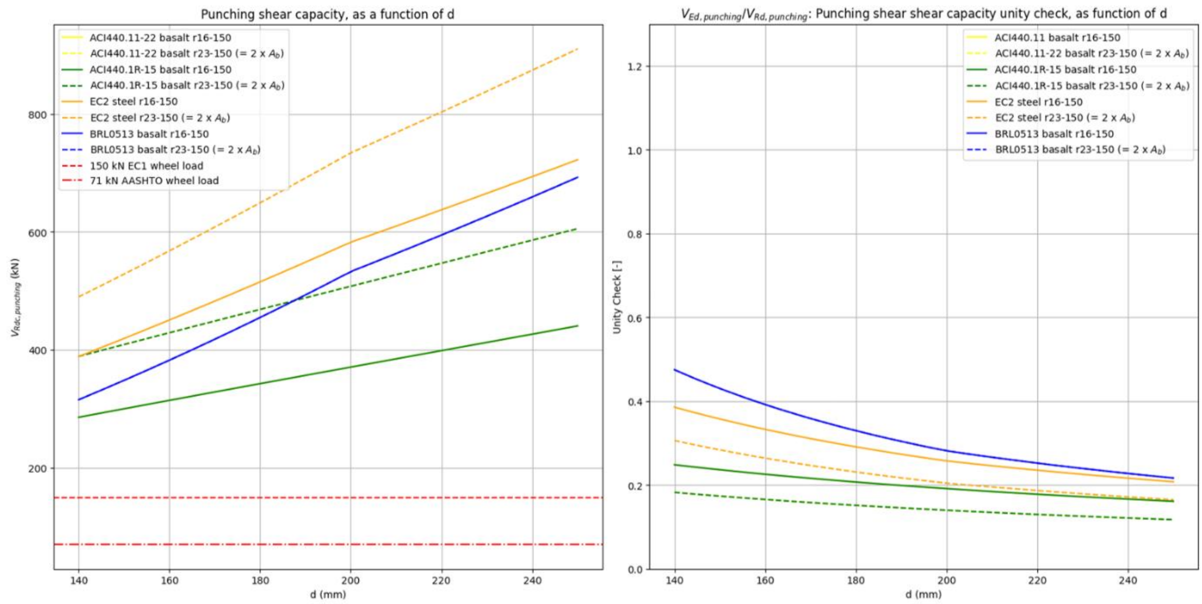

Figure 3.4: Punching shear capacity

3.5 Bending moment capacity analysis: comparison of design codes

Again, BRL0513 provides a much more conservative approach compared to ACI440. Furthermore, it is evident that ACI440 offers a unity check in terms of bending moment, which looks similar to traditional steel B500 reinforcement according to the Eurocode. Naturally, for bending moment capacity, the capacity increases with increasing effective depth. The obtained unity checks for bending moment are significantly lower than those for one-way shear as discussed in Section 3.3.

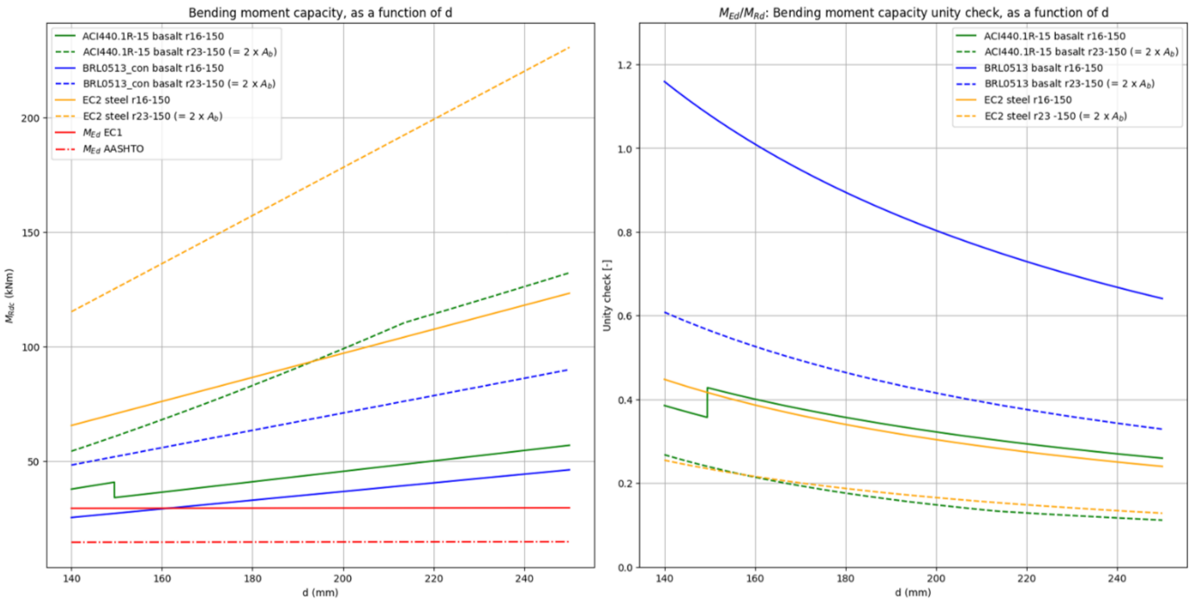

Figure 3.5: Bending moment capacity

Both plots in Figure 3.5 show a jump in the graph for the ACI 440 variant with a relatively high reinforcement ratio. This occurs because, from the point of the jump, a different factor, ϕ, is used for the calculation of the bending moment capacity. This factor depends on the reinforcement ratio of the cross-section. The different factors are shown below:

$$\Phi = 0{,}55 \quad for\ \rho_f \leq \rho_{fb}$$

$$\Phi = 0{,}3 + 0{,}25\frac{\rho_f}{\rho_{fb}} \quad for\ \rho_{fb} < \rho_f \leq 1{,}4\rho_{fb}$$

$$\Phi = 0{,}65 \quad for\ \rho_f \geq 1{,}4\rho_{fb}$$

3.6 Fatigue capacity analysis: comparison between steel and BFRP rebar

The fatigue capacity for reinforcement, is set at a maximum stress variation in the reinforcement that can occur for two million heavy vehicles per year. Since Rijkswaterstaat designs bridges for a lifespan of 100 years, the total number of stress variations must be chosen as 200 million.

For the maximum allowable stress variation for steel, the S-N curve from Section 6.8.4 of NEN-EN 1992-1-1+C2 (2011) is used in combination with table 6.3N. For k_2, the value for straight bars is 9 with an N* of 10^6 and $\Delta\sigma_{RsK}$ = 162,5 MPa. From these values, further extrapolation can be made to the number of $200*10^6$ heavy loading cycles. This results in a maximum allowable stress difference of 77 MPa. See Figure 3.6.1.

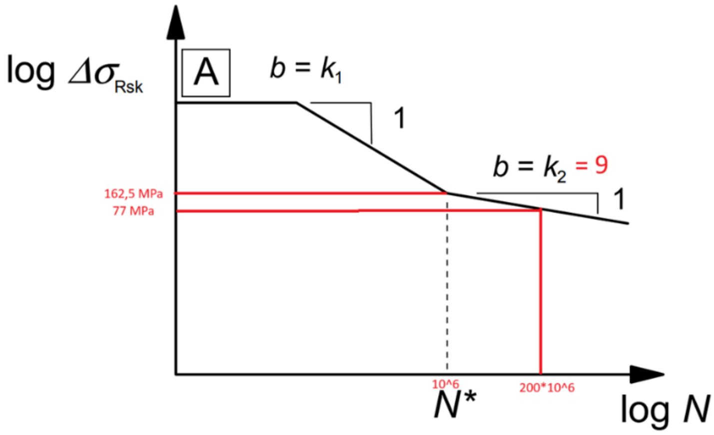

Figure 3.6.1: Fatigue reinforcing steel (NEN-EN 1992-1-1+C2, 2011)

Regarding the fatigue of BFRP rebar, current design standards and guidelines do not yet provide a method to determine the maximum allowable stress variation. However, research has been conducted on the fatigue behaviour of FRP reinforcement. For instance, El-Ragaby et al. (2007) investigated GFRP, which has very similar mechanical properties to BFRP. They also developed a fatigue equation that allows the fatigue life to be determined as a function of the number of loading cycles. From this, it follows that for $200*10^6$ cycles, a maximum allowable stress variation of 388 N/mm^2 applies. See Figure 3.6.2.

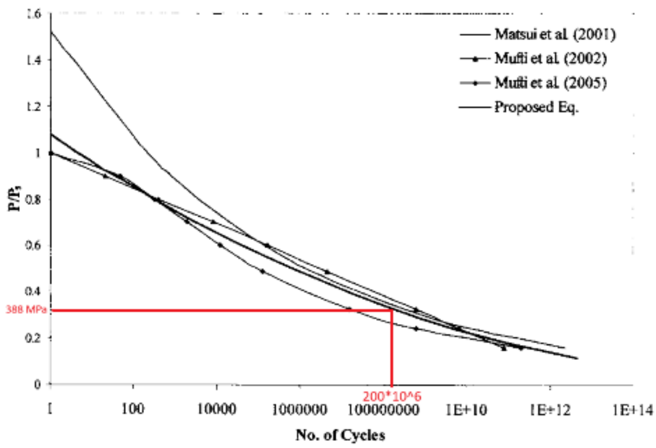

Figure 3.6.2: Fatigue FRP (El-Ragaby, El-Salakawy, & Benmokrane, 2007)

3.7 Summary and conclusion

Based on this preliminary analysis, it can be concluded that bending moment capacity and punching shear are most likely not the governing factors in concrete bridge decks when reinforced with BFRP. The higher unity checks of the one-way shear variant appear to be much more critical than the low values of bending moment capacity and punching shear. Only the BRL0513 shows a relatively high unity check for bending moment; however, this is based on the very conservative assumption of the BFRP design strength being only 13% of the characteristic strength. This value is obtained after applying the factor according to Annex R of the forthcoming Eurocode, as described in Section 2.3.2.
Nevertheless, it should be noted that the preliminary analysis is based on a simplified calculation considering a single span of the bridge deck over the T-beams. The effect of a multi-span bridge deck over multiple T-beams, with multiple loaded spans, was not included in this preliminary analysis. Only a single wheel load on a small section of the bridge deck, 1200 mm in width, was used. Nevertheless, this preliminary analysis provides a good initial indication of the governing failure mechanisms.

Regarding fatigue, it can be concluded that BFRP offers significantly more resistance to fatigue than steel reinforcement. For 200 million heavy loading cycles, the maximum allowable stress variation for steel reinforcement is $\Delta\sigma_{RsK}$ = 77 MPa, while for BFRP it is $\Delta\sigma_{RsK}$ = 388 MPa.

4. Case study description of a concrete bridge deck in an inverted T-girder bridge

Based on a case study, the effect of BFRP on the behaviour of the concrete bridge deck in an inverted T-girder bridge will be examined. This chapter will describe the geometry of the bridge, the elements and materials used, and the parameters varied in the numerical model. Finally, the governing traffic loading conditions will be addressed.

4.1 Structural geometry of the case study bridge

The dimensions of the bridge in this case study are illustrated in Figure 4.1.1 and Figure 4.1.2. The bridge will have a total span of 22 meters. The main span consists of 10 inverted T-beams of the HRP1150 type, with two RH edge girders on the sides. The centre-to-centre distance of the T-girders is 1200 mm, while the centre-to-centre distance between T-girder and RH-girder is 800 mm. The height of the cast-in-situ concrete bridge deck is 250 mm; however, this is a variable that will be modified in the variant study. Cross beams will be placed at the beginning and end of the bridge to connect the T-girders. To simplify the model, it is assumed that the bridge is flat and spans perpendicularly at an angle of 90 degrees.

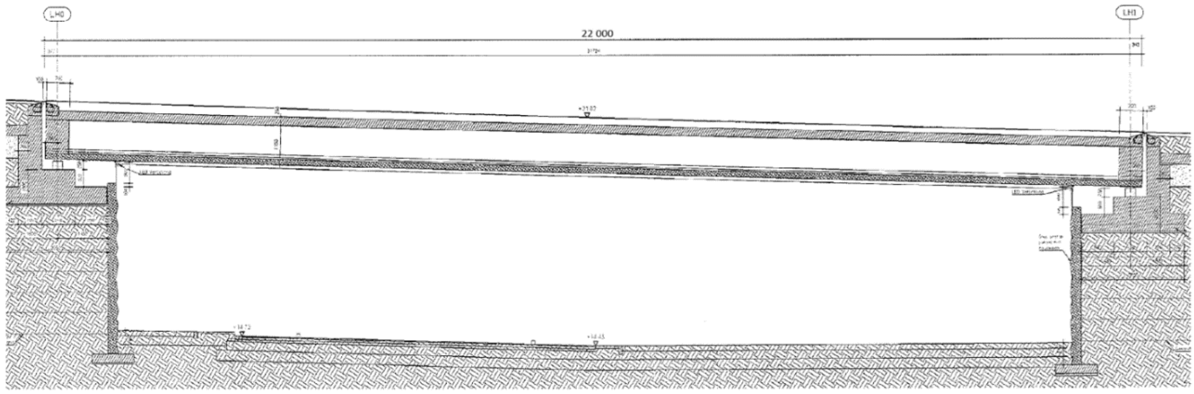

Figure 4.1.1: Longitudinal cross-section

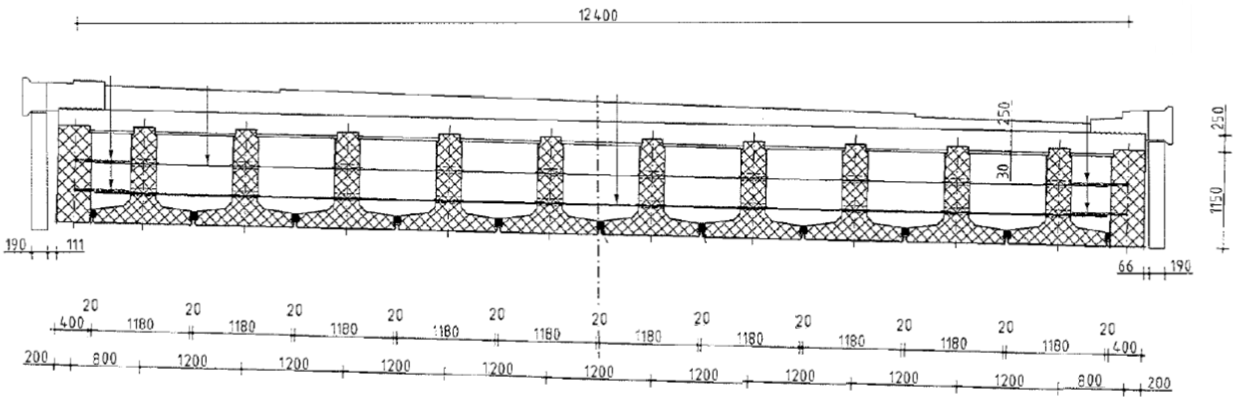

Figure 4.1.2: Transverse cross-section

4.2 Detailed cross-sections and construction materials

Below an overview is given of the cross sections with the corresponding material types.

Inverted T-girder

Material: C60/75

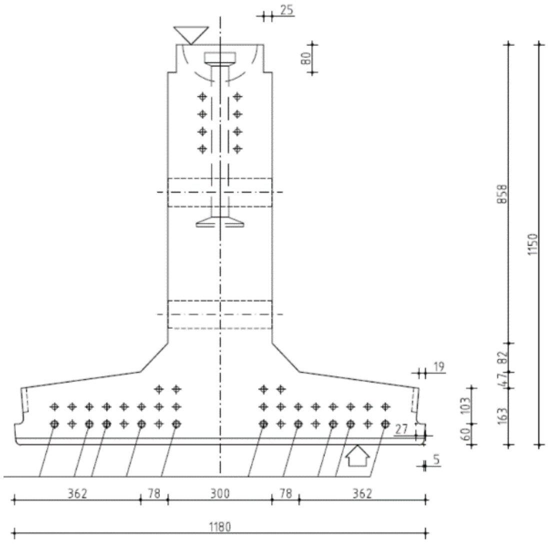

Figure 4.2.1: Cross-section HRP1150

RH-girder

Material: C60/75

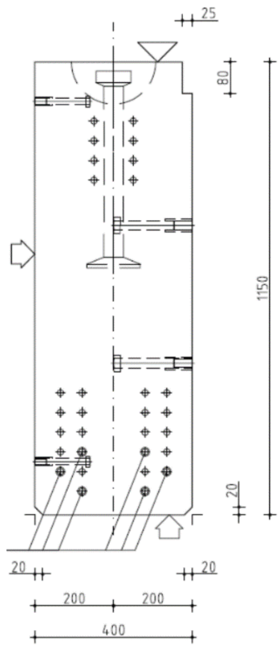

Figure 4.2.2: Cross-section RH-girder

Bridge deck

Material: C30/37

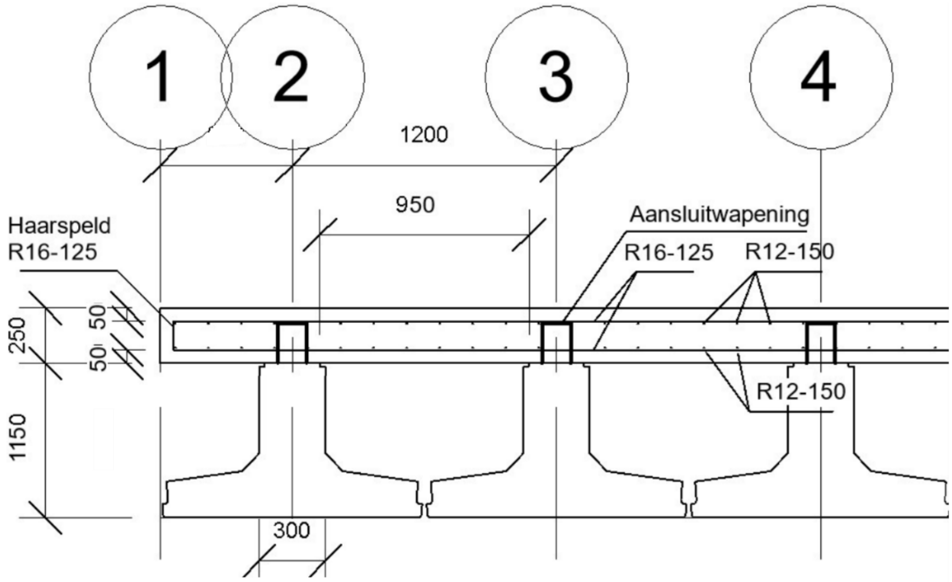

Figure 4.2.3: Bridge deck

4.3 Bridge deck design variants to be analysed

In this case study, the load transfer of various in-situ cast bridge deck variants is considered. As a reference, a traditional variant with steel reinforcement of φ16-125 mm and a concrete cover of 50 mm on both the top and bottom of the cross-section will be examined. Subsequently, a variant will be tested with a one-to-one replacement of steel with BFRP. The next step involves assessing the effect of reducing the total height by decreasing the cover. This reduction is allowed because BFRP has lower environmental class requirements, as described in Section 2.3.4. Both the reduction of cover with increase in effective depth have been considered, as well as the reduction of cover with decrease in total cross-sectional height. Finally, the amount of BFRP reinforcement will be doubled to observe its impact. BFRP has an ECI of approximately 50% that of steel. Doubling the reinforcement volume will result in the same ECI score for reinforcement. Therefore, the environmental benefit will be entirely attributed to the reduction in the amount of concrete used.

Table 4.3: Bridge deck design variants

Variant	Material	Height	Cover	A_s	$\rho_{\%}$
S-r16-s125-h250-c50	Steel	250 mm	50 mm	16-125 mm	0,64%
B-r16-s125-h250-c50	Basalt	250 mm	50 mm	16-125 mm	0,64%
B-r16-s125-h250-c25	Basalt	250 mm	25 mm	16-125 mm	0,64%
B-r16-s125-h200-c25	Basalt	200 mm	25 mm	16-125 mm	0,84%
B-r20-s100-h200-c25	Basalt	200 mm	25 mm	20-100 mm	1,57%

4.4 Traffic load analysis

This section will present the loads considered in the model calculations. The focus of this model will be solely on vertical traffic loads. Horizontal loads, wind, snow, temperature, and seismic loads are excluded. The self-weight is also excluded to focus only on the effect of changing bridge deck stiffness due to changes in rebar type and slab thickness. The traffic loads considered are derived from Eurocode 1 with the recommended values from Dutch National Annex. First, an explanation of the lane layout from Eurocode 1 will be given. Subsequently, the critical load arrangements for both bending moment and shear force in the transverse direction of the bridge will be provided, as this is the direction in which the bridge deck is most heavily loaded.

4.4.1 Layout of lanes according to NEN-EN 1991

The loads from road traffic, consisting of cars, trucks, and special vehicles (e.g., for industrial transport), generate vertical and horizontal, static and dynamic forces. For this analysis, only the vertical traffic loads are considered, as previously described.
To establish the traffic load model, the width of the bridge must first be divided into several theoretical lanes according to Table 4.4.1:

Table 4.4.1: Number and width of lanes in model (NEN-EN 1991-2+C1, 2015)

Carriageway width w	Number of Notional lanes	Width of a notional lane w_l	Width of the Remaining area
$w < 5,4$m	$n_1 = 1$	3 m	$w - 3$m
$5,4$m $\leq w < 6$m	$n_1 = 2$	$\frac{w}{2}$	0
6m $< w$	$n_1 = Int\left(\frac{w}{3}\right)$	3 m	$w - 3 * n_1$
NOTE For example, for a carriageway width equal to 11m, $n_1 = Int\left(\frac{w}{3}\right) = 3$, and the width of the remaining area is $11 - 3 * 3 = 2$m			

The positioning of the lanes does not necessarily have to be related to their numbering. Additionally, the positioning of the different lanes may vary for different assessments, such as shear force, deflection, or bending moment. The positioning should be chosen in each case to achieve the most unfavorable scenario. For fatigue load models, the positioning should be chosen in the most representative manner of the expected traffic. The lane with the most unfavorable effect is designated as lane number 1, while the next most unfavorable is designated as lane number 2, and so on.

For local assessment, the wheel loads should be evenly distributed over their contact area. The distribution occurs at an angle of 45 degrees. The load must be spread through the entire asphalt layer and half of the cast-in-situ concrete bridge deck, ultimately reaching at its neutral axis.

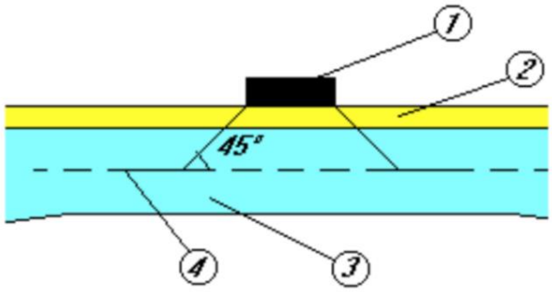

Key
1 Wheel contact pressure
2 Pavement
3 Concrete slab
4 Middle surface of concrete slab

Figure 4.4.1: Wheel load distribution through asphalt layer and concrete bridge deck (NEN-EN 1991-2+C1, 2015)

Load Model 1 describes traffic loads originating from truck and car traffic and is therefore applicable for this case and scope. Load Model 2 is based on a single axle load with a specific wheel contact area, making it more relevant for the dynamic effects of regular traffic on the structure. Load Model 2 will still be analyzed for shear force as the wheel load here is larger than in Load Model 1 and this may give a larger shear force effect. Load Model 3 describes loads for special vehicles, and Load Model 4 is intended for assessments due to crowd loading. Therefore, these last two models are not applicable to this case.

4.4.2 Eurocode Load Model 1

Load Model 1 can be applied to road traffic bridges where the length over which the load is applied is less than 200 meters. Therefore, it is highly applicable to this case study. The model does not describe actual loads but is derived from modeling and calibration (including amplification factors and dynamic effects) such that the effects correspond to those of actual traffic in European countries in the year 2000 (NEN-EN 1991-2+C1, 2015).
Load Model 1 consists of both uniformly distributed loads and concentrated loads in the form of double axle loads, each varying per notional lane. The principles of the double tandem systems and uniformly distributed loads are provided below.

Axle load:	*UDL Load:*
$\alpha_Q Q_k$	$\alpha_q q_k$

with α_Q and α_q as correction factor

- A maximum of one tandem system may be placed per notional lane
- Only complete tandem systems may be used
- Tandem systems must be assumed to be centred along the axis of the theoretical lane
- Each wheel load of the respective tandem system must be equal to $0{,}5\alpha_Q Q_k$
- The contact area of each wheel load is 0,4m x 0,4m

Table 4.4.2.: Load Model 1 values, incorporating Dutch Annex (NEN-EN 1991-2+C1, 2015)

Location	**Tandem system Axle loads $\alpha_{Qi}Q_{ik}$ [kN]**	**UDL system $\alpha_q q_{ik}$ [kN/m^2]**
Lane Number 1	α_{Q1} * 300 = 300	α_{q1} * 9 = 10,35
Lane Number 2	α_{Q2} * 200 = 200	α_{q2} * 2,5 = 3,5
Lane Number 3	α_{Q3} * 100 = 100	α_{q3} * 2,5 = 3,5
Other lanes	0	α_{qi} * 2,5 = 3,5
Remaining area	0	α_{qr} * 2,5 = 3,5

The dimensions of the tandem systems and their locations within the lanes are provided in Figure 4.4.2.

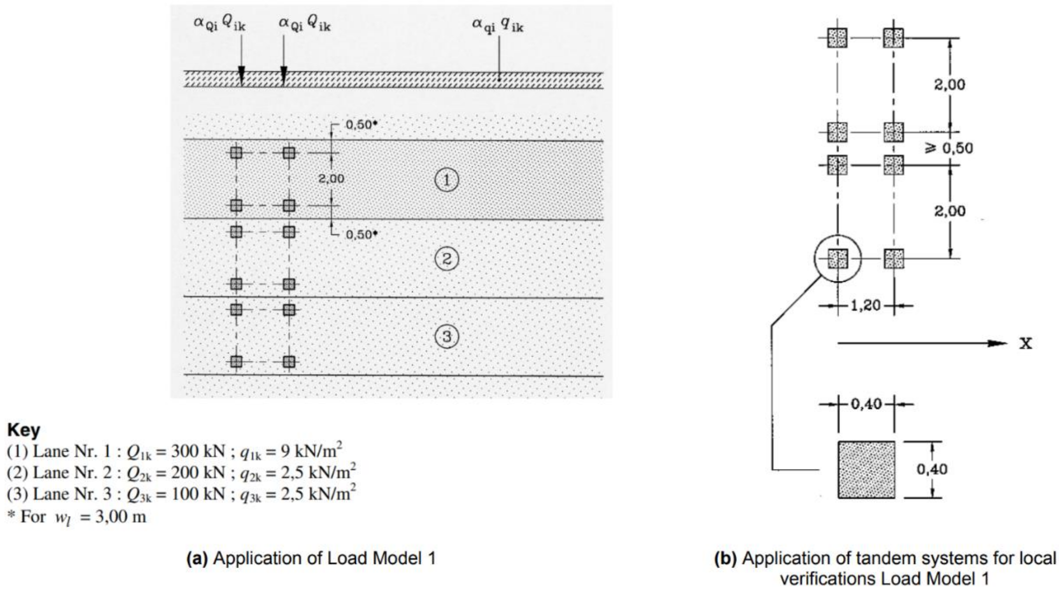

Figure 4.4.2: Load Model 1 (NEN-EN 1991-2+C1, 2015)

4.4.3 Eurocode Load Model 2

Load Model 2 consists of a single axle load, $\beta_Q Q_{ak}$, which should be applied at any arbitrary position on the roadway. The value of Q_{ak} is 400 kN, including the amplification factor for dynamic effects. However, when relevant, only one wheel load of 200 kN may be considered. The value of β_Q can be found in the National Annex.

Table 4.4.3: Load Model 2 values, incorporating Dutch Annex (NEN-EN 1991-2+C1, 2015)

Location	**Tandem system Axle load $\beta_Q Q_{ik}$ [kN]**	**UDL system $\alpha_q q_{ik}$ [kN/m^2]**
Arbitrary position	β_Q * 400 = 400	Not applicable

The dimensions of the tandem system are provided in Figure 4.4.3.

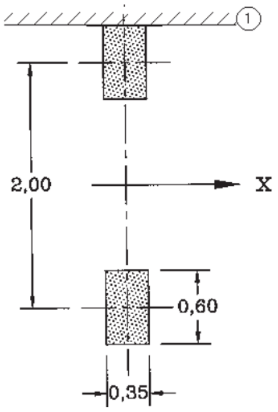

Verklaring

X Lengterichting van de brug
1 Stootrand

Figure 4.4.3: Load Model 2 (NEN-EN 1991-2+C1, 2015)

4.4.4 Traffic Load arrangement – globally

To determine the critical load configurations for the concrete bridge deck of this bridge, it is essential to consider when the maximum loading occurs in transverse direction. Subsequently, at the local level, the tandem loading should be positioned to generate maximum bending moment and shear force in transverse direction.

Maximal loading transverse direction

To determine the transverse behavior of the cast-in-situ concrete bridge deck under critical conditions, the traffic load configuration must be selected to maximize the effect on the transverse direction of the bridge deck. Malan & van Rooyen (2013) described how the traffic loading should be positioned for achieving the maximum transverse bending moment in the bridge deck. This effect is achieved in Load Model 1 when Lane Number 1 is positioned in the center, with Lanes Number 2 and 3 placed next to it. Additionally, the tandem systems should be precisely located in the center of the bridge. See Figure 4.4.4 for a representation of the traffic load configuration.

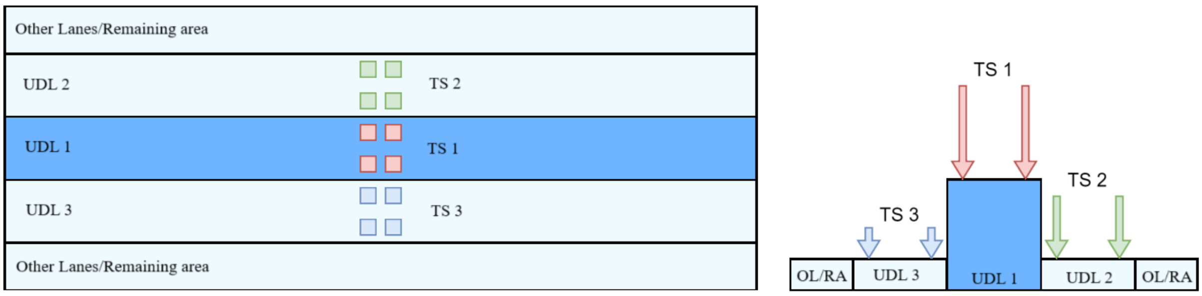

Figure 4.4.4: Traffic load configuration for maximum loading in transverse direction

The configuration as presented above applies to the load in the transverse direction on a global scale. It is now necessary to zoom in on the local effect of small displacements of the loads in transverse direction. By giving the notional lanes small displacements, a wheel load from TS1 can be positioned between two T-girders in such a way that it generates a maximum bending moment or shear force in the bridge decks transverse direction.

4.4.5 Traffic Load arrangement – locally

The focus will now shift to a single wheel load, and a description will be provided on how it should be positioned to generate the maximum transverse bending moment and shear force

Maximum bending moment transverse direction

To generate a maximum transverse bending moment in the cast-in-situ concrete bridge deck, notional lane 1 must be positioned such that a wheel load acts precisely at the midpoint of the span between two T-girders. The area over which the wheel load acts on the asphalt is 400x400 mm. By spreading the load through the asphalt layer and half of the bridge deck at a 45-degree angle, as described in Figure 4.4.1, it is assumed that the load on the neutral axis of the bridge deck is distributed over an area of 600x600 mm.

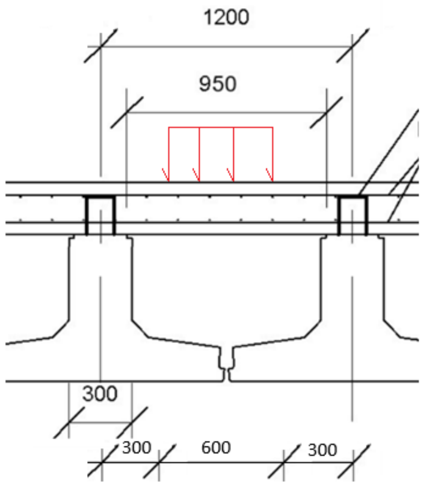

Figure 4.4.5.1: Position wheel load maximum transverse bending moment

Maximum shear force in transverse direction

The location of the wheel load is crucial for the maximum occurring shear force. The closer the wheel load is placed to the support (in this case the web of the T-girder), the higher the resulting shear force. However, one must be aware of the effect of the shear span to depth ratio. When the load is placed very close to the support, arching action will occur, causing the load to be transferred less as shear force and more as a compression arch. As described in Section 2.2.5 of this research. Eurocode 2 indicates in Section 6.2.2 that loads within 2d of the support may be reduced for shear force by a factor β (NEN-EN 1992-1-1+C2, 2011).
When the load is placed within 0,5d of the support, it should be reduced to one-quarter of the original load. From 0,5d to 2d from the support, the load increases linearly to the original load value. This is illustrated graphically in Figure 4.4.5.2.

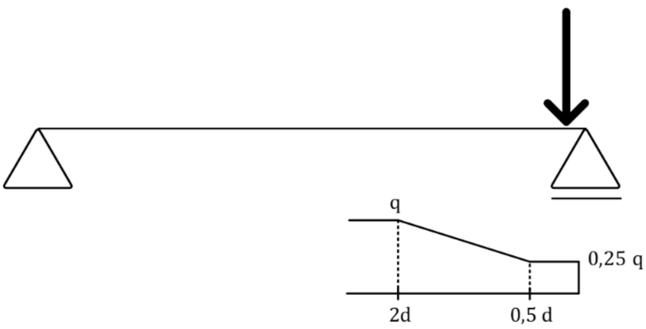

Figure 4.4.5.2: Graphical representation of load reduction for shear force, according to NEN-EN 1992

In the case of elements with a relatively large span compared to the effective depth, d, the reduction within the area close to the support is more significant than the additional shear force it generates. In such cases, the load is positioned at 2d from the support. However, for a bridge deck between two inverted T-girders, the span is very small compared to the effective depth, so placing a wheel load at 2d results in a significant portion of the load being transferred to the other side of the span. Therefore, a study must be conducted to determine the critical location of the wheel load within the span between the inverted T-girders.

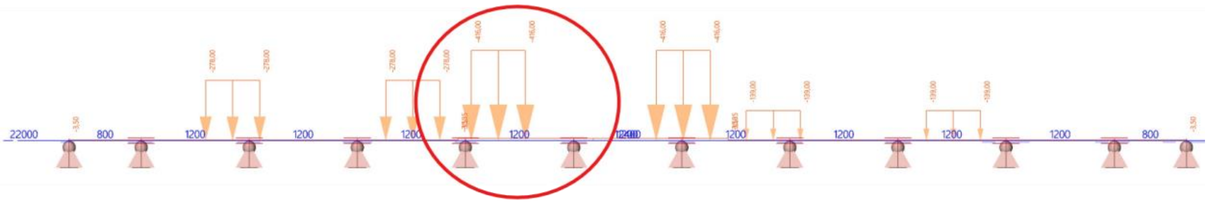

Figure 4.4.5.3: Zoomed location in cross section of bridge deck, LM1

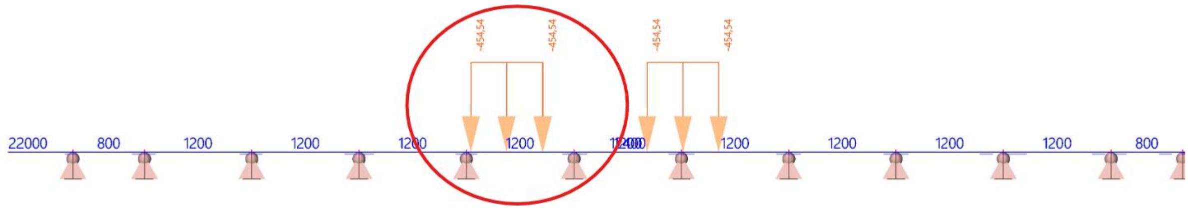

Figure 4.4.5.4: Zoomed location in cross section of bridge deck, LM2

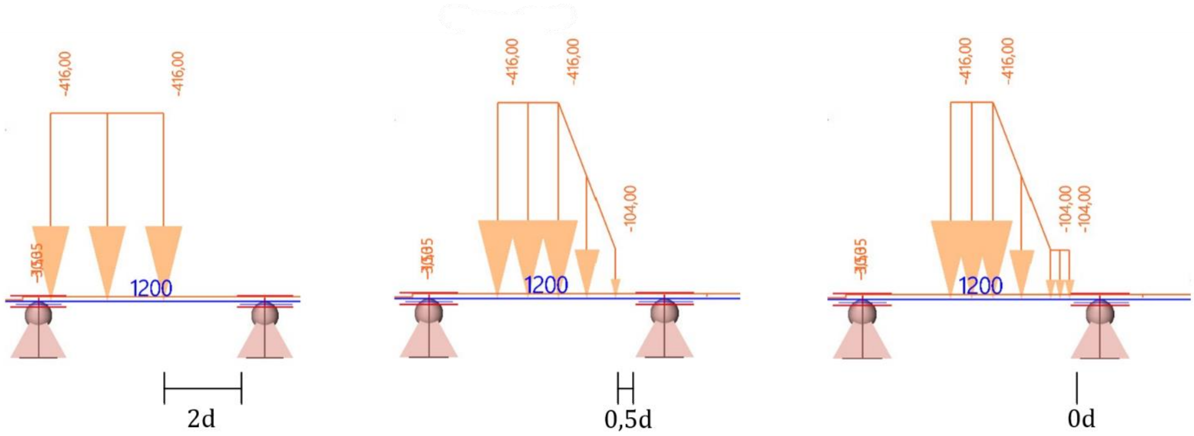

Figure 4.4.5.5: Variants for maximum shear force study

The study showed that for each design variant of the bridge deck, the wheel load configuration with the load placed at a distance of 0,5d generates the maximum shear force. The 2d variant results in significantly lower values, as almost all the load is transferred to the other side of the span. The outcomes of this variant study can be found in APPENDIX E.

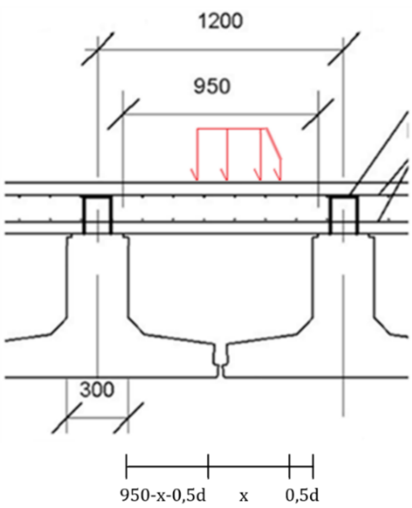

*The distance x is different for Load Model 1 and Load Model 2

Figure 4.4.5.3: Position wheel load maximum transverse shear force

4.5 Summary and conclusion

This section summarizes the case study description of the concrete bridge deck in an inverted T-girder bridge:

Case Study:

- The case study involves a bridge deck with a span of 22 meters and a width of 12,4 meters, made from C30/37 concrete.
- The bridge features 10 inverted T-girders, 2 cross-end girders, and 2 edge girders, made from C60/75 concrete.
- The bridge deck has 5 different design variants: a steel-reinforced reference variant, a variant with a one-to-one replacement of steel with BFRP, a variant with BFRP and reduced concrete cover, a variant with BFRP and reduced concrete cover combined with a lower construction height, and a similar variant with double the amount of BFRP reinforcement.

Traffic loading:

- The governing transverse bending moments will be calculated using Load Model 1 according to NEN-EN 1991-2. The critical wheel load will be placed exactly in the middle of the bridge deck span between two inverted T-girders.
- The governing transverse shear forces are calculated using Load Model 1 and Load Model 2 according to NEN-EN 1991-2. The wheel loads are placed at a distance 0,5d from the inverted T-girders with a linearly decreasing reduction according to NEN-EN 1992, Section 6.2.2.

5. Numerical modelling of deformations and cross-sectional forces

In this chapter, the outcomes of the quasi linear FEA conducted in SCIA Engineer for each design variant are discussed. First, the construction of the numerical model is explained, along with the assumptions and principles that were followed. Then, the deflection of the cast-in-situ concrete bridge deck is examined. Subsequently, for each variant, the maximum bending moment and the maximum shear force in the transverse direction are determined.

5.1 Development and principles of the numerical model

This paragraph will provide a description of the linear numerical model used to determine the load transfer in the concrete bridge deck. The bridge deck will be modeled as an orthotropic plate with centroidal ribs, where the centroidal ribs represent the inverted T-beams. In addition to the inverted T-beams, the end cross girders and edge girders will also be modeled as ribs. The properties and numerical considerations of the modeled elements will be elaborated in more detail in the following sections.

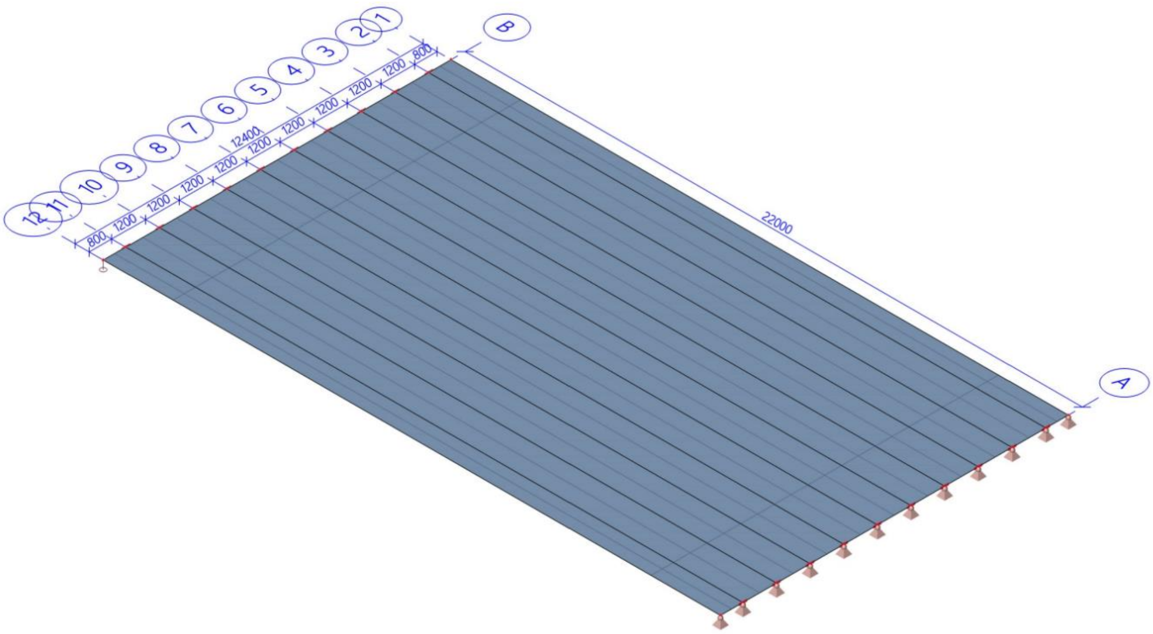

Figure 5.1: Overview of numerical model, orthotropic plate with centroidal ribs in SCIA Engineer

5.1.1 Orthotropic plate modelling of the bridge deck

Cracking

The cast-in-situ concrete bridge deck is modeled in the numerical model as an orthotropic 2D shell element. It is assumed that the bridge deck is fully compressed in the longitudinal direction and therefore uncracked. In the transverse direction, it is assumed that the concrete is cracked, resulting in lower stiffness. As described by Gilbert (2013), the stiffness of cracked concrete is lower than that of uncracked concrete, which should be considered in the orthotropic properties. Figure 5.1.1.1 clearly shows that up to the cracking moment, the stiffness is relatively high and linear elastic. Subsequently, the first cracks appear, after which the reinforcement starts to work, leading to a significant decrease in stiffness, as evidenced by the flattening of the M-kappa curve.

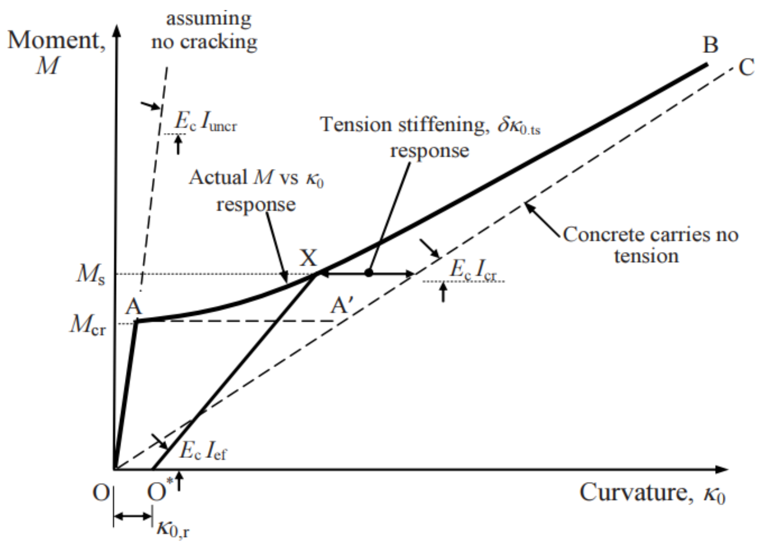

Figure 5.1.1.1: Stiffness after cracking (Gilbert, 2013)

Creep

For the long-term effect of the bridge deck, creep must also be considered. Concrete is a heterogeneous material. It is not purely elastic and does not exhibit linear deformation behavior. Therefore, concrete does not fully return to its original shape after the removal of a certain load. Since the long-term effect is also included in this numerical model, the value of the E-modulus must be corrected for creep in the structural calculations. The correction of the E-modulus for creep applies to both the longitudinal uncracked and transverse cracked stiffness. These corrected E-moduli will thus be incorporated into the orthotropic parameters of the slab.

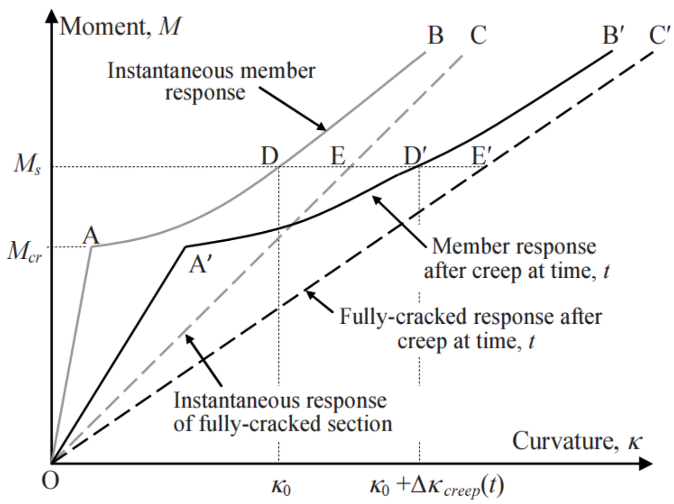

Figure 5.1.1.2: Stiffness after creep (Gilbert, 2013)

Effective E-modulus
To determine the effective E-modulus of each cross-section from Table 4.3, M_{cr} and M_{Rd} are calculated along with their corresponding curvatures. Subsequently, the effective stiffness is determined by the slope from the origin of the graph to the value $0{,}8M_{Rd}$. The effective E-modulus can then be obtained by dividing the effective flexural stiffness (EI) by the moment of inertia (I). Below the M-kappa graph for the reference variant with steel reinforcement is given.

$$M_{cr} = W * f_{ctm} = \frac{bh^2}{6} * f_{ctm}$$

$$k_{cr} = \frac{M_{cr}}{E_c I_c}$$

$$x_{ULS_{elas}} = \frac{-A_s + \sqrt{A_s^2 + 2 * \frac{f_{cd}}{\varepsilon_{c3} * E_s} * A_s * d * b}}{\frac{f_{cd}}{\varepsilon_{c3} * E_s} * b}$$

If $\quad \frac{\varepsilon_y}{d - x_{ULS_{elas}}} * x_{ULS_{elas}} \leq \varepsilon_{c3} = 0{,}00175$

$$M_{ULS,elas} = z_{ULS\_elas} * f_{yd} * A_s$$

Otherwise

$$M_{ULS,elas} = \frac{1}{2} x_{ULS,elas} * b * f_{cd} * z_{ULS\_elas}$$
$$k_{ULS,elas} = \frac{\varepsilon_{cULS_{elas}}}{x_{ULS,elas}}$$

$$x_u = \frac{A_s * f_{yd}}{\alpha_2 * b * f_{cd}} = \frac{A_s * f_{yd}}{0{,}75 * b * f_{cd}}$$

$$M_{Rd} = z_u * f_{yd} * A_s$$

$$k_{Rd} = \frac{\varepsilon_{c,u3}}{x_u} = \frac{0{,}0035}{x_u}$$

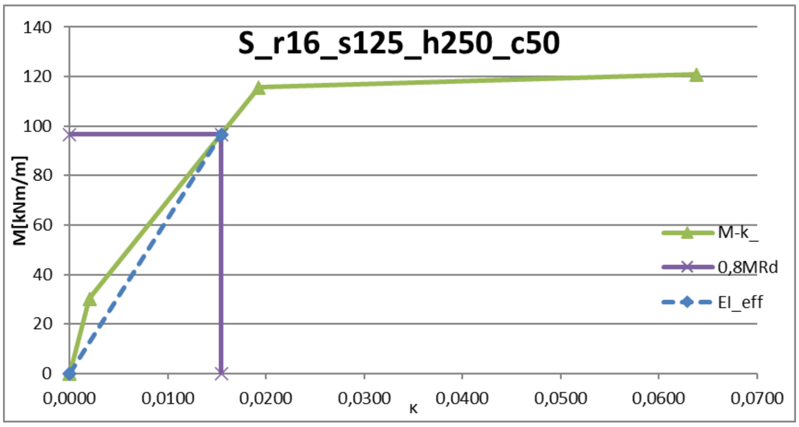

Figure 5.1.1.3: M-k graph of S_r16_s125_h250_c50

Table 5.1.1.1: Values M-k graph of S_r16_s125_h250_c50

Variant	M_{cr} [kNm/m]	k_{cr} [/m]	M_{Rd} [kNm/m]	k_{Rd} [/m]	0,8 M_{Rd} [kNm/m]	$k_{0,8MRd}$ [/m]
S-r16-s125-h250-c50	30	0,0020	121	0,063	97	0,015

The same principle can also be applied to BFRP bars. The question that arises is which design strength for the BFRP bars should be used to determine M_{Rd}. For the previously calculated steel variant, this is very straightforward as it is well known that the design strength f_{yd} is 435 N/mm². For BFRP, this is different.

Firstly, BFRP does not yield, so there is no actual yield strength. However, various codes and guidelines provide recommendations for the design strength to be used in capacity calculations. When using the strength from the upcoming Eurocode, FprEN_1992-1-1:2022, this proves to be a very conservative approach. When the factors are applied as recommended (see Section 2.3.2), the resulting design strength is:

$$f_{ftk,100a} = C_t * C_C * C_e * f_{ftk0} = 1{,}0 * 0{,}8 * 0{,}35 * 0{,}7 * 1200 = 235{,}2\ N/mm^2$$

$$f_{ftd} = \frac{f_{ftk,100a}}{\gamma_{FRP}} = \frac{235{,}2}{1{,}5} = 156{,}8\ N/mm^2$$

This value is very conservative and will ultimately result in a low bending moment capacity and an effective E-modulus of the cracked section that is even higher than that of the steel-reinforced variant. This is due to the fact that the M_{Rd} value in this case is only slightly higher than the M_{cr}. For the continuation of this study, the strength of the BFRP is assumed according to the fib Model Code 2020 and fib Bulletin 40. From Table 3-11 of fib Bulletin 40, the design value of the strength is obtained. Although no specific value is given for BFRP, it is assumed that the GFRP values are representative due to the similarities in material properties. The red colored row is chosen as it best describes the conditions, namely outdoor use, an average temperature of 10 °C and a service life of 100 years. This gives a tensile strength of f_{td} = 441 N/mm^2.

Table 3-11: Examples for environmental design

Material	f_{tk0} MPa	f_{tk1000} MPa	R_{10}	Moist. cond.	n_{mo}	MAT °C	n_T	Serv Life years	n_{SL}	n	$\eta_{env,t}$	$1/\eta_{env,t}$	γ_f	f_f N/mm²
CFRP class 1	2000	2000	3%	Dry	-1	10	0	100	3	2,0	1,1	94%	1,25	1505
CFRP class 2	2000	2000	5%	Dry	-1	10	0	100	3	2,0	1,2	90%	1,25	1444
AFRP class 1	2000	1800	15%	Dry	-1	10	0	100	3	2,0	1,6	65%	1,25	1040
GFRP class 2	1400	1000	20%	Dry	-1	10	0	100	3	2,0	1,9	46%	1,25	512
GFRP class 3	650	366	25%	Wet	1	20	0,5	50	2,7	4,2	5,9	17%	1,25	87
GFRP class 3	650	366	25%	Wet	1	10	0	1	1	2,0	3,2	32%	1,25	165
GFRP class 3	650	366	25%	Dry	-1	20	0,5	100	3	2,5	3,6	27%	2,25	143
GFRP class 1	1100	1000	18%	Wet	0	10	0	100	3	3,0	1,8	55%	1,25	441
GFRP class 1	1100	1000	18%	Wet	1	10	0	1	1	2,0	1,5	67%	1,25	538
GFRP class 1	1100	1000	18%	outdoor	0	30	1	100	3	4,0	2,2	45%	1,25	362

Table 5.1.1.2: Chosen design tensile strength BFRP (fib bulletin 40, 2007)

To highlight the effect of the BFRP strength differences between FprEN_1992-1-1:2022 and the fib Model Code 2020 in combination with fib Bulletin 40, the M-kappa graphs for both cases are shown below. It is clearly visible what the effect is of using the very conservative value of the BFRP strength from the Eurocode, namely a high effective stiffness and low bending moment capacity. This is because the moment capacity is very close to the cracking moment, resulting in a very steep EI_eff line. Next to this the linear elastic behavior of the BFRP rebar is better represented by the fib bulletin40 values.

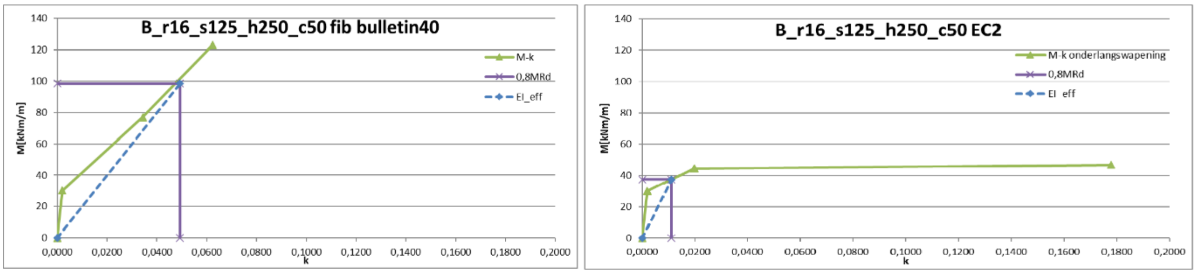

Figure 5.1.1.4: Differences M-kappa graphs for BFRP strengths fib bulletin40 and FprEN_1992-1-1:2022

For all the variants to be investigated from Table 4.3, the effective E-moduli were calculated using the tensile strength from fib Bulletin 40. The values are presented in Table 5.1.1.3. The M-kappa graphs can be found in APPENDIX A.

Table 5.1.1.3: Effective E-moduli in longitudinal and transverse direction

Variant	**$E_{eff,lon}$ [N/mm^2]** **uncracked*	**$E_{eff,trans}$ [N/mm^2]** **cracked*
S-r16-s125-h250-c50	11800	4876
B-r16-s125-h250-c50	11500	1523
B-r16-s125-h250-c25	11600	2089
B-r16-s125-h200-c25	11600	2237
B-r20-s100-h200-c25	11600	3585

With the different E-moduli and heights of the variants, the parameters for the orthotropic plate can be calculated. The parameters have the following meanings in the numerical software program SCIA Engineer

- D11: Flexural stiffness in the “x” direction
- D22: Flexural stiffness in the “y” direction
- D12: Mixed stiffness of D11 and D22 (transverse contraction)
- D33: Torsional stiffness
- D44: Shear flexural stiffness in the "x" direction
- D55: Shear flexural stiffness in the "y" direction

- d11: Normal membrane stiffness in the "x" direction (stretching)
- d22: Normal membrane stiffness in the "y" direction
- d12: Mixed stiffness of "d11" and "d22" (transversal contraction)
- d33: Shear membrane stiffness

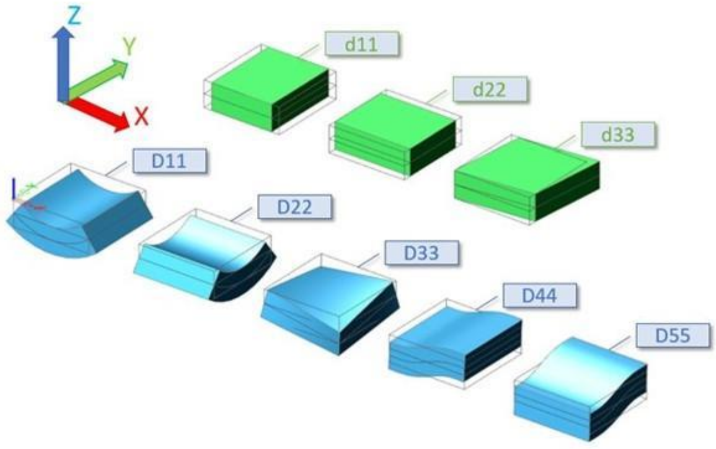

Figure 5.1.1.5: Graphical representation of the orthotropic plate parameters in SCIA Engineer (SCIA Engineer, n.d.)

Parameter formulas:

$$D_{11} = \frac{E_1 * h^3}{12 * (1 - \nu_{12} * \nu_{21})}$$

$$D_{22} = \frac{E_2 * h^3}{12 * (1 - \nu_{12} * \nu_{21})}$$

$$D_{12} = D_{21} = \nu_{21} * D_{11} = \nu_{12} * D_{22}$$

$$D_{33} = \frac{G_{12} * h^3}{12}$$

$$D_{44} = \frac{G_{13} * h}{1,2}$$

$$D_{55} = \frac{G_{23} * h}{1,2}$$

$$d_{11} = \frac{E_1 * h}{(1 - \nu_{12} * \nu_{21})}$$

$$d_{22} = \frac{E_2 * h}{(1 - \nu_{12} * \nu_{21})}$$

$$d_{12} = d_{21} = \nu_{21} * d_{11} = \nu_{12} * d_{22}$$

$$d_{33} = G_{12} * h$$

$$K_{xy} = \frac{E_1}{2 * (1 + \nu_1)} * \alpha * h^3 * b$$

$$K_{yx} = \frac{E_2}{2 * (1 + \nu_2)} * \alpha * h^3 * b$$

For this case:

$$\alpha = 0{,}33$$

And

$$G_{12} = \frac{\sqrt{E_1 E_2}}{2(1 + \sqrt{\nu_{12}\nu_{21}}}$$

$$G_{13} = \frac{E_1}{2 * (1 + \nu_{12})}$$

$$G_{23} = \frac{E_2}{2 * (1 + \nu_{12})}$$

5.1.2 Centroidal rib modelling of bridge girders

The girders are all modeled as centroidal ribs, which are 1D elements integrated into the bridge deck. The T-girders, end cross girders and edge girders provide stiffness against bending and help distribute the traffic loads from the concrete bridge deck. Simplifying the model with centroidal ribs prevents the creation of moments due to eccentricity, which would otherwise cause additional normal stresses in the concrete bridge deck. This study focuses primarily on the distribution of traffic loads in the transverse direction rather than on internal stresses. Since the bridge deck is made of C30/37 concrete and the girders are made of C60/75 concrete, the width of the concrete bridge deck above the T-girders is adjusted according to the differences in Young's moduli. This ensures that the rib has the same bending and torsional stiffness properties as the composite equivalent. Below is a representation of the rib elements.

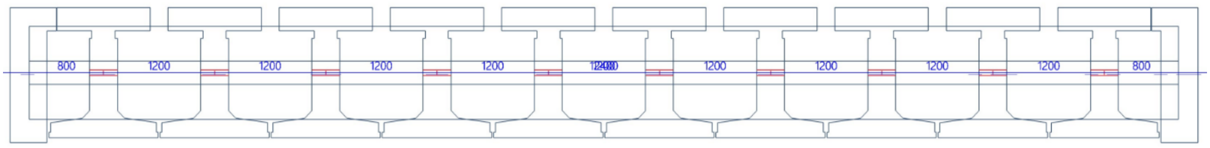

Figure 5.1.2.1: Graphical representation centroidal ribs

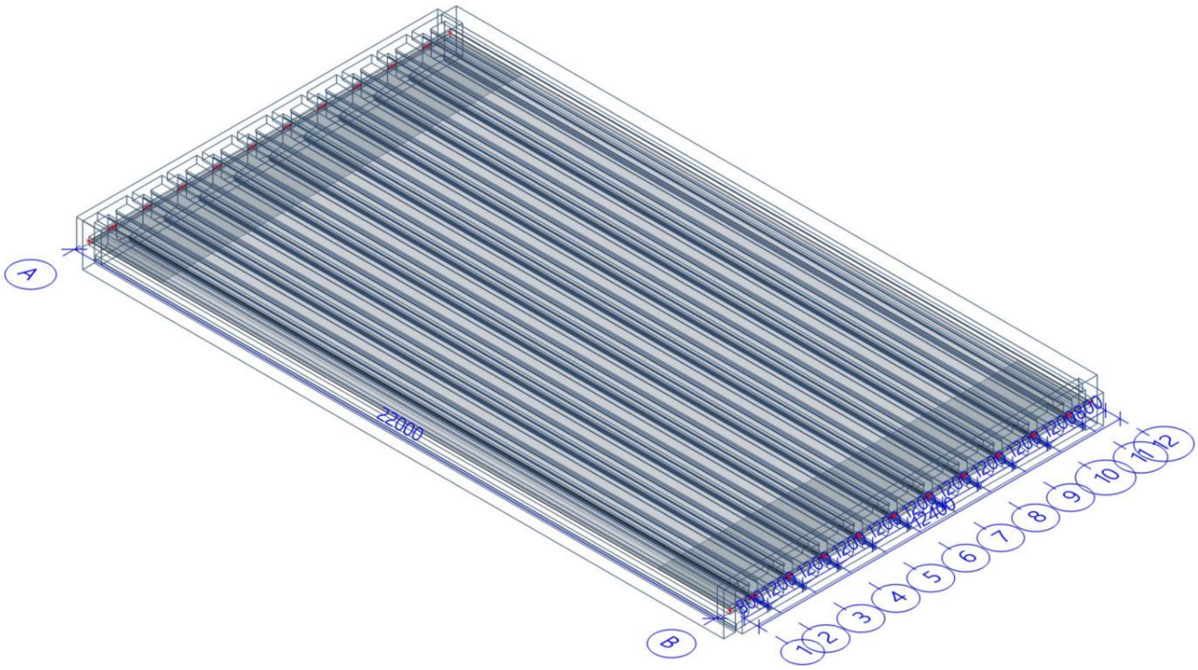

Figure 5.1.2.2: 3D representation of 1D ribs in bridge deck

Table 5.1.2: Properties centroidal ribs

Element	**Properties**	**Cross section**
T-girder, 250 mm deck	• $A = 760\ 640\ mm^2$ • $I_Y = 1{,}878*10^{11}\ mm^4$ • $I_Z = 4{,}674*10^{10}\ mm^4$ • $d_y = 0\ mm$ • $d_z = -19\ mm$ • $I_t = 1{,}869*10^{10}\ mm^4$ • $I_w = 1{,}343*10^{16}\ mm^4$	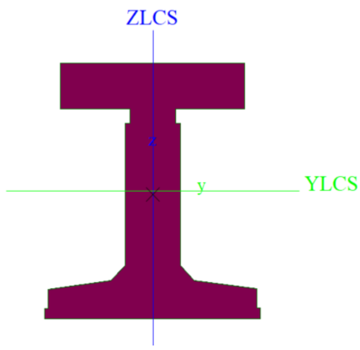
T-girder, 200 mm deck	• $A = 710\ 30\ mm^2$ • $I_Y = 1{,}633*10^{11}\ mm^4$ • $I_Z = 4{,}248*10^{10}\ mm^4$ • $d_y = 0\ mm$ • $d_z = -39\ mm$ • $I_t = 1{,}620*10^{10}\ mm^4$ • $I_w = 1{,}130*10^{16}\ mm^4$	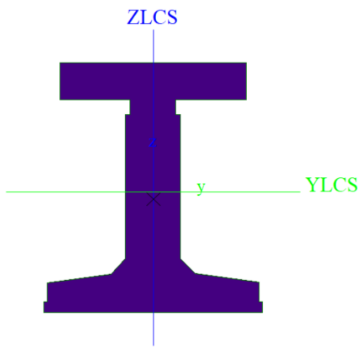
End cross girders	• $A = 850\ 000\ mm^2$ • $I_Y = 7{,}083*10^{10}\ mm^4$ • $I_Z = 5{,}118*10^{10}\ mm^4$ • $d_y = 0\ mm$ • $d_z = 0\ mm$ • $I_t = 1{,}004*10^{11}\ mm^4$ • $I_w = 1{,}893*10^{14}\ mm^4$	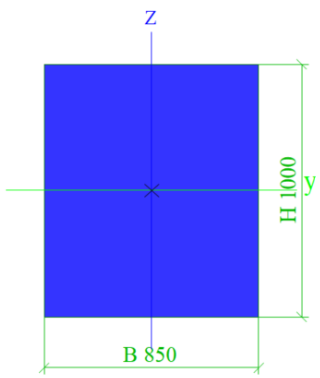
Edge girders	• $A = 480\ 000\ mm^2$ • $I_Y = 5{,}760*10^{10}\ mm^4$ • $I_Z = 6{,}400*10^{9}\ mm^4$ • $d_y = 0\ mm$ • $d_z = 0\ mm$ • $I_t = 2{,}023*10^{10}\ mm^4$ • $I_w = 4{,}888*10^{14}\ mm^4$	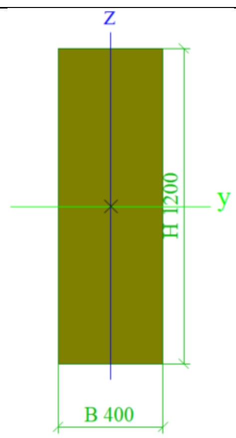

5.1.3 Numerical model completion: mesh details and plate theory

The chosen mesh sizes for the model are 100 mm for 1D elements (ribs) and 100 x 100 mm for 2D elements (shell). This mesh size was selected through an iterative process, where the mesh size was progressively refined until relatively smooth displacement fields were obtained. For the 2D elements, quadrangles were used. Triangular elements were avoided because they can cause high concentrations of loads at a point. The traffic loading in the model is included as described in Section 4.4.4 to obtain the maximum moment and the maximum shear force in transverse direction. Self-weight is excluded in this model to focus solely on the effect of changing stiffness due to variations in rebar type and slab thickness. Validation of the model can be found in APPENDIX B.

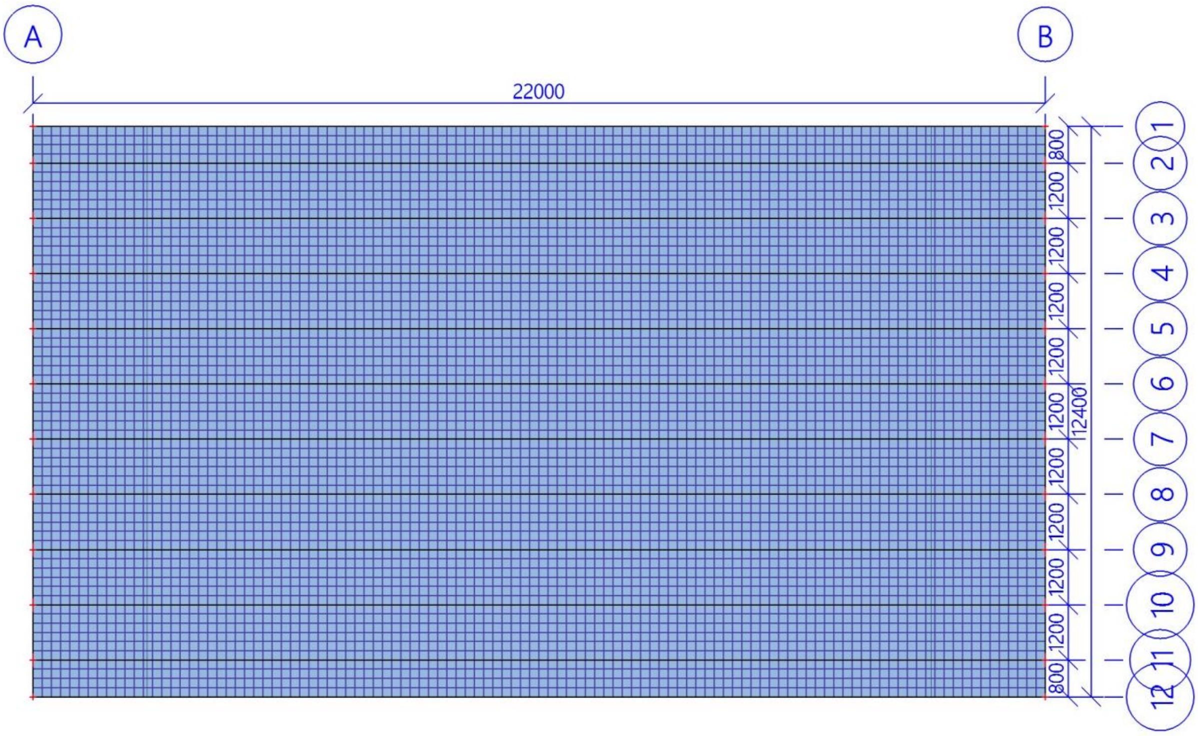

Figure 5.1.3.1: Meshed numerical model

Mindlin theory

In plate analysis, two theoretical models are predominantly used: Kirchhoff theory and Mindlin theory, also known as Reissner-Mindlin theory.

Kirchhoff theory is a suitable method for relatively thin plates where shear deformation can be neglected. This approach considers two degrees of freedom: deflection(w) and normal-to-edge rotation(ϕ_n). Similar to the Euler-Bernoulli beam theory, rotations in Kirchhoff theory are dependent on the deflection of the element. In other words, cross-sections are assumed to remain perpendicular to the vertical centreline of the plate.

Now only two edge loads can be applied, f in the direction of w, and t_n in the direction of ϕ_n. Yet, in general all three plate quantities v_n, m_{nn} and m_{ns} can occur at the edge and may be non-zero. This is summarized in Equation (15.2) (Blaauwendraad, 2010).

$$\begin{Bmatrix} w \\ \varphi_n \end{Bmatrix} \rightarrow \begin{Bmatrix} f \\ t_n \end{Bmatrix} = \begin{Bmatrix} v_n + \dfrac{\partial m_{sn}}{\partial s} \\ m_{nn} \end{Bmatrix} \rightarrow \begin{matrix} v_n \neq f;\ m_{ns} \neq 0 \\ m_{nn} = 0 \end{matrix} \qquad (15.2)$$

Figure 5.1.3.2: Kirchhoff equations (Blaauwendraad, 2010)

Mindlin theory is recommended for relatively thick plates where shear deformation must be taken into account. This theory incorporates three degrees of freedom: deflection(w), normal-to-edge rotation(ϕ_n), and in-plane rotations (ϕ_s). Similar to Timoshenko beam theory, Mindlin theory does not assume that cross-sections remain perpendicular to the vertical centreline of the plate (Blaauwendraad, 2010).
Thus, three edge load components arise: a force f in the direction of w , a distributed torque, t_n, in the direction of ϕ_n, and a distributed torque ,t_s , in the direction of ϕ_s. These edge loads correspond directly to the shear force v_n, the bending moment m_{nn}, and the twisting moment m_{ns} , respectively. Typically, t_n and t_s are zero, which implies that both the bending moment m_{nn} and the twisting moment m_{ns} are zero. This is summarized in Equation (15.1) (Blaauwendraad, 2010).

$$\begin{Bmatrix} w \\ \varphi_n \\ \varphi_s \end{Bmatrix} \rightarrow \begin{Bmatrix} f \\ t_n \\ t_s \end{Bmatrix} = \begin{Bmatrix} v_n \\ m_{nn} \\ m_{ns} \end{Bmatrix} \rightarrow \begin{matrix} v_n = f \\ m_{nn} = 0 \\ m_{ns} = 0 \end{matrix} \qquad (15.1)$$

Figure 5.1.3.3: Mindlin equations (Blaauwendraad, 2010)

A visual representation of the Kirchhoff and Mindlin theories is shown in Figure 5.1.3.4:

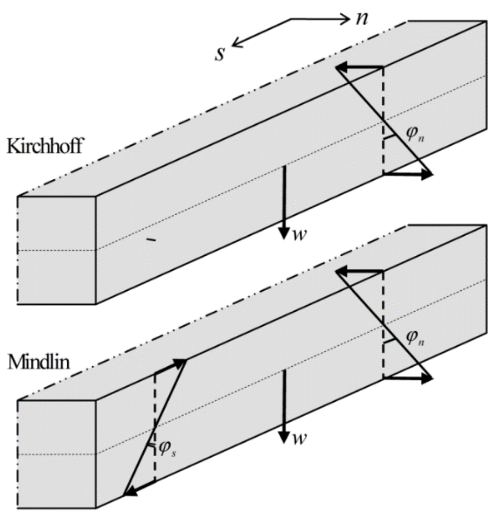

Figure 5.1.3.4: Different boundary conditions for Kirchoff and Mindlin (Blaauwendraad, 2010)

For the numerical model, the cast-in-situ concrete bridge deck is modeled according to Mindlin Theory. The plate is relatively thick, and therefore, it is assumed that shear deformations, which are significant in thicker plates, have to be taken into account. This makes it more accurate than Kirchhoff theory for this application.

5.2 Deflection results and analysis of numerical model and design variation comparison

As shown in Figure 5.2.1, the deflection under the maximum load case for the transverse direction of the bridge deck is highest at the centre of the bridge. This is expected, as the maximum traffic load is also applied at this location (see Section 4.4.4. for the critical load case in the transverse direction). Furthermore, it can be observed that the deflection decreases towards the sides and ends of the deck. At the ends, the deflection even reduces to 0 mm due to the presence of supports with very stiff end cross-girders.

The maximum deflection in bridges in the Netherlands is evaluated according to the Richtlijnen Ontwerp Kunstwerken(ROK) by Rijkswaterstaat. For concrete road bridges, to prevent vibration discomfort, the elastic deflection due to the frequent value of the traffic load must satisfy: $U_{el} \leq L / 1000$ for $L \leq 3$ m and $U_{el} \leq L / 300$ for $L > 10$ m. For the bridge in this case study, with a length of 22 m, this means $U_{el} \leq 73$ mm.

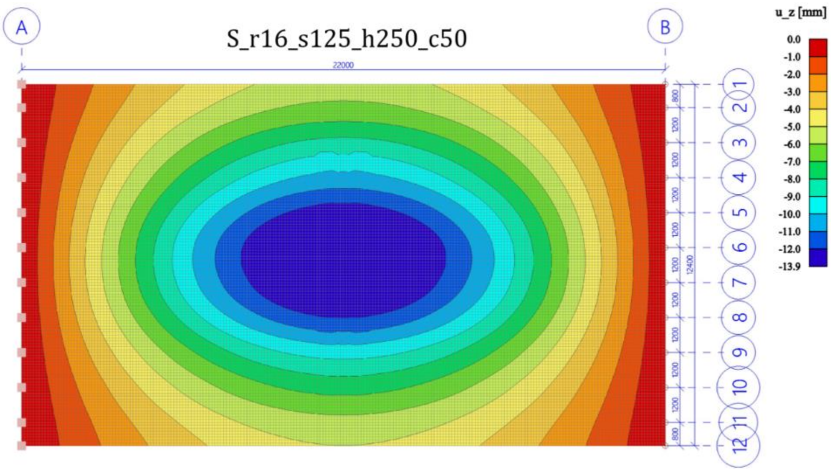

Figure 5.2.1: Displacement field bridge deck for maximum loading transverse direction

Table 5.2.1: Maximum deflections

Variant	$u_{z,max\ slab}$	$u_{z,max,girder}$	$u_{z,maxROK}$
S-r16-s125-h250-c50	13,9 mm	13,9 mm	73 mm
B-r16-s125-h250-c50	14,9 mm	14,4 mm	73 mm
B-r16-s125-h250-c25	14,6 mm	14,4 mm	73 mm
B-r16-s125-h200-c25	17,0 mm	16,4 mm	73 mm
B-r20-s100-h200-c25	16,4 mm	16,3 mm	73 mm

In Table 5.2.1, it can be observed that the lowest deflections occur in the steel variant, with no difference between deflection of the girder and the slab. This indicates that, relative to the T-girder, the slab exhibits negligible deflection. For the variants with BFRP, the deflection is higher than that of the steel variant, and the deflection of the slab is also higher than that of the T-girder. In cases where BFRP rebars are modeled, the bridge deck also exhibits deflection relative to the T-girders.

The highest deflections are found in the variant B-r16-s125-h200-c25, where the height is reduced by reducing the concrete cover while the amount of reinforcement remains constant. For the variants B-r16-s125-h250-c25 and B-r20-s100-h200-c25, where the effective depth and the amount of reinforcement are increased respectively, the deflection is less.

5.3 Transverse bending moment results and analysis of numerical model and design variation comparison

The mechanical model of the bridge deck in the transverse direction can be considered as a beam on elastic supports, where the underlying inverted T-girders represent the “springs”. Towards the middle of the span, the elastic supports will have relatively low stiffness, while towards the end cross-girders, the underlying T-girders will behave more like fixed supports. Therefore, the actual outcome of the model will always lie between these extremes: from a beam on two supports to a continuous beam on fixed supports.

The figures below illustrates the distribution of transverse bending moments under the critical load as described in Section 4.4.4. The wheel load is positioned longitudinally at mid-span and transversely in the middle of the bridge deck between two inverted T-girders. It is clearly visible that the largest span moments occur at the locations of the wheel loads. The further away from the wheel loads, the lower the transverse bending moment. Additionally, it is noted that the effect of a wheel load on adjacent spans is very limited. The transverse bending moment is almost entirely transferred from the bridge deck to the two T-girders between which the wheel load is applied. Consequently, a downward moment is generated in the span, while a hogging moment occurs at the locations of the T-girders.
When considering a section towards the end of the bridge, it is observed that the elastic behavior of the T-girders diminishes. In this case, the T-girders function more as fixed supports rather than elastic supports, as is more the case at mid-span of the bridge.

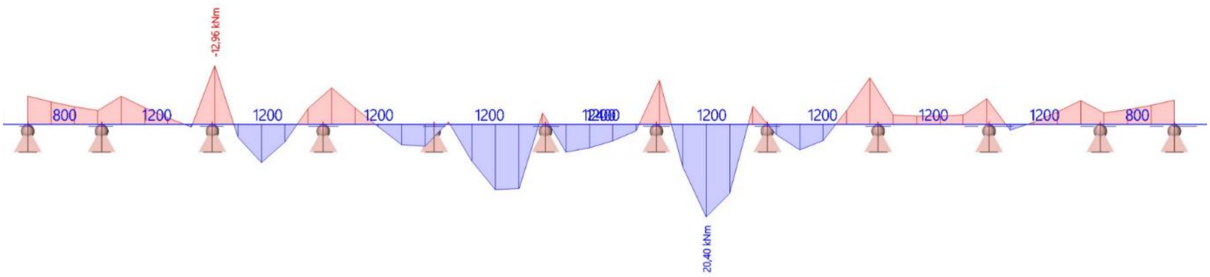

Figure 5.3.2: Transverse bending moment line on mid-section

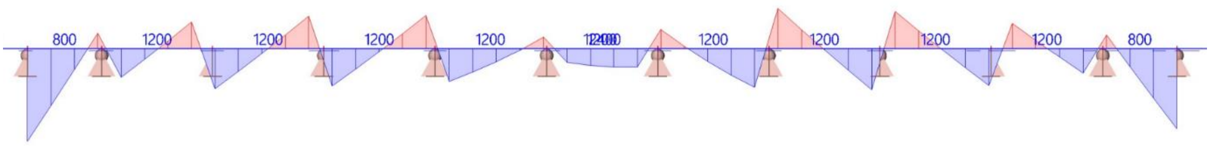

Figure 5.3.3: Transverse bending moment line near end-section

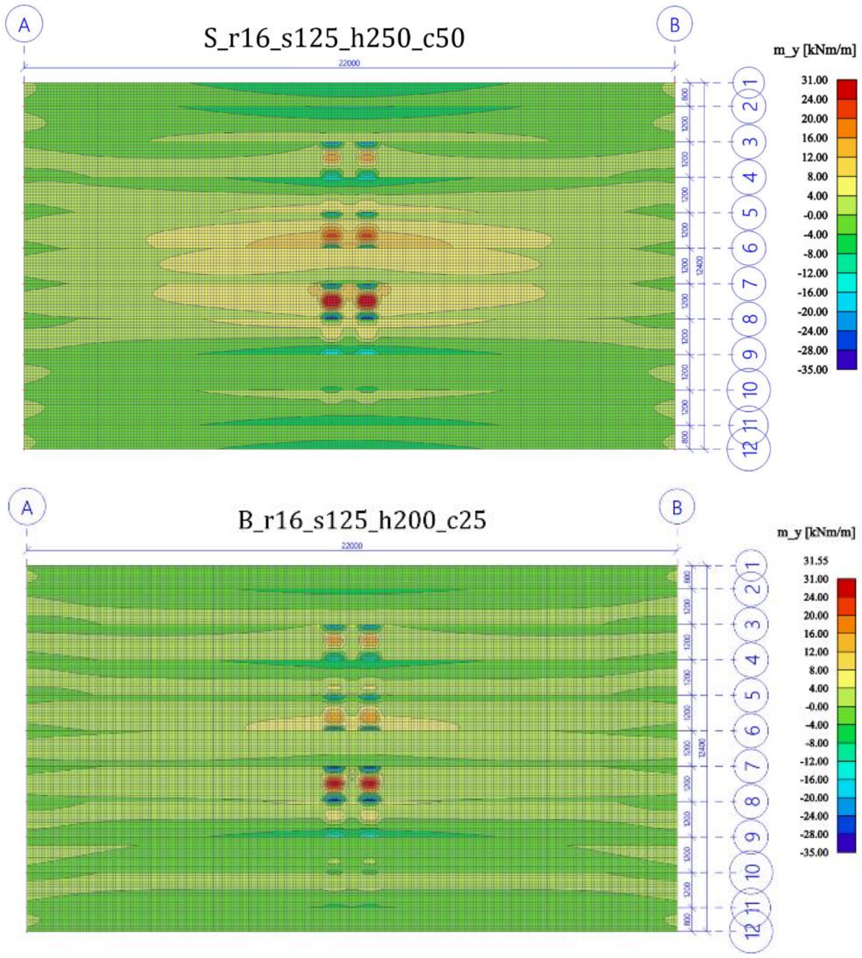

Figure 5.3.1: Transverse bending moments in bridge decks

The contour plots of the transverse bending moments can all be found in APPENDIX C. The steel reference variant and the variant with the same amount of BFRP but with a lower bridge deck cross-section are presented above to illustrate the difference in moment distribution. The steel variant, due to its higher modulus of elasticity, behaves more stiffly and thus has a better distribution of moments, as shown in Figure 5.3.1. In the steel variant, the transverse bending moments spread further along the longitudinal direction of the bridge, in contrast to the BFRP variant with reduced height. The latter transfers the moments over a significantly smaller area, from the center of the bridge deck towards the inverted T-girders. As you can see in Figure 5.3.1 the transverse bending moments of the BFRP deck, are distributed over a length in the longitudinal direction which is about 50% of that of the steel variant. Additionally, the distribution of the load across other beams is less significant in the BFRP variants. Consequently, the most heavily loaded T-beam in the BFRP variants experiences a load approximately 5% higher than that of the most heavily loaded T-beam in the steel variant.

Table 5.3.1: Maximum transverse bending moments

Variant	$M_{Ek,trans}$ (hog – span)	$M_{Rd,trans}$
S-r16-s125-h250-c50	31,1 kNm/m – 30,2 kNm/m	120 kNm/m
B-r16-s125-h250-c50	34,6 kNm/m – 25,9 kNm/m	121 kNm/m
B-r16-s125-h250-c25	34,0 kNm/m – 26,7 kNm/m	138 kNm/m
B-r16-s125-h200-c25	34,8 kNm/m – 25,7 kNm/m	103 kNm/m
B-r20-s100-h200-c25	33,9 kNm/m – 26,8 kNm/m	107 kNm/m

As shown in Table 5.3.1, there is a significant decrease in the maximum transverse bending moment in the span when BFRP reinforcement is used. Additionally, the use of BFRP reinforcement results in a significant increase in the maximum hogging moment in the bridge deck above the T-girders. When the height of the bridge deck is reduced, as in variants B-r16-s125-h200-c25 and B-r20-s100-h200-c25, it is again observed that the hogging moment further increases, while the span moment shows a less significant difference.
Furthermore, it is noteworthy that the bending moment capacity, M_{Rd}, does not significantly increase with a doubling of the reinforcement percentage. This is because, at this value, the condition $x_u/d < 1.3k_{x\_max}$ from BRL0513 changes. Due to the high reinforcement percentage, the capacity is dependent on the failure of the concrete in compression rather than the failure of the reinforcement.

5.4 Transverse shear results and analysis of numerical model and design variation comparison

The distribution of transverse shear force in the bridge deck is illustrated in Figure 5.4.1. The loading case is in accordance with Section 4.4.5. The maximum transverse shear force is observed in the region around the wheel loads. This effect is highly concentrated around the wheel loads and spreads very limited in the x-direction.
The transverse shear force increases from the wheel load towards the T-girders. Subsequently, this shear force is absorbed by the T-girders. Figure 5.4.1 clearly shows that the influence on adjacent spans is negligible. The transverse shear force "disappears" into the T-girder.

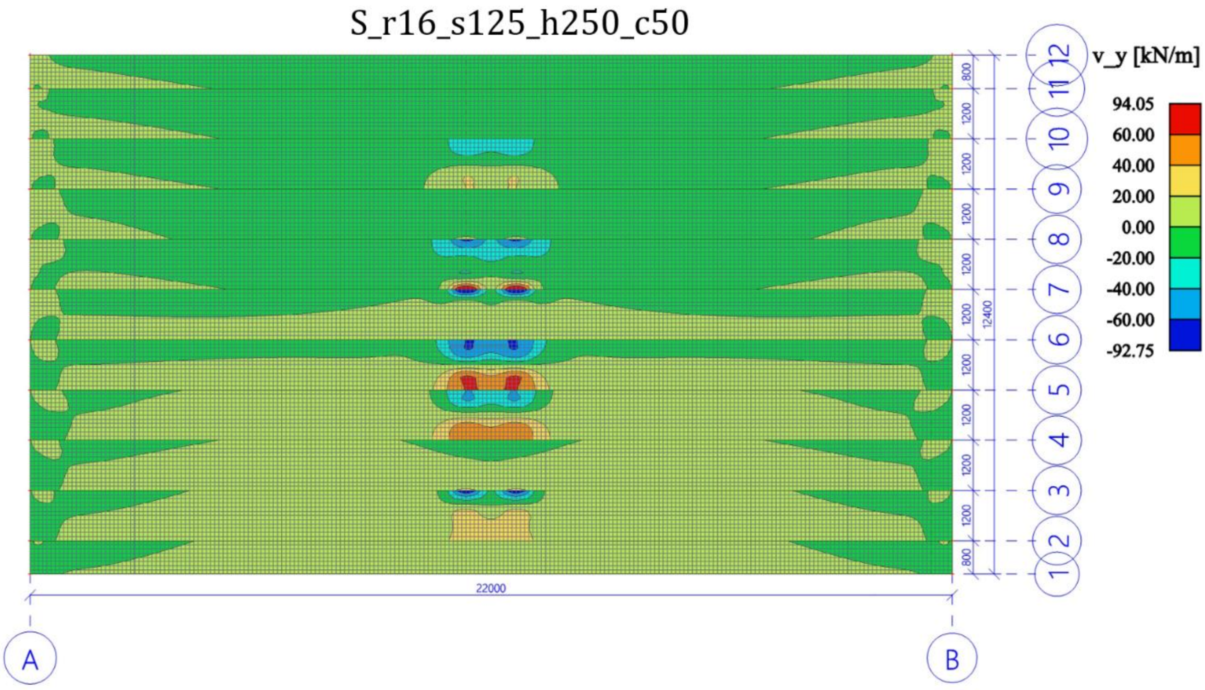

Figure 5.4.1: Maximum transverse shear force in bridge deck

For the maximum transverse shear force, both Load Model 1 and Load Model 2 were analyzed. The results are presented below:

Table 5.4.1: Maximum transverse shear forces, LM1 and LM2

Variant	0,5d	$V_{Ek,trans\ 0,5d,LM1}$	$V_{Ek,trans\ 0,5d,LM2}$	$V_{Rd,trans}$
S-r16-s125-h250-c50	96 mm	56 kN/m	54 kN/m	135 kN/m
B-r16-s125-h250-c50	96 mm	55 kN/m	53 kN/m	104 kN/m
B-r16-s125-h250-c25	109 mm	53 kN/m	49 kN/m	114 kN/m
B-r16-s125-h200-c25	84 mm	59 kN/m	56 kN/m	91 kN/m
B-r20-s100-h200-c25	83 mm	59 kN/m	56 kN/m	97 kN/m

The results indicate that Load Model 1 provides the critical load for transverse shear force in the bridge deck. Additionally, it is observed that the distribution of shear force from the wheel loads does not show a significant difference between the amount or type of reinforcement. However, there is a noticeable effect on the shear force distribution due to the difference in effective depth, d. A greater effective depth results in a reduction of the transverse shear force, while a reduction in effective depth leads to an increase in the transverse shear force

When comparing the steel reference variant, S-r16-s125-h250-c50, with the most sustainable and therefore most desirable BFRP variant, B-r16-s125-h200-c25, it is observed that the latter experiences an increase in transverse shear effect by more than 5%, while its capacity decreases by approximately 30%. This indicates that transverse shear is more governing for this variant compared to its steel reference variant. Doubling the amount of reinforcement has no effect on the transverse shear effect since the effective depth remains nearly the same. However, it does lead to an increase in transverse shear capacity.

To further illustrate the difference in the effect of shear force, a closer examination of the shear force distribution of the critical traffic load configuration will be conducted. By means of the contour plots generated in SCIA Engineer

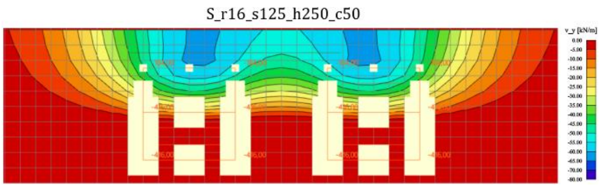

Figure 5.4.2: V_{trans} S_r16_s125_h250_c50

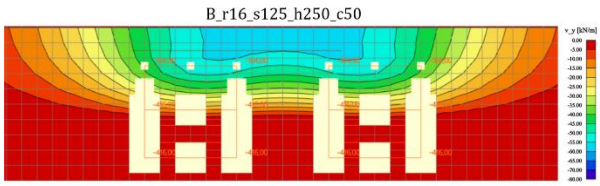

Figure 5.4.3: V_{trans} B_r16_s125_h250_c50

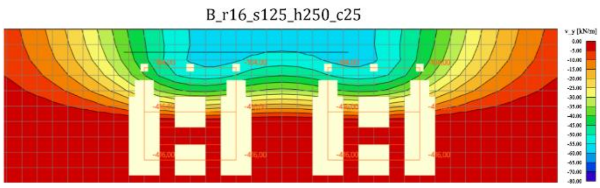

Figure 5.4.4: V_{trans} B_r16_s125_h250_c25

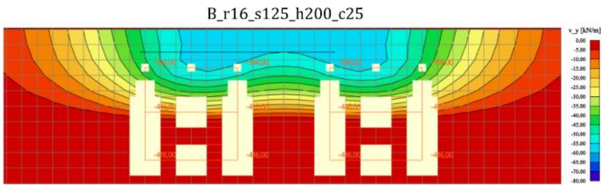

Figure 5.4.5: V_{trans} B_r16_s125_h200_c25

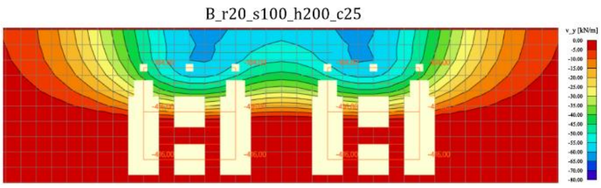

Figure 5.4.6: V_{trans} B_r20_s100_h200_c25

The obtained contour plots clearly illustrate how the wheel loads are transferred towards the inverted T-girders. In the steel variant and the BFRP variant with double the amount of reinforcement, it is evident that the influence of the two individual wheel loads is more pronounced in the character of the contour plot. The other three variants, with relatively lower effective stiffness, show that the effect of the two wheel loads merges more seamlessly

5.5 Summary and conclusion

A quasi-linear model was developed using the finite element software SCIA Engineer. The model represents an in-situ cast bridge deck on prefabricated inverted T-girders. In the model, the bridge deck is modeled as an orthotropic 2D plate with centric ribs representing the girders. In the longitudinal direction, it is assumed that the orthotropic plate is uncracked, resulting in higher stiffness compared to the transverse direction. Additionally, the effective stiffness has been adjusted for the different types of reinforcement, reinforcement ratios, and effective depths.

The model has shown that when reinforced with BFRP instead of steel, the transverse bending moments in the bridge deck span between the T-girders decrease by 15%. This is because the lower modulus of elasticity of BFRP offers less resistance to deflection, thereby reducing the bending moments. Additionally, it is observed that the deflections of the concrete bridge deck relative to the T-girders are higher in the BFRP variants.

For the hogging moments, the opposite effect was observed. The hogging moments in the steel-reinforced variants are 10% lower than in the BFRP-reinforced variants. The steel variant is better able to distribute the transverse bending moments in the bridge deck more evenly towards the T-girders due to its higher stiffness. The BFRP-reinforced bridge decks transfer the transverse bending moments over a smaller bridge deck area towards the T-girders. The heaviest loaded T-girder in the BFRP reinforced bridge decks, gets 5% more loading compared to the heaviest loaded T-girder in the steel reinforced bridge deck. This is also due to the better load distribution of the steel reinforced deck over the girders.

The model has demonstrated that the transverse shear distribution in the bridge deck is primarily dependent on the effective depth of the cross-section. For the considered design BFRP variants, this means that an increase of up to 5% in transverse shear may occur, due to less distribution of the loading. A greater effective depth results in the wheel load being distributed over a larger area. This phenomenon is consistent with literature. For instance, Grasser & Thielen (1991) defined the effective width used in German practice for simply supported one-way slabs as a function of, among other factors, the effective depth. Other parameters influencing the effective width include the width of the loaded area and the center-to-center distance between load and support.

The contour plots also revealed that when the stiffness is relatively high, as seen in the cases of the steel variant and the BFRP variant with double the reinforcement percentage, peak values in transverse shear occur at the centers of the wheel loads. In the more flexible reinforced variants, this effect of the individual wheel loads is less pronounced, and the wheel load effects tend to merge more seamlessly.

6. Design variants failure mechanisms and optimization

Chapter 5 provided valuable insights into the effects of BFRP reinforcement and a reduced concrete cover on the load distributions in a concrete bridge deck. In chapter 7, the various alternatives will be evaluated based on their environmental cost to estimate the sustainability benefits achieved compared to traditional steel-reinforced bridge decks. Before calculating the actual Environmental Cost Indicator (ECI), this chapter will attempt to further optimize the current alternatives to ensure a fair comparison regarding their environmental impact. The designs will be optimized for fatigue, crack width, shear force, and bending moment.

6.1 Fatigue analysis of design variants

Fatigue traffic loading

For the fatigue check, the relatively simple and conservative load model LM1 from NEN-EN 1991, Section 4.6.2, was chosen. The traffic load configuration is the same as the characteristic Load Model 1, established in Section 4.4.4, where the axle loads are $0{,}7Q_{ik}$ and for the UDL load $0{,}3q_{ik}$. This traffic load was input into the numerical software model of SCIA Engineer to obtain the bending moments associated with the fatigue checks."

Steel fatigue check according to NEN-EN 1992-1-1 par. 6.8

The maximum allowable stress range for steel can be calculated using NEN-EN 1992-1-1. The number of cycles assumed for the fatigue check is 2 million heavy vehicles per year. Over a lifespan of 100 years, this results in a total of 200 million cycles. As described in Section 3.6 of this report, this yields a maximum allowable stress range in the reinforcement of 77 N/mm²

BFRP fatigue check according to El-Ragaby et.al (2007)

Currently, there are no specific fatigue design standards available for BFRP. Nonetheless, El-Ragaby et al. (2007) conducted experimental research on the fatigue life of BFRP and established a relationship between fatigue life and loading cycles. This was previously substantiated in Section 3.6 of this report. For 200 million cycles, the maximum allowable stress range in the reinforcement for BFRP is 388 N/mm².

$$\Delta\sigma = \frac{\frac{M_{fat}}{A_s}}{d - \frac{x}{3}}$$

Table 6.1: Fatigue analysis result design variants

Variant	M_{fat}	$\Delta\sigma$	$\Delta\sigma_{RsK}$	Unity check
S-r16-s125-h250-c50	20,0 kNm/m	71 N/mm^2	77 N/mm^2	0,92
B-r16-s125-h250-c50	23,4 kNm/m	80 N/mm^2	388 N/mm^2	0,21
B-r16-s125-h250-c25	23,0 kNm/m	69 N/mm^2	388 N/mm^2	0,18
B-r16-s125-h200-c25	23,6 kNm/m	93 N/mm^2	388 N/mm^2	0,24
B-r20-s100-h200-c25	23,0 kNm/m	48 N/mm^2	388 N/mm^2	0,12

6.2 Crack width analysis of design variants

The crack width of a structure must be analysed to ensure its durability and functionality. The primary reason for limiting crack width is to prevent water, salts, chlorides, and other chemicals from penetrating the reinforcement, which could lead to corrosion. This concern does not apply to BFRP, as this type of rebar cannot corrode. Nevertheless, various design codes, including BRL0513, specify a maximum allowable crack width based on aesthetics and watertightness of a structure. For the application of BFRP in a bridge deck of an inverted T-girder bridge, the crack width requirement is considered entirely irrelevant. Aesthetics are not a concern since the underside of the bridge deck is not visible due to the T-girders beneath it. On the upper side, an asphalt layer will cover the bridge deck, making any cracks invisible. Additionally, this application of BFRP will not need to retain large volumes of water, making the watertightness of the structure irrelevant.
Therefore, only the design variant with steel reinforcement will be evaluated for crack width.

Crack width check according to NEN 1992-1-1 par. 7.3.4
The steel variant has been checked for crack width in accordance with paragraph 7.3.4 of NEN-EN 1992-1-1. The crack width can be calculated using the provided formulas, where the characteristic value of the traffic load is used for the load. Other important input parameters include the reinforcement ratio, rebar properties, and concrete cross sectional properties.

$$w_k = s_{r,max} * (\varepsilon_{sm} - \varepsilon_{cm})$$

$$\varepsilon_{sm} - \varepsilon_{cm} = \frac{\sigma_s - k_t * f_{ct,eff} * \frac{\left(1 + \alpha_e * \rho_{p,eff}\right)}{\rho_{p,eff}}}{E_s} \geq 0{,}6\frac{\sigma_s}{E_s}$$

Table 6.2: Crack width analysis result reference design variants

Variant	M_{kar}	w_k	w_{max}	Unity check
S-r16-s125-h250-c50	31,1 kNm/m	0,08 mm	0,20 mm	0,41

6.3 Transverse bending moment analysis of design variants

The transverse bending moments obtained from the quasi-linear model in Section 5.3 are derived solely from the characteristic traffic loads. To evaluate the transverse bending moment capacity of the design variants of the bridge deck, it is first necessary to determine the design values of the occurring transverse bending moments. These design values are obtained by incorporating the self-weight and permanent loads of the bridge deck along with the corresponding load factors. The case study in this report has been assessed for CC3 situations in accordance with NEN-EN 1990.

Table 6.3: Transverse bending moment analysis result design variants

Variant	M_{Ed}	M_{Rd}	Unity check
S-r16-s125-h250-c50	48,9 kNm/m	120 kNm/m	0,41
B-r16-s125-h250-c50	54,1 kNm/m	121 kNm/m	0,45
B-r16-s125-h250-c25	53,3 kNm/m	138 kNm/m	0,36
B-r16-s125-h200-c25	54,5 kNm/m	103 kNm/m	0,53
B-r20-s100-h200-c25	53,1 kNm/m	107 kNm/m	0,50

6.4 Transverse shear force analysis of design variants

For the transverse shear force assessment in the bridge deck, like the bending moments, the design values of the loads in the governing load configuration must be considered. Therefore, the characteristic values from the quasi-linear model have been supplemented with self-weight, permanent loads, and the load factors corresponding to a CC3 consequence class, in accordance with NEN-EN 1990.

Table 6.4: Transverse shear force analysis result design variants

Variant	V_{Ed}	V_{Rd}	Unity check
S-r16-s125-h250-c50	91 kN/m	135 kN/m	0,67
B-r16-s125-h250-c50	90 kN/m	104 kN/m	0,87
B-r16-s125-h250-c25	87 kN/m	114 kN/m	0,76
B-r16-s125-h200-c25	96 kN/m	91 kN/m	1,05
B-r20-s100-h200-c25	96 kN/m	97 kN/m	0,99

6.5 Optimized design alternative

For the initially selected variants, it was found that the B-r16-s125-h200-c25 variant did not meet the shear capacity requirements, with a unity check greater than 1, using the applied method. Since this variant would yield the highest sustainability benefits by maintaining the same amount of reinforcement while reducing the amount of concrete, an optimization of this variant was executed to meet the shear force requirements. Through an iterative process, a new variant was developed that achieved the optimal balance between reducing concrete usage and maintaining structural performance. The structural performance for this optimized variant, B-r16-s125-h215-c25, is provided below.

Table 6.5.1: Fatigue analysis result design variants

Variant	M_{fat}	$\Delta\sigma$	$\Delta\sigma_{RsK}$	Unity check
B-r16-s125-h215-c25	23,5 kNm/m	85 N/mm^2	388 N/mm^2	0,22

Table 6.5.2.: Transverse bending moment analysis result optimized variant

Variant	M_{Ed}	M_{Rd}	Unity check
B-r16-s125-h215-c25	54,3 kNm/m	114 kNm/m	0,48

Table 6.5.3.: Transverse shear force analysis result optimized variant

Variant	V_{Ed}	V_{Rd}	Unity check
B-r16-s125-h215-c25	92 kN/m	99 kN/m	0,93

6.6 Summary and conclusion

This chapter has demonstrated that the critical failure mechanism is indeed different for BFRP-reinforced bridge decks compared to steel-reinforced bridge decks. In the bridge deck reinforced with steel rebar, the fatigue requirement is critical, with a unity check of 0,92. Fatigue unity checks for BFRP indicate that fatigue is not an issue for this rebar material in a bridge deck, unlike steel rebar. This is consistent with El-Ragaby et al. (2007), who also state that the fatigue life of FRP is significantly higher than that of steel.

Crack width and transverse bending moment do not appear to be the critical failure mechanisms for any of the design variants. However, transverse shear force is indeed the critical failure mechanism for the BFRP variants. This is consistent with the simplified preliminary analysis presented in Chapter 3, where one-way shear was also identified as the most likely governing failure mechanism. As shown in Table 6.4, using BFRP as a one-to-one replacement for steel is feasible, as the UC still provides a sufficient safety margin. Nonetheless, it should be noted that a one-to-one replacement of steel with BFRP, combined with reducing the height of the bridge deck, results in a UC greater than 1. Reducing the construction height of the bridge deck while doubling the amount of BFRP yields a UC of 0,99, which is just sufficient but offers a very small safety margin.

The calculated shear capacity is based on BRL 0513, which is an extension to NEN-EN 1992. The most desired sustainable design variant for the bridge deck, B-r16-s125-h200-c25, does not meet the shear force requirement, having a UC higher than 1. Therefore, an optimization of the construction height of the concrete bridge deck was carried out to achieve maximum sustainability while still meeting structural performance requirements. As a result, the variant with a height of 215 mm, designated as B-r16-s125-h215-c25, emerged as the optimized variant, having a governing UC of 0,93 for transverse shear force.

Additionally, a more advanced calculation based on nonlinearity, more extensive geometries or compressive membrane action should provide extra capacity, as demonstrated in the reference project on the Thompson Bridge in Section 2.1.7 (Zhou, Zheng, & Taylor, 2018). Which could potentially lead to even better optimizations.

7. Environmental cost analysis

In addition to their mechanical properties, the design variants each have their unique sustainability characteristics. This chapter will compare the different variants based on their environmental impact. To determine the Environmental Cost Indicator (ECI) of each design variant, the system boundaries of the LCA study must first be established. Subsequently, using the Environmental Product Declaration (EPD) of BFRP, the ECI of the material will be calculated to ultimately derive the ECI values for the entire design variants.

7.1 LCA study and system boundaries

A Life Cycle Assessment (LCA) can encompass various system boundaries. For this study, the cradle-to-gate (A1-A3) system boundaries have been selected. This includes the environmental impacts from raw material extraction (A1), transportation to the manufacturer (A2), and manufacturing of the product (A3). Detailed and reliable data for the use phase (B) and end-of-life phase (C) can be difficult to obtain. Focusing on A1-A3 ensures that the analysis is based on more readily available and accurate data. This approach also places a primary focus on material usage. The use phase (B) and end-of-life phase (C) are more project-specific parameters.

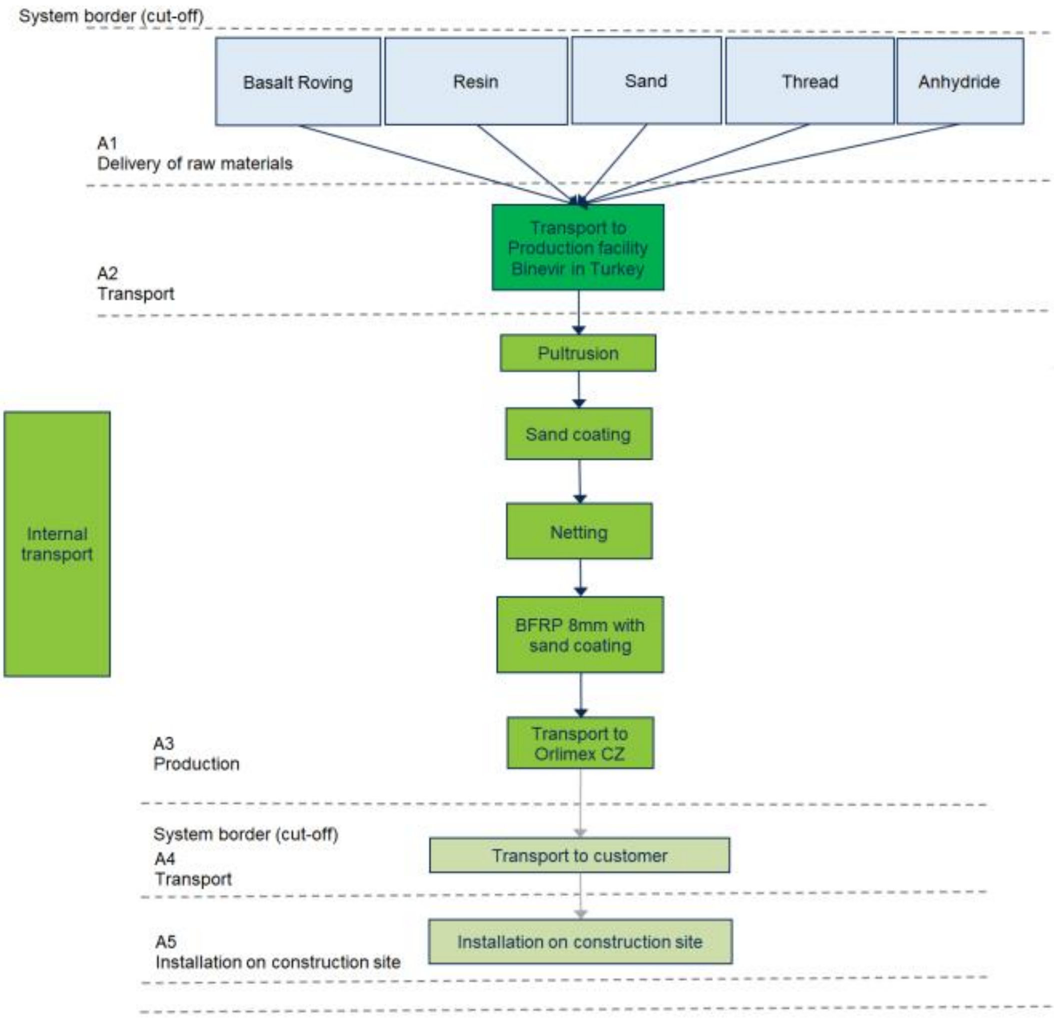

Figure 7.1: LCA process diagram according to EN 15804 (7.2.1) (Orlimex CZ s.r.o., 2022)

7.2 Environmental product declaration current approach

The Environmental Product Declaration (EPD) is a document that quantifies the environmental impact of a construction material based on various impact categories. Every supplier of construction materials is required to provide an EPD for their materials. Although the supplier is responsible for the EPD, the documents must be independently verified by a third party to guarantee the reliability of the EPD.
The EPD must be conducted in accordance with ISO 14025 and NEN-EN 15804+A1. An updated version of the latter will become the standard by the end of 2025. For this analysis, the current standard has been used, as this ensures that the ECI aligns with the current situation and facilitates easier comparison with other reference projects. The EPD used in this study is provided by Orlimex CZ, a major player in the BFRP supply market in the Netherlands, which also supplied the BFRP for the reference project discussed in Section 2.1.7 on the Bus Depot in Breda. Additionally, the values for reinforcing steel are provided, which come from the Vereniging Wapeningsstaal Nederland (Dutch Association for Reinforcing Steel).

Environmental impact categories:

ADPE	Abiotic Depletion Potential for non-fossil resources
ADPF	Abiotic Depletion Potential for fossil resources
GWP	Global Warming Potential
ODP	Depletion Potential of the stratospheric Ozone layer
POCP	Formation potential of tropospheric ozone photochemical oxidants
AP	Acidification Potential of land and water
EP	Eutrophication Potential
HTP	Human Toxicity Potential
FAETP	Freshwater Aquatic Ecotoxicity Potential
MAETP	Marine Aquatic Ecotoxicity Potential
TETP	Terrestrial Ecotoxicity Potential

Table 7.2: Impact category values of BFRP and steel rebar per kg according to NEN-EN 15804+A1 (Orlimex CZ s.r.o., 2022) (Vereniging Wapeningsstaal Nederland, 2021)

Environmental impact category	Unit	BFRP	Steel
ADPE	kg Sb. eq.	2,14E-5	9,66E-6
ADPF	kg Sb. eq.	2,18E-2	7,50E-3
GWP	kg CO_2 eq.	2,69E+0	9,92E-1
ODP	kg CFC 11 eq.	2,85E-7	8,87E-8
POCP	kg ethene eq.	1,40E-3	1,03E-3
AP	kg SO_2 eq.	9,96E-3	4,62E-3
EP	kg PO_4^{-3} eq.	1,45E-3	6,42E-4
HTP	kg DCB eq.	1,23E+0	6,24E-1
FAETP	kg DCB eq.	1,63E-1	2,19E-2
MAETP	kg DCB eq.	8,13E+1	4,21E+1
TETP	kg DCP eq.	6,28E-3	6,01E-2

7.3 Environmental cost indicator current approach

The Environmental Cost Indicator (ECI) represents the shadow costs of the environmental impact of construction materials, expressed in a monetary value. These shadow costs enable the comparison of different materials and designs in terms of their environmental impact. Table 7.3.1 presents the shadow costs of the various impact categories as described according to NEN-EN 15804+A1.

Table 7.3.1: Shadow costs per impact category according to NEN-EN 15804+A1

Environmental impact category	Unit	Shadow costs (€/unit)
ADPE	kg Sb. eq.	€0,16
ADPF	kg Sb. eq.	€0,16
GWP	kg CO_2 eq.	€0,05
ODP	kg CFC 11 eq.	€30,00
POCP	kg ethene eq.	€2,00
AP	kg SO_2 eq.	€4,00
EP	kg PO_4^{-3} eq.	€9,00
HTP	kg DCB eq.	€0,09
FAETP	kg DCB eq.	€0,03
MAETP	kg DCB eq.	€0,0001
TETP	kg DCP eq.	€0,06

The shadow costs of each impact category from Table 7.3.1 must be multiplied by the impact category values of the rebar materials from Table 7.2 to obtain the total shadow costs of the rebar materials. The results of this calculation are presented in Table 7.3.2. The contribution to the total ECI of each environmental impact category can be found in APPENDIX F. It can be observed that the ECI of BFRP per unit of mass is more than twice as high as that of steel. However, it is important to consider that BFRP has a density that is a 3,9 times lower than steel rebar. Therefore, per unit of volume, the ECI of BFRP is significantly lower, as shown in Table 7.3.2.

Table 7.3.2: ECI values BFRP and steel rebar according to NEN-EN 15804+A1

Rebar Material	ECI	ECI
BFRP rebar	€ 0,320 / kg	€ 640,00 / m^3
Steel rebar	€ 0,142 / kg	€ 1114,70 / m^3 (+74%)

7.4 Environmental product declaration forthcoming approach

Although the design variants will be assessed according to the current LCA standard, a forward-looking perspective on the sustainability of BFRP compared to steel in the future is also considered. The new standard, will consist of 19 impact categories instead of the current 11 impact categories. It is anticipated that the new standard will result in the ECI for construction materials being on average 1,4 to 2,1 times higher, depending on the material. Table 7.4 presents the new values of the EPD in accordance with NEN-EN 15804+A2.

Environmental impact categories:

GWP-total	Global Warming Potential - total
GWP-fossil	Global Warming Potential – fossil resources
GWP-biogenic	Global Warming Potential – bio-based resources
GWP-luluc	Global Warming Potential – land use change
ODP	Depletion Potential of the stratospheric Ozone layer
AP	Acidification Potential of land and water
EP-freshwater	Eutrophication Potential – freshwater
EP-marine	Eutrophication Potential – marine ecosystems
EP-terrestrial	Eutrophication Potential – terrestrial ecosystems
POCP	Formation potential of tropospheric ozone photochemical oxidants
ADP-minerals & metals	Abiotic Depletion Potential natural non-fossil resources
ADP-fossil	Abiotic Depletion Potential natural fossil fuel resources
WDP	Water Deprivation Potential
PM	Particulate Matter
IRP	Ionizing Radiation
ETP-fw	Ecotoxicity Potential - freshwater
HTP-c	Human Toxicity Potential - carcinogenic
HTP-nc	Human Toxicity Potential – non-carcinogenic
SQP	Land Use Related Impact

Table 7.4: Impact category values of BFRP and steel rebar per kg according to NEN-EN 15804+A2 (Orlimex CZ s.r.o., 2022) (Vereniging Wapeningsstaal Nederland, 2021)

Environmental impact category	Unit	BFRP	Steel
GWP-total	kg CO_2 eq.	2,76E+00	1,02E+00
GWP-fossil	kg CO_2 eq.	2,75E+00	1,02E+00
GWP-biogenic	kg CO_2 eq.	6,20E-03	3,97E-03
GWP-luluc	kg CO_2 eq.	4,43E-03	1,18E-03
ODP	kg CFC 11 eq.	3,15E-07	9,20E-08
AP	mol H^+ eq.	1,22E-02	5,70E-03
EP-freshwater	kg PO_4^{-3} eq.	1,09E-04	5,32E-05
EP-marine	kg N eq.	2,66E-03	1,23E-03
EP-terrestrial	mol N eq.	2,85E-02	1,35E-02
POCP	kg NMVOC eq.	9,38E-03	4,90E-03
ADP-minerals & metals	kg Sb eq.	2,14E-05	9,66E-06
ADP-fossil	MJ	4,14E+01	1,45E-01
WDP	m^3 world eq.	5,59E-01	5,38E-01
PM	Disease incidence	9,55E-08	1,00E-07
IRP	kBq U235 eq.	1,00E-01	5,98E-02
ETP-fw	CTUe	4,43E+01	2,24E+01
HTP-c	CTUh	1,61E-09	1,05E-08
HTP-nc	CTUh	2,20E-08	2,97E-07
SQP	---	9,94E+00	4,28E+00

7.5 Environmental cost indicator forthcoming approach

The shadow costs for the impact categories have also been revised for the update of the LCA standard. In addition to the newly added impact categories, the weighting factors for the impact categories included in the current standard have been modified. Notably, the environmental costs for CO_2 have more than doubled.

Table 7.5.1: Shadow costs per impact category according to NEN-EN 15804+A2

Environmental impact category	Unit	Shadow costs (€/unit)
GWP-total	kg CO_2 eq.	€ 0,12
GWP-fossil	kg CO_2 eq.	€ 0,12
GWP-biogenic	kg CO_2 eq.	€ 0,12
GWP-luluc	kg CO_2 eq.	€ 0,12
ODP	kg CFC 11 eq.	€ 32,00
AP	mol H^+ eq.	€ 0,39
EP-freshwater	kg PO_4^{-3} eq.	€ 1,96
EP-marine	kg N eq.	€ 3,28
EP-terrestrial	mol N eq.	€ 0,36
POCP	kg NMVOC eq.	€ 1,22
ADP-minerals & metals	kg Sb eq.	€ 0,30
ADP-fossil	MJ	€ 0,00
WDP	m^3 world eq.	€ 0,01
PM	Disease incidence	€ 575.838,00
IRP	kBq U235 eq.	€ 0,05
ETP-fw	CTUe	€ 0,00
HTP-c	CTUh	€ 1.096.368,00
HTP-nc	CTUh	€ 147.588,00
SQP	---	€ 0,00

By multiplying the impact category values with the shadow costs, Table 7.5.2 is obtained. The contribution to the total ECI of each environmental impact category can be found in APPENDIX F. ECI has significantly increased for both materials, which falls within expectations. However, the degree of increase varies considerably. Compared to the current standard, steel shows an ECI increase of 82%, while BFRP shows an increase of only 39%. As a result, when the new standard is implemented, replacing steel with BFRP will have an even greater impact on sustainability. In the current approach, steel has an ECI per unit volume that is 74% higher than BFRP, whereas in the new approach, this difference increases to 128%.

Table 7.5.2: ECI values BFRP and steel rebar according to NEN-EN 15804+A2

Rebar Material	ECI	ECI
BFRP rebar	€ 0,445 / kg	€ 890,00 / m^3
Steel rebar	€ 0,258 / kg	€ 2025,30 / m^3 (+128%)

7.6 ECI values of design variants

With the obtained ECI values of the rebar material, the total ECI value of each design variant can be calculated. The ECI for the variants is calculated based on the current standard, NEN-EN 15804+A1, as this is currently in effect. In addition to the rebar material, the quantity of concrete must also be included in the calculation, as it is a variable parameter in the design variants. For the detailed calculation and methodology, see APPENDIX G of this report.

Table 7.6.1: ECI values of design variants per m^2 bridge deck C30/37 CEM I

Variant	C30/37 CEM I	BFRP	Steel	Total
S-r16-s125-h250-c50	€ 6,06	€ 0	€ 5,27	€ 11,33 (0%)
B-r16-s125-h250-c50	€ 6,06	€ 3,02	€ 0	€ 9,08 (-20%)
B-r16-s125-h250-c25	€ 6,06	€ 3,02	€ 0	€ 9,08 (-20%)
B-r16-s125-h200-c25	€ 4,85	€ 3,02	€ 0	€ 7,87 (-30%)
B-r20-s100-h200-c25	€ 4,85	€ 5,93	€ 0	€ 10,78 (-5%)
B-r16-s125-h215-c25	€ 5,21	€ 3,02	€ 0	€ 8,23 (-27%)

Table 7.6.2: ECI values of design variants per m^2 bridge deck C30/37 CEM III

Variant	C30/37 CEM III	BFRP	Steel	Total
S-r16-s125-h250-c50	€ 3,17	€ 0	€ 5,27	€ 8,44 (0%)
B-r16-s125-h250-c50	€ 3,17	€ 3,02	€ 0	€ 6,19 (-26%)
B-r16-s125-h250-c25	€ 3,17	€ 3,02	€ 0	€ 6,19 (-26%)
B-r16-s125-h200-c25	€ 2,53	€ 3,02	€ 0	€ 5,55 (-34%)
B-r20-s100-h200-c25	€ 2,53	€ 5,93	€ 0	€ 8,59 (+2%)
B-r16-s125-h215-c25	€ 2,72	€ 3,02	€ 0	€ 5,74 (-32%)

7.7 Summary and conclusion

A life cycle assessment (LCA) encompasses various phases in which a product can exist, specifically the product stage (A1-A3), construction stage (A4-A5), use stage (B), end-of-life stage (C), and beyond life cycle stage (D). For determining the Environmental Cost Indicator (ECI) of the design variants, the system boundaries of the LCA were set to include only the product stage (A1-A3).

Using the Environmental Product Declaration (EPD), the value of each environmental impact category per kilogram of rebar material was determined for both reinforcing steel and BFRP. By multiplying the obtained values with the shadow costs per impact category, an ECI value in euros was derived. Per unit of mass, steel has a more favorable ECI than BFRP. However, the density of steel is nearly four times higher than that of BFRP. When considering the ECI per unit of volume, BFRP performs significantly better than steel.

The total ECI values for the design variants were obtained for both the use of concrete with CEM I and CEM III cement. The percentage reduction in ECI ranges between 20-34% for BFRP variants with the same reinforcement quantities. As expected, the greatest sustainability improvement is achieved by applying BFRP reinforcement with a reduction in concrete cover by reducing the amount of concrete. However, the bridge deck with the highest sustainability does not meet the transverse shear requirements according to the calculation methodology. Therefore, an optimization was carried out to achieve a sustainable bridge deck that still complies with the requirements. This resulted in the B-r16-s125-h215-c25 bridge deck, which achieved an ECI reduction of 27% and 32%, depending on the type of cement used in the concrete mixture. The percentage reduction in ECI is greater for the CEM III variants than for the CEM I variants. This is because the low Portland cement content of CEM III results in a

lower ECI for the concrete component, thereby amplifying the effect of more sustainable reinforcement.
Reducing the amount of concrete by decreasing the concrete cover and doubling the reinforcement results in a slight sustainability improvement of only 4% for the CEM I concrete variant compared to the reference variant with steel. For the CEM III variant, there is even an increase in ECI of 2%, indicating that this variant has a worse environmental performance than the reference variant.
Looking ahead, the implementation of the new LCA standard will further widen the difference in environmental costs between steel and BFRP. The use of BFRP will then enhance the sustainability of structures even more than it currently does with the existing calculation method.

8. Discussion

In this chapter, the results of the report will be interpreted. The analysis will determine whether the results align with the expected outcomes and assess the applicability of the constructed model for its intended purpose. Additionally, the implications and limitations of the model will be further elaborated.

8.1 Discussion on numerical model

For various design variants of a bridge deck in an inverted T-girder bridge, a numerical model was developed to determine the traffic load distribution. The design variants of the bridge deck differ in reinforcement material (steel or BFRP), concrete cover, effective depth, and amount of reinforcement. The modifications to the bridge deck are reflected in the orthotropic properties of the orthotropic plate in terms of effective stiffness and height of the plate. Reinforcement is not explicitly modelled but is incorporated through the modification of the effective stiffness of the cracked concrete section. As a result, the model provides valuable insights into the differences in structural behaviour and traffic load distribution of the various bridge deck design variants, even though it does not represent an exact characterization of the actual system. However, this modelling approach makes it easily applicable to different systems with varying dimensions and characteristics.

Furthermore, several simplifications have been made that may affect the validity of the model. Firstly, the T-girders have been modelled as centroidal ribs. This simplification differs from the actual situation where the T-girders are eccentrically connected to the bridge deck rather than centrally. This approach simplifies the analysis as the rib's effects on the deck are symmetrical. However, eccentric ribs introduce additional complexities due to the eccentricity causing asymmetrical stress distributions and influencing the torsional stiffness of the ribs in the deck. Centroidal ribs were chosen to comply with the requirement of the model to understand the overall behaviour of the deck without accounting for complex detailed interactions.
Secondly, a linear model was chosen, which does not account for non-linear effects. Concrete exhibits non-linear material properties that are not fully captured in this linear model. The cracking behavior of concrete, plasticity, and the interface properties between rebar (steel or BFRP) and concrete are not modeled. However, by modeling linearly, the computational cost of this approach is very efficient. This method, being a common and conservative way to calculate load effects, provides valuable insights into load distribution and allows for quick and easy adjustments to design variants.

In the model, only vertical traffic loads have been considered. The critical traffic load configurations were derived from literature in combination with a trial-and-error process. While the actual critical loads may differ slightly, it is expected that the current maximum loads provide a very good approximation of the maximum values. Horizontal loads resulting from wind, braking vehicles, or temperature differences have been excluded. Additionally, special loads such as collisions, explosions, and seismic loads were not included in the model. For a more in-depth study, these loads could also be considered. However, this research primarily focused on the effect of BFRP rebar and reduced concrete cover on the distribution of traffic loads in the inverted T-girder bridge deck.

8.2 Discussion on results

The results of the numerical model highlight the effect of changing the effective stiffness of the bridge deck on the load distribution. Design variants that are stiffer due to steel reinforcement or a greater effective depth result in a wider distribution of the transverse bending moments. This effect is clearly visible in the contour plots of the transverse bending moments. Conversely, it can be observed that when the stiffness is relatively low, for example by using BFRP with a reduced bridge deck height, the transverse bending moments are more concentrated towards the T-girders.

In the context of transverse shear force, it has been found that the average shear force is most dependent on the effective depth and, to a lesser extent, on the reinforcement material itself. This aligns with the theory of Grasser & Thielen (1991), who defined the effective width used in German practice for simply supported one-way slabs as a function of, among other factors, the effective depth. Other parameters influencing the effective width include the width of the loaded area and the center-to-center distance between the load and the support. These parameters are consistent across all variants, suggesting that the difference in effective depth has a causal relationship with the distribution of the transverse shear force.

For the steel-reinforced variant of the bridge deck, it was found that fatigue is the critical failure mechanism. The BFRP variants all appear to have transverse shear force as the critical failure mechanism. This result corresponds with experimental research on concrete slabs reinforced with FRP by Abdul-Salam, Farghaly, & Benmokrane (2016), who also found shear to be the failure mechanism. Additionally, the hypothesis drawn based on the preliminary analysis of bridge deck capacity using various design codes in Chapter 3 was confirmed. This analysis also indicated that shear force would most likely be the critical failure mechanism for the BFRP reinforced bridge decks.

Placing these results in the context of reality raises a question. The effect of compressive membrane action (CMA) was not included in the numerical model, nor in determining the capacities. Research by Tharmarajah, Taylor, Cleland, & Robinson (2014) has shown that the effect of CMA can indeed provide significant additional capacity, which was also applied in the Thompson Bridge project. Therefore, the method used in this report may yield more conservative outcomes because the CMA effect was not considered. CMA was not applied because the aim of this research is to determine the capacities using simple design formulas, as is typically the traditional approach with steel-reinforced bridge decks.

9. Conclusions

To address the main research question and summarize the entire study, this chapter will first answer the sub-research questions. Subsequently, this will enable the main research question to be answered.

To what extent has BFRP already been used in built structures and what design principles were followed?

- The extent to which BFRP has been applied as reinforcement in concrete structures is very limited. BFRP is a relatively new material that has only been used on a small scale in structures which require minimal structural performance. These structures include, for example, fire walls, non-structural reinforcement in floors, and pilot projects in testing phases such as an approach slab and a small pedestrian bridge at a university. The design principles followed in these applications are derived from the American standard formulas of the ACI440 code, the Canadian CSA S806, and the BRL0513 amendment to the Eurocode.
- A project where BFRP has been applied with higher structural performance required, is the Thompsons' Bridge in Northern Ireland. This is currently the only known project where BFRP has been used in the concrete deck of a bridge in the main road network. Unlike traditional capacity calculations as outlined in the standards, this project utilized the principle of compressive membrane action (CMA).

What are the current design codes and guidelines for using FRP rebars in concrete structures?

- The most comprehensive design codes and guidelines are found in North America. The American ACI 440 standards and the Canadian CSA S806 standards pertain to FRP. Some of these standards address FRP in general, while others are specific to GFRP. These latter standards may possibly also be applicable to BFRP, as the mechanical properties of GFRP and BFRP are very similar.
- Europe does not yet have comprehensive design standards for FRP reinforced concrete. The forthcoming Eurocode includes only an informative Annex R that outlines some basic principles. Additionally, there is the Dutch amendment, BRL0513, which provides modifications to NEN-EN 1992 for GFRP and CFRP rebar to make them applicable instead of steel rebar.

How can the load distribution in a concrete bridge deck reinforced with BFRP be tested with a numerical model?

- This research has demonstrated that an inverted T-girder bridge can be modeled using a quasi-linear numerical model. In this model, the bridge deck is represented as an orthotropic 2D plate with adjusted effective E-moduli. These adjustments are based on the assumption that concrete is uncracked in longitudinal direction, while a lower E-modulus is used in the transverse direction due to the cracked state. The T-girders are modeled as centroidal ribs and are also assumed to consist of uncracked concrete.

- The model has shown that BFRP rebar in the bridge deck reduces the stiffness of the deck, altering the distribution of traffic loads compared to the situation when steel reinforcement is used. Traffic loads are less effectively distributed from the bridge deck to the girder. In the model, the critical deformations, bending moments, and shear forces can be determined. These critical deformations and sectional forces are then checked against the capacity formulas of BRL0513 to verify if the structure meets the requirements.

What is the difference in governing failure mechanisms between BFRP reinforced concrete bridge decks and steel reinforced concrete bridge decks?

- For steel-reinforced concrete bridge decks, it has been found that fatigue of the steel is the critical failure mechanism. In contrast, BFRP is much more resistant to fatigue but less effective against shear forces. The critical failure mechanism for all BFRP-reinforced concrete bridge decks appears to be shear force. Literature research has shown that this reduction in shear capacity is due to the lower E-modulus of BFRP, which leads to a smaller concrete compression zone, higher crack widths and therefore a decrease in aggregate interlock. In addition, the dowel action of BFRP rebars is lower than steel rebars, due to lower transverse strength of the BFRP rebar material.
- The numerical model has shown that a decrease in effective depth increases the occurring maximum shear force, as there is less opportunity for the shear force to spread. By replacing the steel reinforcement in the bridge deck one-to-one with BFRP and reducing the amount of concrete by decreasing the concrete cover, the occurring shear force increases by approximately 5%, while the capacity decreases by 33%.
- For the bridge in this case study, it was found that reducing the bridge deck height from 250 mm to 200 mm and using BFRP results in a shear capacity unity check that does not meet the requirements in CC3. Therefore, additional capacity must be found, for example, by using more advanced modeling principles, to make this design suffice.
- An optimization has been found, reducing the bridge deck height from 250 mm to 215 mm, while maintaining the same amount of reinforcement and a concrete cover of 25 mm. This variant meets all the structural requirements.

What is the CO2 reduction of a concrete bridge deck when BFRP combined with a smaller concrete cover is used compared to traditional steel reinforcement with a thicker concrete cover?

- The current LCA standard, also used in this calculation, is NEN-EN 15804+A1. An LCA study based on cradle-to-gate phases (A1-A3) was conducted and provided extensive insights into the different ECI values of the design variants. Depending on the type of cement used, only replacing steel with BFRP results in an ECI reduction of 20% to 26%.
- It has been found that when, in addition to using BFRP, the thickness of the bridge deck is also reduced from 250 mm to 200 mm, the total ECI reduction increases to 30% to 34%. However, according to the applied calculation method, this variant does not meet the transverse shear requirements. Therefore, a methodology to acquire additional transverse shear capacity is necessary.
- An optimization has been found, reducing the bridge deck height from 250 mm to 215 mm, while maintaining the same amount of reinforcement and a concrete cover of 25 mm. This variant has an ECI reduction of 27% to 32%.

- Doubling the amount of BFRP while reducing the bridge deck thickness from 250 mm to 200 mm appears to have very little impact on the ECI compared to the reference variant.
- Probably in 2026, the new European LCA standard, NEN-EN 15804+A2, will come into effect. With this updated calculation method, the ECI of steel will increase by 82%, while that of BFRP will increase by only 39%. Therefore, the use of BFRP will yield even greater sustainability benefits under the new standard than it already does with the current calculation method

Main research question:

To what extent does the use of BFRP in combination with a smaller concrete cover, in a cast-in-situ concrete bridge deck on prefabricated inverted T-beams, influence the shear capacity?

- This research has demonstrated that BFRP rebar in a bridge deck leads to a reduction in shear capacity. Various design parameters have been adjusted. According to the model, the occurring shear force is primarily dependent on the effective depth. Thus, the impact on shear force is twofold: on the load effect side and on the capacity side of the cross-section.
- In the traditional steel design variant, the unity check for shear force is 0,67. For the variant with BFRP, this increases to 0,87 if the effective depth remains the same but increases less to 0,76 if the effective depth increases by reduced cover.
- Using BFRP rebar instead of steel rebar and reducing the overall height of the bridge deck to save concrete and make the bridge deck more sustainable, further decreases the effective depth. This results in both an increase in the occurring shear force and a drastic reduction in shear capacity. Reducing the bridge deck from 250 mm to 215 mm and maintaining a concrete cover of 25 mm instead of the traditional 50 mm, proves to be the optimized design solution for this specific case study. This design variant meets the shear force requirements with a unity check of 0,93 and achieves an ECI reduction of 27% to 32% depending on the cement type used.
- Further reducing the bridge deck height for this specific case study to save more concrete, results in a structure that does not meet structural requirements in terms of one-way shear capacity, as the unity check exceeds 1. To potentially achieve additional concrete savings by reducing the construction height, a more advanced alternative calculation method must be applied.

10. Recommendations

Based on the findings of this study, several recommendations can be made to enhance the design and implementation of BFRP reinforcement in bridge decks of inverted T-girder bridges. The recommendations are divided into recommendations for practice and recommendations for future research.

10.1 Recommendations for practice

- It is strongly recommended that the industry standardize the production process and quality control of BFRP as soon as possible. There is a significant need for uniform quality of BFRP rebar with minimal variation in mechanical properties. Currently, there is too much variation in the quality of available BFRP on the market, necessitating costly and extensive testing of BFRP rebar.
- Comprehensive European design standards are still lacking. To make the design and calculation of BFRP reinforced structures more accessible, it is recommended to develop European design standards. Currently, Europe lags North American standards, which already have several comprehensive design standards in practice. In Europe, one is still limited to an informative annex in the forthcoming Eurocode and a few amendment sheets to the Eurocode.
- This study has demonstrated that the use of BFRP can be feasible in the bridge deck of an inverted T-girder bridge. Therefore, it is recommended to consider the use of BFRP in bridge decks as a design option, as it offers higher durability and is resistant to corrosion. However, it is advisable to apply BFRP in situations where the bridge deck has a relatively small span compared to the effective depth of the deck in transverse direction. For larger span to depth ratios, deflections and cracks may become excessive due to the lower E-modulus of the BFRP material.
- To make the design process of BFRP reinforced concrete decks more efficient, it is advised to start with designing for shear capacity. This study has shown that shear is most likely the critical failure mechanism for BFRP reinforced concrete decks. By optimizing the bridge deck for shear first, it is likely that the structure will suffice for other failure mechanisms as well.
- It is recommended to apply BFRP rebar in concrete bridge decks and to reduce the height of the concrete bridge deck. This study has demonstrated that, for this specific case study, a one-to-one replacement of steel reinforcement with BFRP reinforcement is feasible. Additionally, concrete savings can be achieved by reducing the construction height of the bridge deck from 250 mm to 215 mm.

10.2 Recommendations for future research

- In future studies, the numerical model could be further developed to include non-linear effects. This could involve modeling the non-linear material properties of concrete, as well as the cracking behavior and explicitly modelling the rebars with their bond-slip characteristics. While this would make the model less efficient in terms of computational cost, it could provide a more accurate representation of the bridge deck-girder system.
- The model could also adopt a less simplified geometric form, such as a 3D bridge deck instead of 2D, and the girders could be modeled as 2,5D or 3D elements instead of 1D centroidal ribs. If this extended geometry input is combined with the non-linear material properties, the effect of CMA could also be modeled, which previous research has indicated can significantly increase additional capacity.
- By applying BFRP reinforcement and potentially making the bridge deck thinner, the deck becomes less stiff, resulting in more load being transferred to the girders. According to the model used, the load on the maximum loaded T-girder increases by 5%. Future research could investigate the impact of this additional load on the girders' lifespan, potential for reuse and sustainability of the total bridge deck-girder system.
- Further research is needed on BFRP at the end of its service life. It is well known that steel can be relatively easily separated from concrete and is very recyclable. However, much is still unknown about the end-of-life processes for BFRP.
- Further research into the possibilities of producing bent BFRP rebar without loss of capacity would be highly desirable. Currently, bent BFRP rebar experiences significant capacity loss, often necessitating the use of steel for bent rebar elements. Since steel is less sustainable and prone to corrosion, a larger (local) concrete cover is required, making the structure less environmentally friendly.

References

AASHTO. (2012). *AASHTO LRFD Bridge Design Specifications.* Washington D.C., 1661 pp.: American Association of State Highway and Transportation.

Abdul-Salam, B., Farghaly, A. S., & Benmokrane, B. (2016). *Mechanisms of shear resistance of one-way concrete slabs reinforced with FRP bars.* https://doi.org/10.1016/j.conbuildmat.2016.10.015 : Construction and Building Materials, Vol. 127, pp. 959-970.

Abed, F., Refai, A. E., & Abdalla, S. (2019). *Experimental and finite element investigation of the shear performance of BFRP-RC short beams.* https://doi.org/10.1016/j.istruc.2019.06.019 : Structures, Vol. 20, pp. 689-701.

Achillides, Z. (1998). *Bond Behaviour of FRP Bars in Concrete.* Sheffield, United Kingdom: PhD Thesis, The University of Sheffield, 368 pp.

ACI 318-19. (2019). *Building Code Requirements for Structural Concrete.* https://doi.org/10.14359/51716937 : American Concrete Institute, Farmington Hills, MI, USA, 624 pp.

ACI 440.11-22. (2022). *Building Code Requirements for Structural Concrete Reinforced with Glass Fiber Reinforced Polymer (GFRP) Bars-Code and Commentary.* Farmington Hills, MI, USA, 260 pp.: American Concrete Institute.

ACI 440.1R-15. (2015). *Guide for the Design and Construction of Structural Concrete Reinforced with Fiber-Reinforced Polymer (FRP) Bars.* Farmington Hills, MI, USA, 88 pp.: American Concrete Institute.

Arslan, G. (2011). *Diagonal Tension Failure of RC Beams Without Stirrups.* https://doi.org/10.3846/13923730.2012.671264 : Journal of Civil Engineering & Management, Vol. 18, No 2, pp. 217-226.

ASCEM. (2023). *Hoofdrapport - Invloed toepassen van basaltwapening als alternatief voor stalen wapening op milieu impact prefab stootplaat.*

ASTM D 2584. (2011). *Standard Test Method for Ignition Loss of Cured Reinforced Resins.* https://doi.org/10.1520/D2584-18 : ASTM-International.

Bagherpour, S. (2012). *Fibre Reinforced Polyester Composites.* https://doi.org/10.5772/48697 : Rijeka: IntechOpen, 242 pp.

Basalt.Guru. (2016). *Swimming pool construction using basalt rebar*. Retrieved from Basalt.Guru: https://basalt.guru/swimming-pool-construction-using-basalt-rebar/

Baumann, T., & Rüsch, H. (1970). *Versuche zum Studium der Verdübelungswirkung der Biegezugbewehrung eines Stahlbetonbalkens.* Ernst: Deutscher Ausschuss für Stahlbeton (DAfStb), Heft, No 210, c. 87.

Betonakkoord. (2018). *Betonakkoord voor Duurzame Groei.*

Bhat, T., Chevali, V., Liu, X., Feih, S., & Mouritz, A. (2015). *Fire structural resistance of basalt fibre composite.* https://doi.org/10.1016/j.compositesa.2015.01.006 : Composites Part A: Applied Science and Manufacturing, Vol. 71, pp. 107-115.

Blaauwendraad, J. (2010). *Plates and FEM.* https://doi.org/10.1007/978-90-481-3596-7 : Springer Science, Dordrecht Heidelberg London New York.

Braam, C., & Langendijk, P. (2008). *CB2 Constructieleer Gewapend Beton.* 's-Hertogenbosch: Cement en BetonCentrum.

BRL 0513. (2015). *Glasvezelstaven voor toepassing als wapening in beton.* KOMO Kwaliteits- en Toetsingscommissie.

Cladera, A. (2003). *Shear design of reinforced high-strength concrete beams.* Universitat Politècnica de Catalunya, Barcelona, Spain: PhD Thesis. Sapin: ACHE (Spanish Concrete Association).

CSA S806-12. (2012). *Design and construction of building structures with fibre-reinforced polymers.* Mississauga, Ontario, Canada: Canadian Standards Association, 201 pp.

Deutsche Basalt Faser. (2021). *Basalt voor betonwapening.*

Ebid, A. M., & Deifalla, A. (2021). *Prediction of shear strength of FRP reinforced beams with and without stirrups using (GP) technique.* https://doi.org/10.1016/j.asej.2021.02.006 : Ain Shams Engineering Journal, Vol. 12, No. 3, pp. 2493-2510.

Ellis, D. S., Tabatabai, H., & Nabizadeh, A. (2018). *Residual Tensile Strength and Bond Properties of GFRP Bars after Exposure to Elevated Temperatures.* https://doi.org/10.3390/ma11030346 : Materials, Vol. 11, No. 3, p. 346.

El-Ragaby, A., El-Salakawy, E., & Benmokrane, B. (2007). *Fatigue Life Evaluation of Concrete Bridge Deck Slabs Reinforced with Glass FRP Composite Bars.* https://doi.org/10.1061/(ASCE)1090-0268(2007)11:3(258) : American Society of Civil Engineers(ASCE), Vol. 3, No 3,.

Feng, G., Guo, S., Zhou, L., Luo, W., Guo, X., Jin, Z., & Zhu, D. (2024). *Effects of surface characteristics and alkalinity on the deterioration of BFRP bars and BFRP-SSC interface in seawater environment.* https://doi.org/10.1016/j.compositesb.2023.111072 : Composites Part B: Engineering, Vol. 268, .

fib bulletin 40. (2007). *FRP reinforcement in RC structures.* Lausanne, Switzerland, 151 pp.: Fédération Internationale du Béton.

fib Model Code for Concrete Structures. (2020). *fib Model Code for Concrete Structures.* Lausanne, Switzerland, 780 pp.: Fédération Internationale du Béton.

FprEN_1992-1-1:2022. (2022). *Eurocode 2: Design of concrete structures —.* CEN, 410 pp.

Fu, H.-d., Feng, X.-y., Liu, J.-X., Yang, Z.-m., He, C., & Li, S.-k. (2020). *An investigation on anti-impact and penetration performance of basalt fiber composites with different weave and lay-up modes.* https://doi.org/10.1016/j.dt.2019.09.005 : Defence Technology, Vol. 16, No. 4, pp. 787-801.

Gilbert, R. I. (2013). *Time-Dependent Stiffness of Cracked Reinforced and Composite Concrete Slabs.* https://doi.org/10.1016/j.proeng.2013.04.006 : Procedia Engineering, Vol. 57, pp. 19-34.

Grasser, E., & Thielen, G. (1991). *Design aid for the calculation of sectional forces and deformations of reinforced concrete structures.* Deutscher Ausschuss für Stahlbeton, Heft, No, 240 c. 86.

GRCA International. (2019). *AR Glassfibre for GRC.* Northampton, United Kingdom: GRCA Technical Working Group.

Guadagnini, M., Pilakoutas, K., & Waldron, P. (2006). *Shear Resistance of FRP RC Beams: Experimental Study.* https://doi.org/10.1061/(ASCE)1090-0268(2006)10:6(464) : Journal of Composites for Construction, Vol. 10, No. 6.

Hoven, T. v. (2023, december 18). *Licht, sterk, niet-corroderend en honderd procent recyclebaar*. Retrieved from Beton en Staalbouw: https://www.betonenstaalbouw.nl/artikel/licht-sterk-niet-corroderend-en-honderd-procent-recyclebaar/

Kanakubo, T., & Shindo, M. (1997). *Shear Behaviour of Fiber-Mesh Reinforced Plates.* Sapporo, Japan: Third International Symposium on Non-Metallic (FRP) Reinforcement for Concrete Structures.

Kang, J. (2017). *Structural Behaviors of Reinforced Concrete Piers Rehabilitated with FRP Wraps.* https://doi.org/10.1155/2017/2989238 : Hindawi.

Khuntia, M., & Stojadinovic, B. (2001). *Shear strength of reinforced concrete beams without transverse reinforcement.* ACI Structural Journal.

Kostovos, M. D., & Pavlovic, M. N. (1999). *Ultimate Limit State Design of Concrete Structures - A New Approach.* London, United Kingdom: Institution of Civil Engineers.

Lantsoght, E., Veen, C. v., Boer, A. d., & Walraven, J. (2015). *Transverse load redistribution and effective shear width in reinforced concrete slabs.* Heron, Vol. 60 (2015) No. 3, pp. 145-179.

Leenders, F. (2024). *Basaltvezelwapening voor busremise.* https://www.cementonline.nl/basaltvezelwapening-voor-busremise: Cement.

Lingen, K. v. (2024). *Flexural Behaviour of Concrete Reinforced With Basalt Fibre Reinforcement Bars.* https://resolver.tudelft.nl/uuid:76eb0a45-77c5-488c-bfb3-d5873845a67f : Master Thesis, Faculty of Civil Engineering and Geosciences.

Lu, J., Yang, Y., & Hendriks, M. A. (2024). *A closed-form solution of dowel action based on beam on elastic foundation theory and fracture mechanics.* https://doi.org/10.1016/j.engstruct.2024.118430 : Engineering Structures, Vol. 315.

Malan, A., & Rooyen, G. v. (2013). *Critical normal traffic loading for flexure of skew bridges according to TMH7.* Journal of the South African Institution of Civil Engineering, Vol. 55, No. 3.

Medeiros, M., Rocha, F., R.A.-Medeiros-Junior, & Helene, P. (2017). *Corrosion potential: influence of moisture, water-cement ratio, chloride content and concrete cover.* https://doi.org/10.1590/S1983-41952017000400005 : Ibracon Structures and Materials Journal, Vol. 10, No. 4, pp. 864-885.

Nagatomo, K., Matsubara, S., & Kaku, T. (1992). Bond behaviour of deformed bars under lateral compressive and tensile stress. *Proceedings of the Bond in Concrete Conference Riga, pp. 1-69.* Riga, Latvia.

Nanni, A., Luca, A. D., & Zadeh, H. (2014). *Reinforced concrete with FRP bars. Mechanics and design, international standard book no-13.* https://doi.org/10.1201/b16669 , 418 pp.: CRC Press.

Nasvik, J. (2016, April 13). *Basalt Fiber Reinforced Rebar*. Retrieved from For Construction Pros: https://www.forconstructionpros.com/concrete/equipment-products/article/12184173/basalt-fiber-reinforced-rebar#:~:text=The%20process%20of%20making%20the,0007%20inches%20in%20diameter.

NEN-EN 1991-2+C1. (2015). *Eurocode 1: Belastingen op constructies – Deel 2: Verkeersbelasting op bruggen.* Delft, the Netherlands, 187 pp.: Nederlands Normalisatie-instituut.

NEN-EN 1992-1-1+C2. (2011). *Eurocode 2: Ontwerp en berekening van betonconstructies - Deel 1-1: Algemene regels en regels voor gebouwen.* Delft, the Netherlands, 247 pp.: Nederlands Normalisatie-instituut.

NEN-EN-ISO14040. (2006). *Environmental management - Life cycle assessment – Principles and framework.* Delft, the Netherlands: The International Organization for Standardization (ISO), 20 pp.

NEN-EN-ISO14044. (2006). *Environmental management - Life cycle assessment — Requirements and guidelines.* Delft, the Netherlands: The International Organization for Standardization (ISO).

Nishimura, K., Onishi, N., & Kawazu, M. (2020). *Experimental Study On Bond Split Failure of Tension Reinforcing Bars Embedded in Concrete.* https://doi.org/10.1002/2475-8876.12154 : Japan Architectural Review, Vol. 3, No. 3, pp. 318-333.

Orlimex CZ s.r.o. (2022). *Environmental Product Declaration.* https://www.mrpi.nl/epd-files/epd/1.1.00389.2022_MRPI-EPD_Basalt%20Fibre%20Reinforced%20Polymer%20Rebar-%2010mm%20_FINAL.pdf: Eco Platform.

Orlitech. (2024). *Home*. Retrieved from Orlimex: https://orlitech.co.uk/

Orr, J., & Gibbons, O. (2020). *How to calculate embodied carbon.* https://doi.org/10.17863/CAM.53699: The Institution of Structural Enigneers.

Pavlovic, A., Donchev, T., Petkova, D., & Staletovic, N. (2022). *Sustainability of alternative reinforcement for concrete structures: Life cycle assessment of basalt FRP bars.* https://doi.org/10.1016/j.conbuildmat.2022.127424 : Construction and Building Materials, Vol. 334.

Pilakoutas, Guadagnini, Neocleous, & Matthys. (2009). Design guidelines for FRP reinforced concrete structures. *Proceedings of the Institution of Civil Engineers* (pp. Vol. 164, No. 4, pp. 255-263). https://doi.org/10.1680/stbu.2011.164.4.255 : Structures and Buildings.

Pilakoutas, K. (2022). *Composites in concrete construction In Failure Analysis of Industrial Composite Materials (Gdoutos A, Pilakoutas K and Rodopoulos C (eds)).* New York: McGraw-Hill.

Prince-Lund Engineering. (2019). *Fiber Reinforced Polymers Characteristics and Behaviors*. Retrieved from Prince-Lund Engineering: https://www.princelund.com/fiber-reinforced-polymers.html#gsc.tab=0

Qassim, S. H., & Al-Saraj, W. K. (2021). Shear compression failure in reinforced self-compacted lightweight concrete beams subjected to axial load. *International Conference on Latest Developments in Materials & Manufacturing* (pp. Vol. 60, No. 3, pp. 1179-1185). https://doi.org/10.1016/j.matpr.2021.08.035 : Materialstoday: Proceedings.

Rajak, D. K., Wagh, P. H., & Linul, E. (2022). *A Review on Synthetic Fibers for Polymer Matrix Composites: Performance, Failure Modes and Applications.* https://doi.org/10.3390/ma15144790 : Materials, Vol. 15, No. 14.

Refai, A. E., & Abed, F. (2015). *Concrete Contribution to Shear Strength of Beams Reinforced with Basalt Fiber-Reinforced Bars.* https://doi.org/10.1061/(ASCE)CC.1943-5614.0000648 : Journal of Composites for Construction, Vol. 20, No. 4.

ROK. (2021). *RTD 1001 Richtlijnen Ontwerp Kunstwerken.* Rijkswaterstaat.

Rooij, R. d. (2011). *Loading capacity of laterally restrained prestressed concrete slabs.* https://resolver.tudelft.nl/uuid:bf3dcd94-c512-4849-9bbc-ccf3b0913925 : Master thesis TU Delft, Delft, the Netherlands.

Rossini, M., Spadea, S., & Nanni, A. (2019). *Pedestrian Bridge as Clarifying Example of FRP-RC/PC Design (ACI Special Publication).* SP-333: Advances in Concrete Bridges: Design, Construction, Evaluation, and Rehabilitation.

Ruiz, F. P. (2022, June 27). *A Greener Rebar*. Retrieved from Green Building Advisor: https://www.greenbuildingadvisor.com/article/basalt-rebar

Samad, A., Mohamad, N., Ali, N., Jayaprakash, J., & Mendis, P. (2016). *Rehabilitation of continuous reinforced concrete beams in shear by external bonding of carbon fiber reinforced polymer strips for sustainable construction.* https://doi.org/10.4028/www.scientific.net/KEM.708.49 : Key Engineering Materials, Vol. 708, pp. 49-58.

Schmidt, A., Kampmann, R., Telikapalli, S., Emparanza, A. R., & Caso, F. D. (2019). Basalt FRP Production: Market Analysis and State-of-the-Art Report. *Proceedings of the FIB Symposium 2019.* Krakow, Poland: Innovations in Materials, Design and Structures.

SCIA Engineer. (n.d.). *Orthotropic behaviour of plates*. Retrieved from SCIA: https://www.scia.net/en/support/faq/scia-engineer/modelling/orthotropic-behaviour-plates

Solyom, S., & Balázs, G. L. (2020). *Bond of FRP bars with different surface characteristics.* https://doi.org/10.1016/j.conbuildmat.2020.119839 : Construction and Building Materials, Vol. 264,.

Stoiber, N., Hammerl, M., & Kromoser, B. (2020). *Cradle-to-gate life cycle assessment of CFRP reinforcement for concrete structures: Calculation basis and exemplary application.* https://doi.org/10.1016/j.jclepro.2020.124300 : Journal of Cleaner Production, Vol. 280, No. 1.

Swann, W. (2021). *Developing a low-carbon, circular economy for steel.* https://doi.org/10.56330/DPLL5365 : The Structural Engineer Journal, Vol. 99, No. 4, pp. 18-19.

Tassios, T. (1979). Properties of bond between concrete and steel under load cycles idealising seismic actions. *Proceedings of AICAP-CEB Symposium.* Rome, Italy: CEB Bulletin No. 131, pp. 67-122.

Taylor, H. (1970). *Investigation of the Forces Carried Across Cracks in Reinforced Concrete Beams in Shear by Interlock of Aggregate.* London, UK: Cement and Concrete Association.

Tepfers, R. (1979). *Cracking of concrete cover along anchored deformed reinforcing bars.* https://doi.org/10.1680/macr.1979.31.106.3 : Magazine of Concrete Research, Vol. 31, No. 106, pp. 3-12.

Tharmarajah, G., Taylor, S. E., Cleland, D. J., & Robinson, D. (2014). *Corrosion-resistant FRP reinforcement for bridge deck slabs.* https://doi.org/10.1680/jbren.13.00001 : Bridge Engineering, Vol. 168, No. 3, pp. 208-217.

Tottori, S., & Wakui, H. (1993). Shear Capacity of RC and PC Beams Using FRP Reinforcement. *Proceedings of the International Symposium on Fiber Reinforced Plastic Reinforcement for Concrete Structures.* https://doi.org/10.14359/3944 : American Concrete Institute, Vol. 138, pp. 615-632.

Tracy, B. (2023, January 16). *Cement industry accounts for about 8% of CO2 emissions. One startup seeks to change that.* Retrieved from CBS News: https://www.cbsnews.com/news/cement-industry-co2-emissions-climate-change-brimstone/

Tsai, S. W., & Hahn, H. T. (1980). *Introduction to Composite Materials.* USA, 466 pp.: CRC Press.

Tureyen, A. K., & Frosh, R. J. (2003). *Concrete Shear Strength: Another Perspective.* ACI Structural Journal, Vol. 100, No. 5, pp. 609-615.

United States Patent Office. (1923). *US14624464A- Tipping crucible basalt furnaces.* United States Patent Office.

Vereniging Wapeningsstaal Nederland. (2021). *Environmental Product Declaration.* https://www.mrpi.nl/epd/vwn-vereniging-wapeningsstaal-nederland-wapeningsstaal-voor-toepassing-in-gewapende-betonconstructies/: Nationale Milieudatabase.

Walraven, J. (1981). *Fundamental Analysis of Aggregate Interlock.* https://doi.org/10.1061/JSDEAG.0005820 : Journal of the Structural Division, Vol. 107, No. 11.

Xiong, Z., Wei, W., Liu, F., Cui, C., Li, L., Zou, R., & Zeng, Y. (2021). *Bond behaviour of recycled aggregate concrete with basalt fibre-reinforced polymer bars.* https://doi.org/10.1016/j.compstruct.2020.113078 : Composite Structures, Vol. 256.

Xu, X., Rawat, P., Shi, Y., & Zhu, D. (2019). *Tensile mechanical properties of basalt fiber reinforced polymer tendons at low to intermediate strain rates.* https://doi.org/10.1016/j.compositesb.2019.107442 : Composites Part B: Engineering, Vol. 177.

Yang, Y., Walraven, J., & Uijl, J. d. (2017). *Shear behavior of reinforced concrete beams without transverse reinforcement based on critical shear displacement.*

https://doi.org/10.1061/(ASCE)ST.1943-541X.0001608 : Journal of Structural Engineering, Vol. 143, No. 1.

Zhon Sheng. (2023, October 13). *Zhong Sheng Composite Material*. Retrieved from Strength Showdown: Basalt Rebar vs. Fiberglass Rebar – Which One Prevails?: https://www.frpzs.com/News/Basalt-Rebar-vs-Fiberglass-Rebar.html

Zhou, L., Zheng, Y., & Taylor, S. E. (2018). *Finite-Element Investigation of the Structural Behavior of Basalt Fiber Reinforced Polymer (BFRP) Reinforced Self-Compacting Concrete (SCC) Decks Slabs in Thompson Bridge.* https://doi.org/10.3390/polym10060678 : Polymers, Vol. 10, No. 6.

APPENDIX A – M- κ graphs

This appendix presents the M-κ graphs, from which the effective stiffness was calculated for application in the SCIA Engineer numerical model.

A.1 M- κ graphs

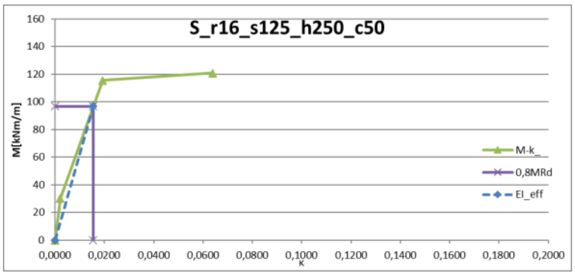

Figure A.1.1: M- κ graph S_r16_s125_h250_c50

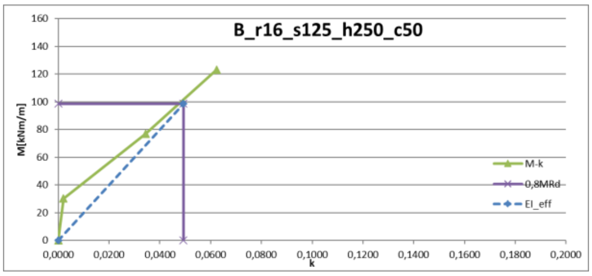

Figure A.1.2: M- κ graph B_r16_s125_h250_c50

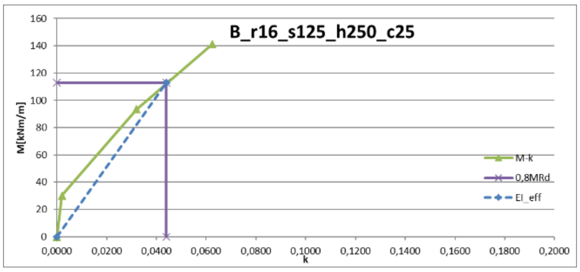

Figure A.1.3: M- κ graph B_r16_s125_h250_c25

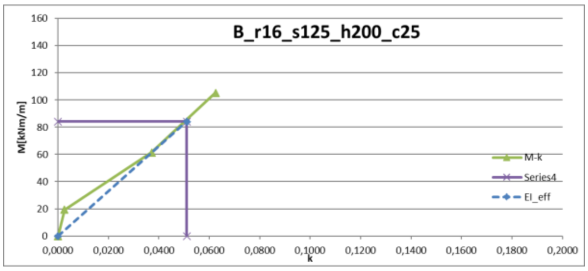

Figure A.1.4: M- κ graph B_r16_s125_h200_c25

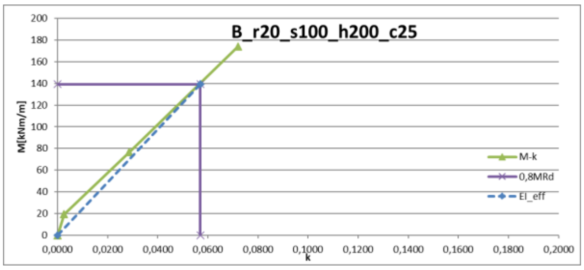

Figure A.1.5: M- κ graph B_r20_s100_h200_c25

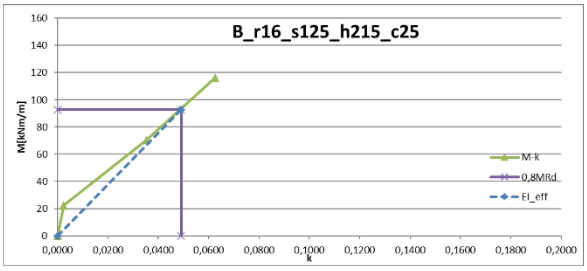

Figure A.1.6: M- κ graph B_r16_s125_h215_c25

APPENDIX B – Model validation

This appendix describes the validation of the numerical model used for the load distribution in the inverted T-girder bridge. To validate the numerical model, the results are compared with those obtained using an analytical method. A surface load of 10 kN/m² is applied to the model, and software then calculates the deflections, reaction forces and bending moments. Subsequently, an analytical model of a single T-girder with bridge deck, considered as a simple beam on two supports, is also used to calculate the deflections, reaction forces and bending moments. If the results in both approaches are of comparable magnitudes, it can be assumed that the model can be validated as reliable.

B.1 Analytical model

Figure B.1 represents the analytical model used to validate the numerical model. The model consists of a simply supported single precast T-girder with the corresponding part of the cast-in-situ bridge deck. The span length is the same as the bridge span, namely 22 meters. A load of 10 kN/m² is chosen, which must be converted to a line load by multiplying it by the width of the T-girder. This width is 1200 mm.

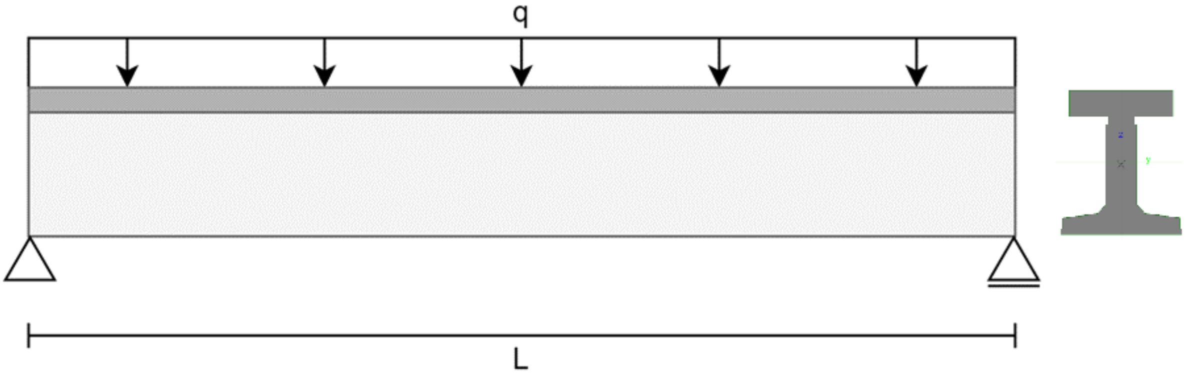

Figure B.1: Analytical validation model

The cast-in-situ concrete bridge deck consists of a different concrete than the precast T-girder, specifically C30/37 and C60/75. Consequently, this results in different E-moduli for these components of the cross-section, complicating the analytical calculation. Therefore, it was decided to model the T-girder entirely as C60/75 and to adjust the width of the cast-in-situ bridge deck according to the appropriate ratio between the E-moduli. This ensures that the flexural rigidity of the cross-section remains consistent. The properties of the model are presented in the table.

Table B.1: Properties analytical validation model

Parameter	value
L	22000 mm
q	10 * 1,2 = 12 kN/m
I_y	$1{,}879 * 10^{11}$ mm^4
$E_{C60/75}$	39100 N/mm^2

B.1.1 Deflection

Deflection of the analytical model can be calculated by substituting the appropriate parameters into the formula below.

$$u_{z,max} = \frac{5}{384}\frac{qL^4}{EI} = \frac{5}{384} * \frac{12 * 22000^4}{39100 * 1{,}879 * 10^{11}} = 4{,}98\ mm$$

B.1.2 Support reactions

The reaction forces of the analytical model can be calculated as the maximum shear force of a system consisting of a uniformly distributed load, q. The model parameters need to be substituted into the formula, yielding the following result:

$$F_z = \frac{1}{2} qL = \frac{1}{2} * 12 * 22 = 132\ kN$$

B.1.3 Bending moments

For the specific input parameters, the value of the maximum bending moment of the analytical model can also be calculated. The formula below provides the maximum moment for a simply supported beam with a uniformly distributed line load q:

$$M_{max} = \frac{1}{8} qL^2 = \frac{1}{8} * 12 * 22^2 = 726\ kNm$$

B.2 Comparing results

For the numerical model, the deflection, support reactions, and maximum bending moments are also determined for a surface load of 10 kN/m². The results of these calculations, along with those from the analytical method, are presented in Table B.3.

Table B.2: Comparison analytical and numerical results

Modeling approach	**$u_{z,max}$ [mm]**	**F_z [kN]**	**M_{max} [kNm]**
Analytical model	4,98	132	726
Numerical model	5,00	133	713
Difference	+ 0,04 %	+ 0,08%	-0,98 %

The comparison between the two modelling approaches indicates that the differences in outcomes are minimal. Therefore, it can be assumed that the numerical model is adequate and generates realistic results.

APPENDIX C – Model outcomes 0,8 M_{Rd} stiffness

This appendix presents the contour plots of the deflections of the bridge deck, obtained from the SCIA Engineer model. The chosen effective stiffness in this model was determined by interpolating the M-κ curve to 0,8M_{Rd}. Based on these contour plots, it can be concluded that the deflections for BFRP-reinforced bridge decks are 4 to 18% higher than those of the steel-reinforced variant. Additionally, the contour plots for transverse bending moments and transverse shear forces are provided. For the steel variants, a greater distribution of transverse bending moments is observed in the bridge deck.

C.1 Deflection – E_{fic} at 0,8M_{Rd}

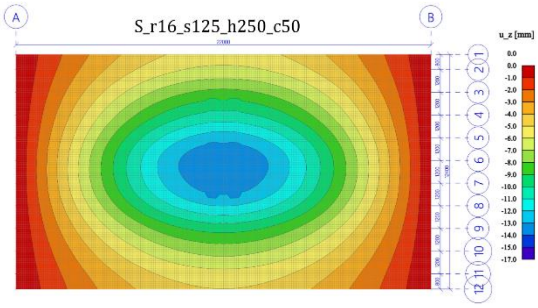

Figure C.1.1: Deflection S_r16_s125_h250_c50

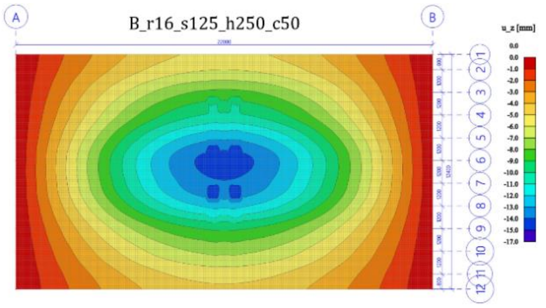

Figure C.1.2: Deflection B_r16_s125_h250_c50

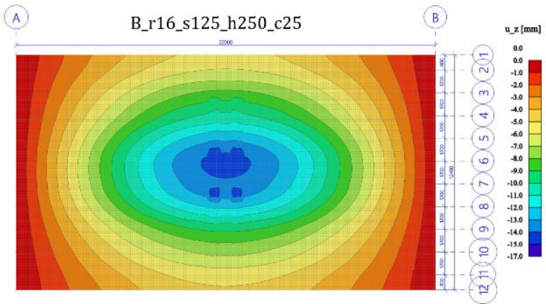

Figure C.1.3: Deflection B_r16_s125_h250_c25

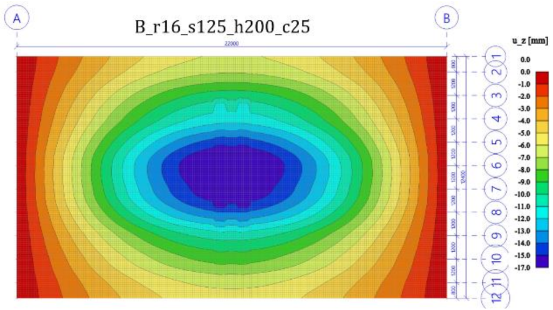

Figure C.1.4: Deflection B_r16_s125_h200_c25

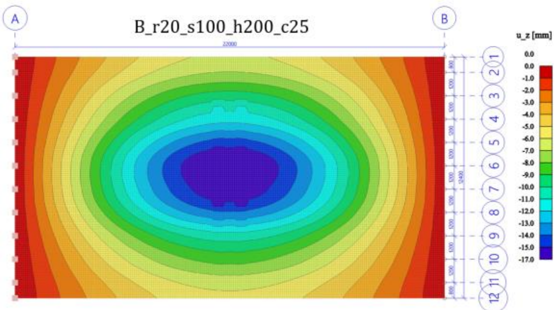

Figure C.1.5: Deflection B_r20_s100_h200_c25

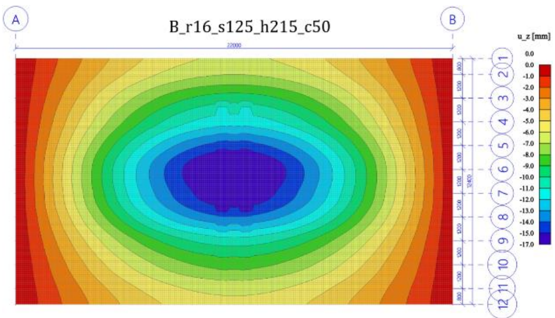

Figure C.1.6: Deflection B_r16_s125_h215_c25

C.2 Transverse Bending moments – E_{fic} at $0{,}8M_{Rd}$

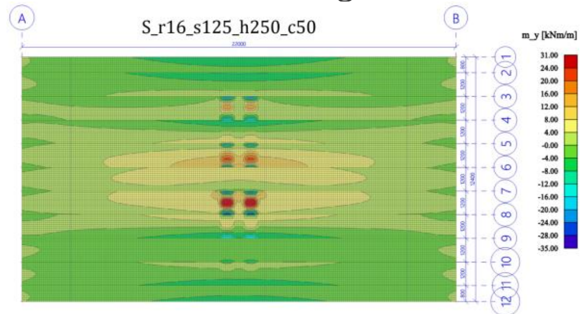

Figure C.2.1: M_{trans} S_r16_s125_h250_c50

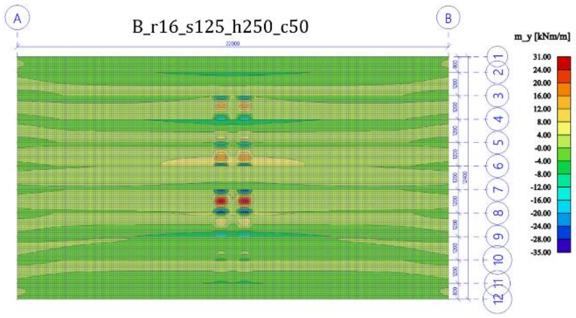

Figure C.2.2: M_{trans} B_r16_s125_h250_c50

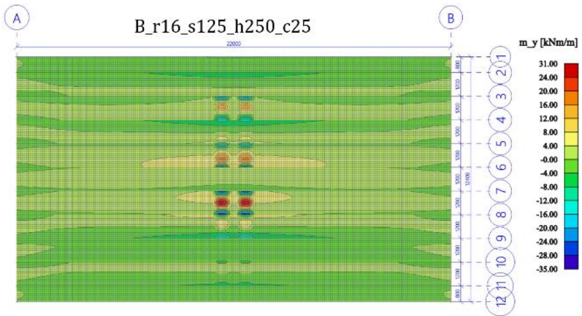

Figure C.2.3: M_{trans} B_r16_s125_h250_c25

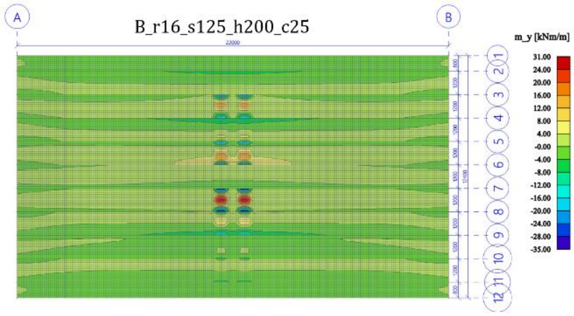

Figure C.2.4: M_{trans} B_r16_s125_h200_c25

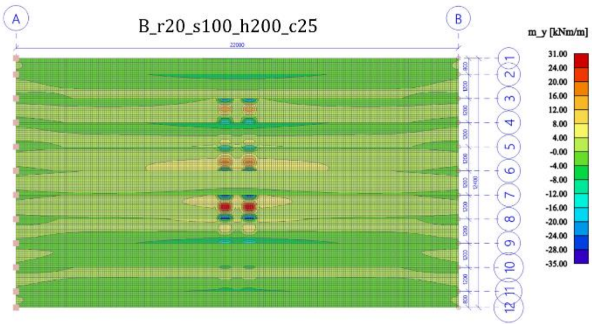

Figure C.2.5: M_{trans} B_r20_s100_h200_c25

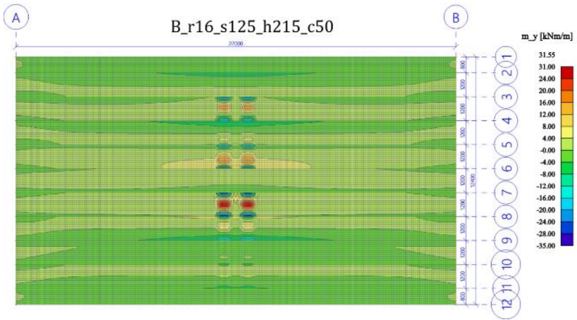

Figure C.2.6: M_{trans} B_r16_s125_h215_c25

C.3 Transverse shear forces – E_{fic} at $0{,}8M_{Rd}$

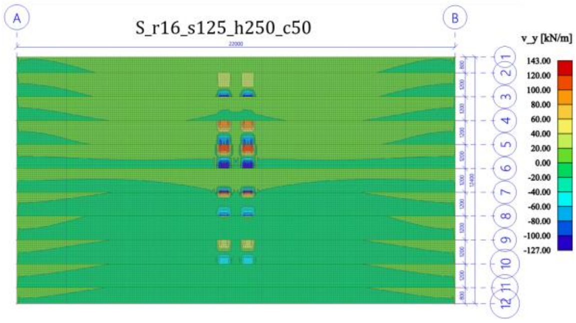

Figure C.3.1: V_{trans} S_r16_s125_h250_c50

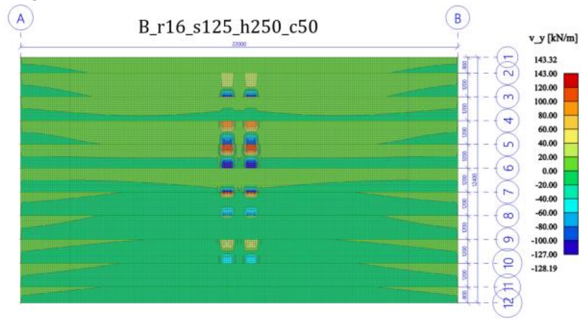

Figure C.3.2: V_{trans} B_r16_s125_h250_c50

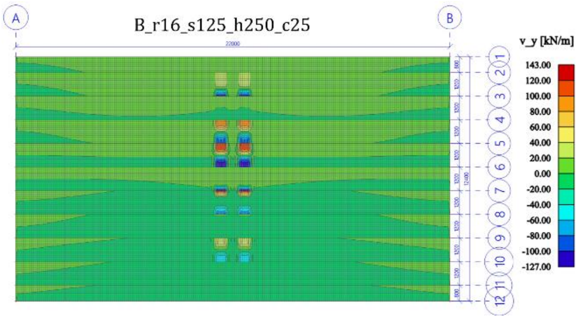

Figure C.3.3: V_{trans} B_r16_s125_h250_c25

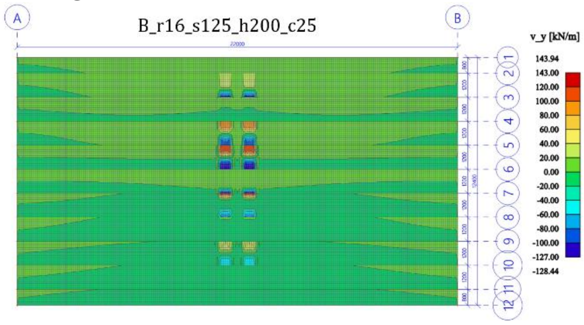

Figure C.3.4: V_{trans} B_r16_s125_h200_c25

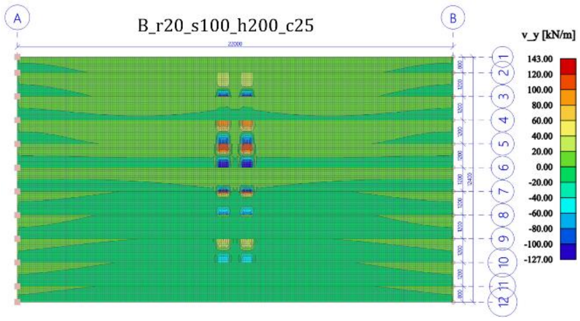

Figure C.3.5: V_{trans} B_r20_s100_h200_c25

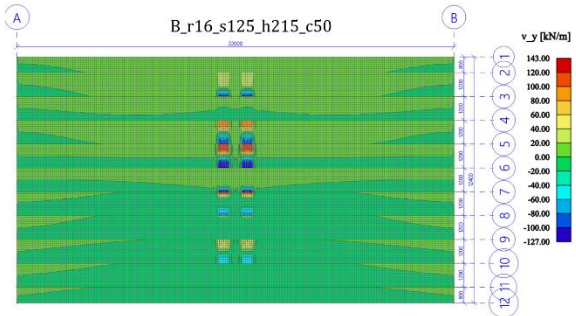

Figure C.3.6: V_{trans} B_r16_s125_h215_c25

APPENDIX D – Model outcomes 0,5 M_{Rd} stiffness

This appendix presents the contour plots of the deflections of the bridge deck, obtained from the SCIA Engineer model. The chosen fictitious stiffness in this model was determined by interpolating the M-κ curve to 0,5M_{Rd}. Based on these contour plots, it can be concluded that the deflections for BFRP-reinforced bridge decks are 4 to 18% higher than those of the steel-reinforced variant. Additionally, the contour plots for transverse bending moments and transverse shear forces are provided. For the steel variants, a greater distribution of transverse bending moments is observed in the bridge deck.

D.1 Deflection – E_{fic} at 0,5M_{Rd}

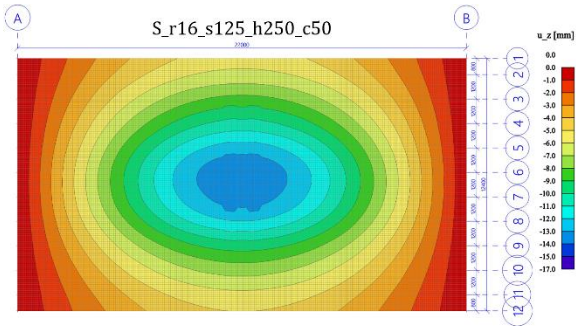

Figure D.1.1: Deflection S_r16_s125_h250_c50

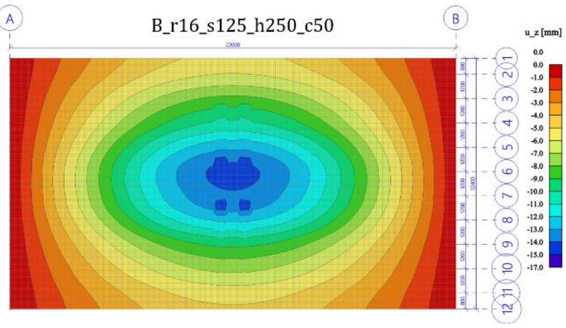

Figure D.1.2: Deflection B_r16_s125_h250_c50

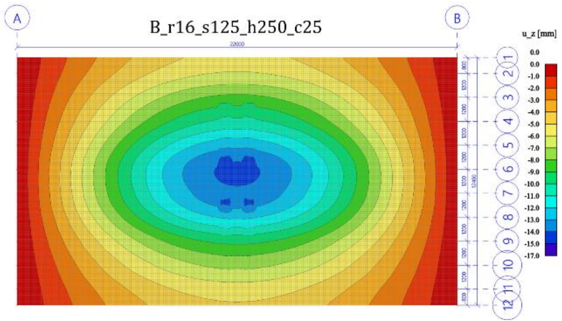

Figure D.1.3: Deflection B_r16_s125_h250_c25

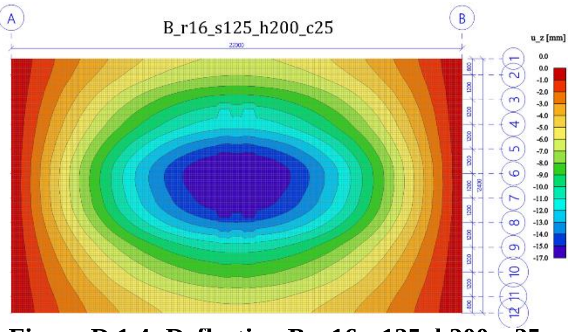

Figure D.1.4: Deflection B_r16_s125_h200_c25

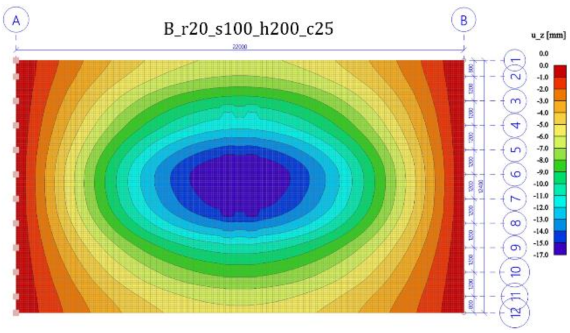

Figure D.1.5: Deflection B_r20_s100_h200_c25

D.2 Transverse Bending moments – E_{fic} at $0{,}5M_{Rd}$

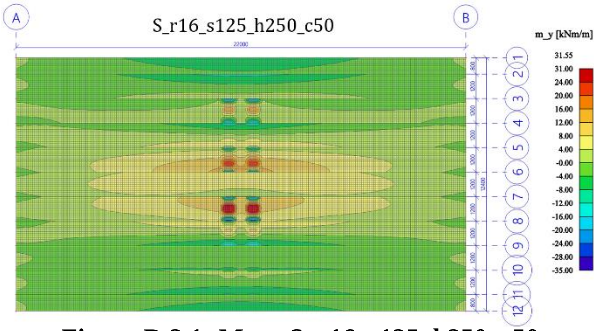

Figure D.2.1: M_{trans} S_r16_s125_h250_c50

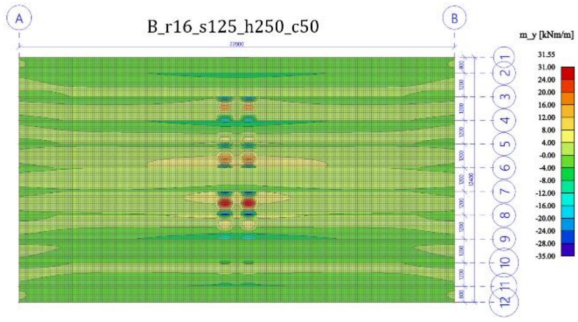

Figure D.2.2: M_{trans} B_r16_s125_h250_c50

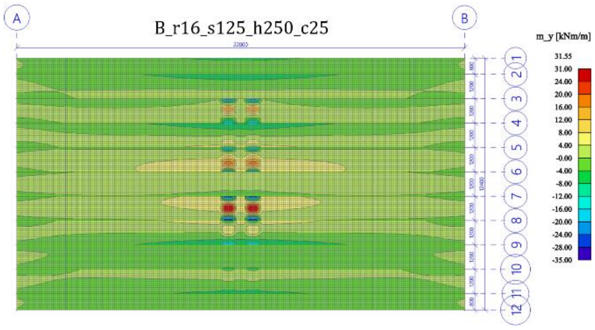

Figure D.2.3: M_{trans} B_r16_s125_h250_c25

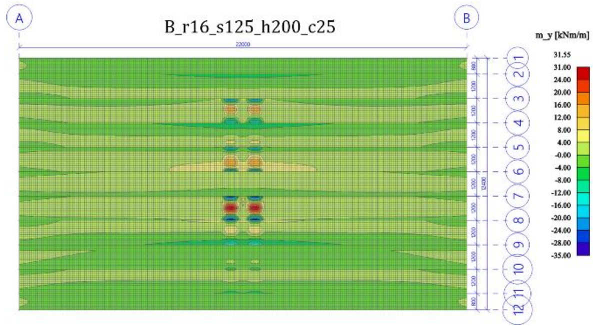

Figure D.2.4: M_{trans} B_r16_s125_h200_c25

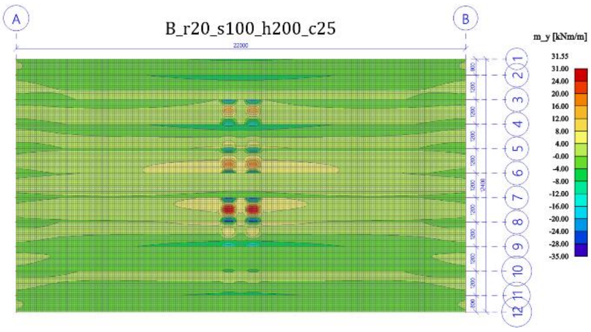

Figure D.2.5: M_{trans} B_r20_s100_h200_c25

Variant	$M_{Ek,trans}$ (hog – span)	$M_{Rd,trans}$
S-r16-s125-h250-c50	30,0 kNm/m – 31,6 kNm/m	120 kNm/m
B-r16-s125-h250-c50	34,1 kNm/m – 26,6 kNm/m	121 kNm/m
B-r16-s125-h250-c25	33,6 kNm/m – 27,3 kNm/m	138 kNm/m
B-r16-s125-h200-c25	34,6 kNm/m – 26,1 kNm/m	103 kNm/m
B-r20-s100-h200-c25	33,7 kNm/m – 27,1 kNm/m	107 kNm/m

D.3 Transverse shear forces – E_{fic} at $0{,}5M_{Rd}$

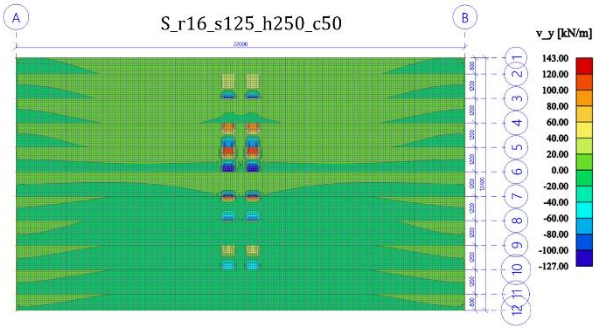

Figure D.3.1: V_{trans} S_r16_s125_h250_c50

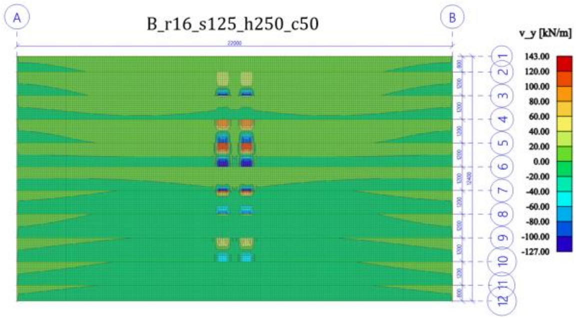

Figure D.3.2: V_{trans} B_r16_s125_h250_c50

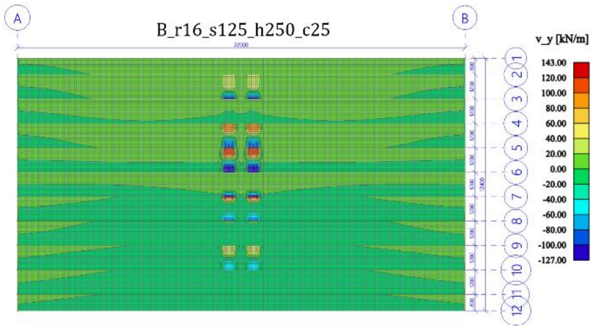

Figure D.3.3: V_{trans} B_r16_s125_h250_c25

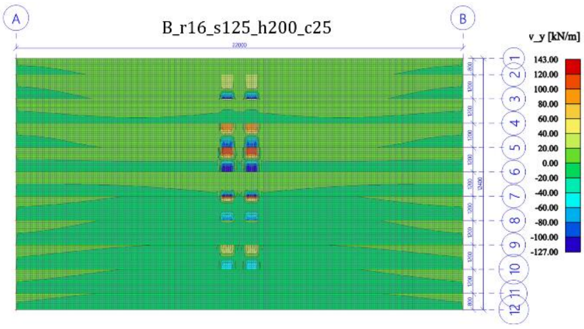

Figure D.3.4: V_{trans} B_r16_s125_h200_c25

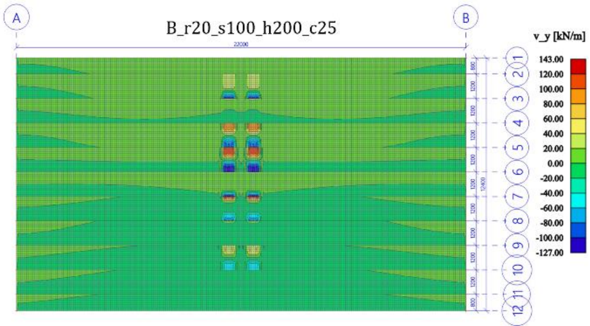

Figure D.3.5: V_{trans} B_r20_s100_h200_c25

APPENDIX E – Governing shear force configuration locally

This appendix provides a comprehensive study of the governing shear force configuration. Various configurations were examined, taking into account the reduction factor for loads near the support, as prescribed by Eurocode. The 0,5d variant was found to be the critical load configuration. See Section 4.4 for further background and the necessity of this study.

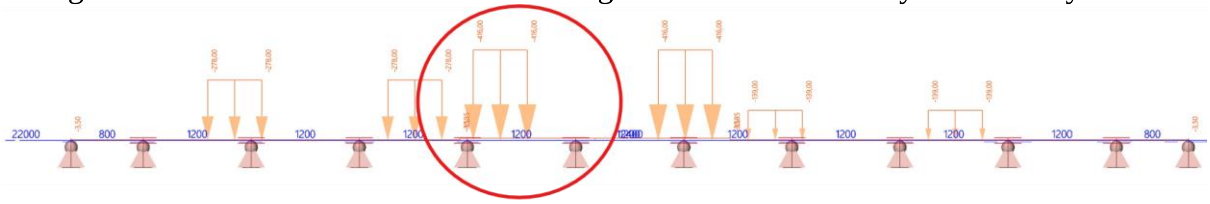

Figure E.1: Zoomed location in cross section of bridge deck

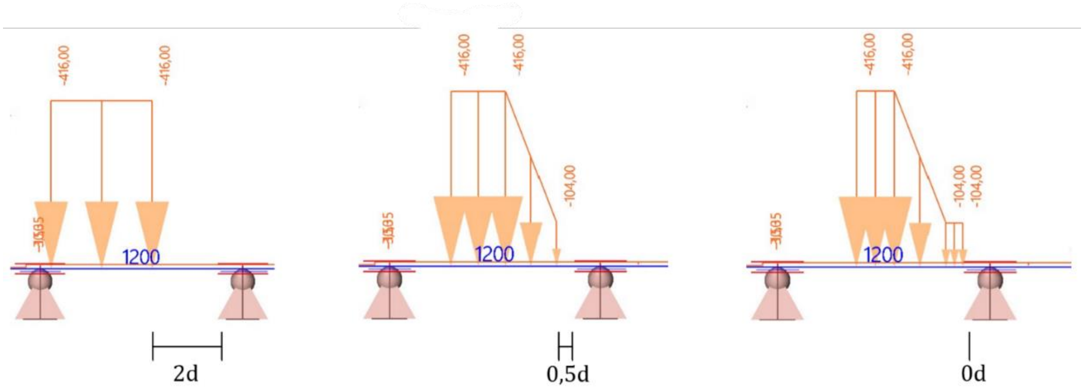

Figure E.2: Variants for maximum shear force study

Table E.1: Maximum transverse shear forces, 2d

Variant	2d	$V_{Ek,trans\ 2d}$	$V_{Rd,trans}$
S-r16-s125-h250-c50	384 mm	45 kN/m	135 kN/m
B-r16-s125-h250-c50	384 mm	42 kN/m	104 kN/m
B-r16-s125-h250-c25	434 mm	38 kN/m	114 kN/m
B-r16-s125-h200-c25	334 mm	48 kN/m	91 kN/m
B-r20-s100-h200-c25	330 mm	49 kN/m	97 kN/m

Table E.2: Maximum transverse shear forces, 0,5d

Variant	0,5d	$V_{Ek,trans\ 0,5d}$	$V_{Rd,trans}$
S-r16-s125-h250-c50	96 mm	56 kN/m	135 kN/m
B-r16-s125-h250-c50	96 mm	55 kN/m	104 kN/m
B-r16-s125-h250-c25	109 mm	53 kN/m	114 kN/m
B-r16-s125-h200-c25	84 mm	59 kN/m	91 kN/m
B-r20-s100-h200-c25	83 mm	59 kN/m	97 kN/m

Table E.3: Maximum transverse shear forces, 0d

Variant	0d	$V_{Ek,trans\ 0d}$	$V_{Rd,trans}$
S-r16-s125-h250-c50	0 mm	52 kN/m	135 kN/m
B-r16-s125-h250-c50	0 mm	52 kN/m	104 kN/m
B-r16-s125-h250-c25	0 mm	49 kN/m	114 kN/m
B-r16-s125-h200-c25	0 mm	55 kN/m	91 kN/m
B-r20-s100-h200-c25	0 mm	56 kN/m	97 kN/m

APPENDIX F – ECI calculations A1 & A2 comparison

This appendix provides the detailed calculation of the ECI for BFRP and steel rebar for the LCA stages A1 – A3. The ECI values are calculated by multiplying the shadow costs by the values of the environmental impact categories from the Environmental Product Declaration of both materials. The ECI has been calculated for both the current A1 standard and the future A2 standard. The ECI is determined for a quantity of 1 kilogram of product.
Notably, when comparing the A1 standard with the A2 standard, the ECI for steel increases by 85%, while the ECI for BFRP increases by only 39%. This indicates that once the new standard comes into effect, constructing with BFRP will become even more sustainable compared to steel. It is also noteworthy that for BFRP, the share of Global Warming Potential (GWP) in the new standard increases from 42% to 72%. For steel, such significant changes in the share of impact categories are less pronounced.

NEN-EN 15804+A1

	BFRP	Steel	Shadow costs (€/unit)	price BFRP	%	price Steel	%
ADPE	2,14E-05	9,66E-06	€ 0,16000	€ 0,00	0,00	€ 0,00	0,00
ADPF	2,18E-02	7,50E-03	€ 0,16000	€ 0,00	0,01	€ 0,00	0,01
GWP	2,69E+00	9,92E-01	€ 0,05000	€ 0,13	0,42	€ 0,05	0,35
ODP	2,85E-07	8,87E-08	€ 30,00000	€ 0,00	0,00	€ 0,00	0,00
POCP	1,40E-03	1,03E-03	€ 2,00000	€ 0,00	0,01	€ 0,00	0,01
AP	9,96E-03	4,62E-03	€ 4,00000	€ 0,04	0,13	€ 0,02	0,13
EP	1,45E-03	6,42E-04	€ 9,00000	€ 0,01	0,04	€ 0,01	0,04
HTP	1,23E+00	6,24E-01	€ 0,09000	€ 0,11	0,35	€ 0,06	0,40
FAETP	1,63E-01	2,19E-02	€ 0,03000	€ 0,00	0,02	€ 0,00	0,00
MAETP	8,13E+01	4,21E+01	€ 0,00010	€ 0,01	0,03	€ 0,00	0,03
TETP	6,28E-03	6,01E-02	€ 0,06000	€ 0,00	0,00	€ 0,00	0,03
total				€ 0,32	1,00	€ 0,14	1

NEN-EN 15804+A2

	BFRP	Steel	Shadow costs (€/unit)	price BFRP	%	price Steel	%
GWP-total	2,76E+00	1,02E+00		€ 0,00	0,00	€ 0,00	0,00
GWP-fossil	2,75E+00	1,02E+00	€ 0,11600	€ 0,32	0,72	€ 0,12	0,46
GWP-biogenic	6,20E-03	3,97E-03	€ 0,11600	€ 0,00	0,00	€ 0,00	0,00
GWP-luluc	4,43E-03	1,18E-03	€ 0,11600	€ 0,00	0,00	€ 0,00	0,00
ODP	3,15E-07	9,20E-08	€ 32,00000	€ 0,00	0,00	€ 0,00	0,00
AP	1,22E-02	5,70E-03	€ 0,39000	€ 0,00	0,01	€ 0,00	0,01
EP-freshwater	1,09E-04	5,32E-05	€ 1,96000	€ 0,00	0,00	€ 0,00	0,00
EP-marine	2,66E-03	1,23E-03	€ 3,28000	€ 0,01	0,02	€ 0,00	0,02
EP-terrestrial	2,85E-02	1,35E-02	€ 0,36000	€ 0,01	0,02	€ 0,00	0,02
POCP	9,38E-03	4,90E-03	€ 1,22000	€ 0,01	0,03	€ 0,01	0,02
ADP-minerals & metals	2,14E-05	9,66E-06	€ 0,30000	€ 0,00	0,00	€ 0,00	0,00
ADP-fossil	4,14E+01	1,45E-01	€ 0,00033	€ 0,01	0,03	€ 0,00	0,00
WDP	5,59E-01	5,38E-01	€ 0,00506	€ 0,00	0,01	€ 0,00	0,01
PM	9,55E-08	1,00E-07	€ 575.838,00000	€ 0,05	0,12	€ 0,06	0,22
IRP	1,00E-01	5,98E-02	€ 0,04900	€ 0,00	0,01	€ 0,00	0,01
ETP-fw	4,43E+01	2,24E+01	€ 0,00013	€ 0,01	0,01	€ 0,00	0,01
HTP-c	1,61E-09	1,05E-08	€ 1.096.368,00000	€ 0,00	0,00	€ 0,01	0,04
HTP-nc	2,20E-08	2,97E-07	€ 147.588,00000	€ 0,00	0,01	€ 0,04	0,17
SQP	9,94E+00	4,28E+00	€ 0,00018	€ 0,00	€ 0,00	€ 0,00	0,00
total				€ 0,445	1,00	€ 0,258	1,00

Figure F.1: Detailed ECI calculation for BFRP and steel

APPENDIX G – ECI calculation design variants

In addition to Section 7.6, this appendix presents the detailed calculations performed to obtain the ECI values for each design variant per square meter of bridge deck. Firstly, Table G.1 provides the values of the ECI per unit volume of material. Subsequently, the volume of each material per square meter of bridge deck is determined in Table G.2. Finally, in Tables G.3 and G.4, the ECI is calculated by multiplying the volumes of the construction materials by the ECI costs per unit volume, resulting in the total ECI value for each design variant.

Table G.1: ECI construction materials

Material	ECI	Source
C30/37 CEM I	€24,24 / m^3	Nationale Milieudatabase
C30/37 CEM III	€12,66 / m^3	Nationale Milieudatabase
BFRP rebar	€640,00 / m^3	See Chapter 7
Steel rebar	€1114,70 / m^3	See Chapter 7

Table G.2: Construction material quantities per m^2 bridge deck

Design variant	Height	Concrete volume	$\varphi_{longitudinal}$	$\varphi_{transverse}$	Rebar volume
S-r16-s125-h250-c50	250 mm	0,25 m^3	r12-s150	r16-s125	0,004724 m^3
B-r16-s125-h250-c50	250 mm	0,25 m^3	r12-s150	r16-s125	0,004724 m^3
B-r16-s125-h250-c25	250 mm	0,25 m^3	r12-s150	r16-s125	0,004724 m^3
B-r16-s125-h200-c25	200 mm	0,20 m^3	r12-s150	r16-s125	0,004724 m^3
B-r20-s100-h200-c25	200 mm	0,20 m^3	r16-s135	r20-s100	0,009262 m^3
B-r16-s125-h215-c25	215 mm	0,215 m^3	r12-s150	r16-s125	0,004724 m^3

Table G.3: ECI calculation per m² bridge deck C30/37 CEM I

Variant	C30/37 CEM I	BFRP	Steel	Total
S-r16-s125-h250-c50	0,25 * 24,24 = € 6,06	€ 0	0,004724 * 1114,7 = € 5,27	€ 11,33 (0%)
B-r16-s125-h250-c50	0,25 * 24,24 = € 6,06	0,004724 * 640 = € 3,02	€ 0	€ 9,08 (-20%)
B-r16-s125-h250-c25	0,25 * 24,24 = € 6,06	0,004724 * 640 = € 3,02	€ 0	€ 9,08 (-20%)
B-r16-s125-h200-c25	0,20 * 24,24 = € 4,85	0,004724 * 640 = € 3,02	€ 0	€ 7,87 (-30%)
B-r20-s100-h200-c25	0,20 * 24,24 = € 4,85	0,009262 * 640 = € 5,93	€ 0	€ 10,78 (-5%)
B-r16-s125-h215-c25	0,215 * 24,24 = € 5,21	0,004724 * 640 = € 3,02	€ 0	€ 8,23 (-27%)

Table G.4: ECI calculation per m² bridge deck C30/37 CEM III

Variant	C30/37 CEM III	BFRP	Steel	Total
S-r16-s125-h250-c50	0,25 * 12,66 = € 3,17	€ 0	0,004724 * 1114,7 = € 5,27	€ 8,44 (0%)
B-r16-s125-h250-c50	0,25 * 12,66 = € 3,17	0,004724 * 640 = € 3,02	€ 0	€ 6,19 (-26%)
B-r16-s125-h250-c25	0,25 * 12,66 = € 3,17	0,004724 * 640 = € 3,02	€ 0	€ 6,19 (-26%)
B-r16-s125-h200-c25	0,20 * 12,66 = € 2,53	0,004724 * 640 = € 3,02	€ 0	€ 5,55 (-34%)
B-r20-s100-h200-c25	0,20 * 12,66 = € 2,53	0,009262 * 640 = € 5,93	€ 0	€ 8,59 (+2%)
B-r16-s125-h215-c25	0,215 * 12,66 = € 2,72	0,004724 * 640 = € 3,02	€ 0	€ 5,74 (-32%)